

1
2

CONNECTING OBSERVED MICROBURST PRECIPITATION WITH ITS
SCATTERING MECHANISM

3

by

Mykhaylo Sergeevich Shumko

4

A dissertation submitted in partial fulfillment
of the requirements for the degree

of

Doctor of Philosophy

in

Physics

5

MONTANA STATE UNIVERSITY
Bozeman, Montana

October 2019

6

7

©COPYRIGHT

8

by

Mykhaylo Sergeevich Shumko

2019

All Rights Reserved

DEDICATION

⁹ I dedicate this to all MSU students who use L^AT_EX. Dedication is optional
¹⁰ and may be no longer than one page, single spaced, and should precede the
¹¹ acknowledgments page.

ACKNOWLEDGEMENTS

¹² I would like acknowledge the countless engineers, technicians, and scientists who
¹³ made the FIREBIRD, AC-6, and RBSP missions a success. This work was supported
¹⁴ by Montana State University and by NASA Headquarters under the NASA Earth and
¹⁵ Space Science Fellowship Program - Grant 80NSSC18K1204. **Add co-author support.**

TABLE OF CONTENTS

16	1. INTRODUCTION	1
17	Charged Particle Motion in Electric and Magnetic Fields	2
18	Particle Populations and Their Interractions in the Magnetosphere	8
19	Inner Magnetosphere Populations.....	11
20	Plasmasphere.....	13
21	Ring Current	15
22	Radiation Belts.....	16
23	Radiation Belt Particle Sources and Sinks	20
24	Adiabatic Heating	20
25	Wave Resonance Heating	21
26	Particle Losses	25
27	Microbursts	26
28	Scope of Reserach	29
29	2. CHAPTER TWO	
30	EVIDENCE OF MICROBURSTS OBSERVED NEAR THE EQUA-	
31	TORIAL PLANE IN THE OUTER VAN ALLEN RADIATION	
32	BELT	31
33	Contribution of Authors and Co-Authors	31
34	Manuscript Information	32
35	Key Points	33
36	Abstract	33
37	Introduction	33
38	Spacecraft Instrumentation	36
39	Observations	37
40	Analysis.....	40
41	Microburst and Source PSD	40
42	Motion of resonant electrons in phase space	43
43	Comparing the microburst PSD to diffusion theory	46
44	Discussion and Conclusions	48
45	Acknowledgments	49
46	3. CHAPTER THREE	
47	MICROBURST SCALE SIZE DERIVED FROM MULTIPLE BOUNCES	
48	OF A MICROBURST SIMULTANEOUSLY OBSERVED WITH	
49	THE FIREBIRD-II CUBESATS	51
50	Contribution of Authors and Co-Authors	51

TABLE OF CONTENTS – CONTINUED

51	Manuscript Information	52
52	Key Points	53
53	Abstract	53
54	Introduction	54
55	Spacecraft and Observation	56
56	Analysis.....	59
57	Electron Bounce Period	60
58	Microburst Energy Spectra	62
59	Microburst Scale Sizes	62
60	Discussion and Conclusions	65
61	Acknowledgments	67
62	4. CHAPTER FOUR	
63	MICROBURST SIZE DISTRIBUTION DERIVED WITH AEROCUBE-	
64	6	68
65	Contribution of Authors and Co-Authors	68
66	Manuscript Information	69
67	5. CONCLUSIONS AND FUTURE WORK	70
68	Future Work.....	71
69	REFERENCES CITED.....	72
70	APPENDIX: Appendix A.....	81
71	APPENDIX: Appendix B	84

LIST OF FIGURES

Figure	Page
72 1.1 The three periodic motions of charged particles 73 in Earth's dipole magnetic field. These motions 74 are: gyration about the magnetic field line, bounce 75 motion between the magnetic poles, and azimuthal 76 drift around the Earth. Figure from (Baumjohann 77 and Treumann, 1997).	2
78 1.2 Charged particle motion in a uniform magnetic field 79 \vec{B} . Panel (A) shows the geometry defining the 80 pitch angle, α . Panel (B) and (C) show two helical 81 electron trajectories with dashed lines assuming a 82 large and small α (corresponding to a small and large 83 parallel velocity $v_{ }$), respectively.	6
84 1.3 Contours of constant gyration, bounce, and drift 85 frequencies for electrons and protons in a dipole field. 86 Figure from Schulz and Lanzerotti (1974).	7
87 1.4 Macroscopic structures in the outer magnetosphere. 88 The solar wind with its frozen-in interplanetary 89 magnetic field is shown on the left and is traveling 90 supersonically towards the right. The solar wind 91 envelops Earth's magnetic field to create the mag- 92 netosphere cavity. Since the solar wind is traveling 93 supersonically, it creates a bow shock up stream. 94 Downstream of the bow shock the shocked solar wind 95 plasma inside the magnetosheath flows around the 96 magnetopause, a boundary between the solar wind 97 and magnetosphere. Figure from Baumjohann and 98 Treumann (1997).	9
99 1.5 Macroscopic structures in the inner magnetosphere 100 most relevant to this dissertation. The plasmas- 101 phere, and the radiation belts are shown and ring 102 current is co-located there as well. Sun is to the left. 103 Figure from Baumjohann and Treumann (1997).	10
104 1.6 The series of steps involved in magnetic reconnection 105 with a southward IMF. Figure from Baumjohann 106 and Treumann (1997).	12

LIST OF FIGURES – CONTINUED

Figure	Page
107 108 109 110 111 112 113 1.7 Equipotential lines and electric field arrows due to the superposition of the co-rotation and convection electric fields. Electrons in the shaded region execute closed orbits. Outside of the shaded regions the electrons are not trapped and will escape. The region separating the two regimes is called the Alfvén layer. Figure from Baumjohann and Treumann (1997).....	14
114 115 116 117 118 119 120 121 122 123 124 125 126 127 128 129 130 1.8 The DST index during the St. Patrick's Day 2015 storm. This storm was caused by a coronal mass ejection on March 15th, 2015. The storm phases are: initial phase, main phase, and recovery phase. The initial phase occurred when the Dst peaked at +50 nT on March 17th during which the ring current was eroded by the coronal mass ejection during the interval shown by the red bar. Then the rapid decrease to ≈ -200 nT was during the main phase where many injections from the magnetotail pumped up the ring current which reduced Earth's magnetic field strength at the ground and is shown with the green bar. Lastly, the recovery phase lasted from March 18th to approximately March 29th during which the ring current particles were lost and the ring current returned to its equilibrium state. The recovery phase is shown with the blue bar.....	17
131 132 133 1.9 The two radiation belts with a the locations of various satelites and orbits. Figure from (Horne et al., 2013).	18
134 135 136 137 138 139 1.10 The dynamics of the outer radiation belt in 1997 from the POLAR satellite. Top panel shows the 1.2-2.4 MeV electron flux as a function of L and 1997 day of year. The middle panel shows the DST index, and bottom panel shows the solar wind velocity. Figure from (Reeves et al., 2003).	19

LIST OF FIGURES – CONTINUED

Figure	Page
140 1.11 The trajectories of an electron and a right-hand cir- 141 cularly polarized wave during a cyclotron resonance. 142 The electron's v_{\parallel} and the wave's k_{\parallel} are in opposite 143 directions such that the wave's frequency is Doppler 144 shifted to a integer multiple of the electron cyclotron 145 frequency. Figure from (Tsurutani and Lakhina, 1997).	22
146 1.12 Various wave modes in the magnetosphere. Ultra 147 low frequency waves occur throught the magneto- 148 sphere. Chorus waves are typically observed in 149 the 0-12 midnight-dawn region. EMIC waves are 150 typically observed in the dusk MLT sector. Hiss 151 waves are observed inside the plasmasphere. Figure 152 from Millan and Thorne (2007).....	24
153 1.13 An example train of microbursts observed by FIREBIRD- 154 II unit 4 on February 2nd, 2015. The colored curves 155 show the differential energy channel count rates in 156 six channels from ≈ 200 keV to greater than 1 MeV. 157 The x-axis labels show auxiliary information such as 158 time of observation and the spacecraft position in L, 159 MLT, latitude and longitude coordinates.	27
160 1.14 Relativistic ($> 1\text{MeV}$) distribution of microburst 161 occurrence rates as a function of L and MLT. The 162 three panels show the microburst occurrence rate 163 dependence on geomagnetic activity, parameterized 164 by the auroral electrojet (AE) index for (a) $\text{AE} <$ 165 100 nT, (b) $100 < \text{AE} < 300$ nT and (c) $\text{AE} > 300$ 166 nT. Figure from Douma et al. (2017).....	28

LIST OF FIGURES – CONTINUED

Figure	Page
167 2.1 Electron and wave conditions from the MagEIS-A 168 and EMFISIS WFR sensors for the microburst time 169 interval. Panels (a), (b), and (c) are from RBSP-A 170 with its position information annotated in panel (a). 171 Panels (d), (e), and (f) are from RBSP-B with its 172 position information annotated in panel (d). Panel 173 (a) is the MagEIS-A high rate timeseries. Panels (b) 174 and (e) show the evolution of the MagEIS-A J as a 175 function of α_L from the ~ 40 to ~ 60 keV channel. 176 Every 10th point is shown in panel (b). The solid 177 black line in panels (a) and (b) mark the end of 178 the time period used for the PSD fit extrapolation 179 analysis explained in section 3. The dashed black 180 lines in panels (a) and (b) show the time interval 181 used for the observed microburst PSD. Panels (c) 182 and (f) show the EMFISIS WFR spectra, with the 183 available burst data superposed. The red, green, and 184 cyan traces are equatorial f_{ce0} , $f_{ce0}/2$, and $f_{ce0}/10$, 185 respectively.	39
186 2.2 Panel (a) shows the MagEIS-A high rate timeseries. 187 Panel (b) shows the RBSPICE EBR count rate 188 timeseries for $\gtrsim 19$ keV electrons. The microbursts 189 were observed between 11:17:10 - 11:17:12 UT and 190 are indicated with the vertical black arrows in panels 191 (a) and (b) for MagEIS-A times. Panel (c) shows the 192 RBSPICE EBR (family of relatively sparse sampled 193 curves) and MagEIS-A J from the 29-41 keV energy 194 channel (single curve) as a function of α_L . The 195 vertical dashed lines show the time interval for the 196 PSD analysis.....	41

LIST OF FIGURES – CONTINUED

Figure	Page
197 2.3 The colored annulus represents $f(p_\perp, p_{\parallel})$ in normalized momentum space, parallel and perpendicular to the background magnetic field. The microburst $f(p_\perp, p_{\parallel})$ is highlighted with the white circle. The columns show different powers of the sine extrapolation, and rows show the different magnetic latitudes of the scattering. The white dotted traces represent the boundary between the data and extrapolation. The green, red, and white solid traces are the resonance curves for $\omega = 0.2\Omega_{ce}$, $0.4\Omega_{ce}$, $0.6\Omega_{ce}$, respectively. The cyan dashed traces are the diffusion curves for a $\omega = 0.4\Omega_{ce}$ wave (waves of other frequency have similar diffusion curves). The magnetic latitude of the scattering, the ratio of the plasma to the cyclotron frequency, and the power of the sine extrapolation is annotated in each panel. For the resonance and diffusion curves, the density model assumed a $n_L = 1 e^-/cm^3$ and $\psi = -1$	44
215 3.1 HiRes data of the microburst observed at February 2nd, 2015 at 06:12:53 UT, smoothed with a 150 ms rolling average. The subsequent bounces showed some energy dispersion. As discussed in Appendix B, a time correction of -2.28 s was applied to FU3. While the flux from five energy channels is shown, only channels with reasonable counting statistics were used for the spatial scale analysis. Vertical colored bars show the \sqrt{N} error every 10th data point and vertical black bars are lined up with the peaks in the 220-283 keV energy channel to help identify dispersion.	58

LIST OF FIGURES – CONTINUED

Figure	Page
227 3.2 Observed and theoretical t_b for electrons of energies 228 from 200 to 770 keV. The solid black line is t_b 229 in a dipole magnetic field, derived in Schulz and 230 Lanzerotti (1974). The red dotted and cyan dashed 231 lines are the t_b derived using the T89, and T04 232 magnetic field models with IRBEM-Lib. Lastly, 233 the blue dot-dash curve is the t_b derived using the 234 Olson & Pfitzer Quiet model. The green and purple 235 rectangles represent the observed t_b for FU3 and 236 FU4 using a Gaussian fit, respectively. The blue 237 rectangles represent the observed t_b calculated with 238 the minima between the bounces. The width of the 239 boxes represent the width of those energy channels, 240 and the height represents the uncertainty from the fit.....	61
241 3.3 The topology of the FIREBIRD-II orbit and the 242 multiple bounces of the microburst projected onto 243 latitude and longitude with axis scaled to equal 244 distance. Attributes relating to FU3 shown in red 245 dashed lines, and FU4 with blue solid lines. The 246 spacecraft path is shown with the diagonal lines, 247 starting at the upper right corner. The labels P1- 248 4 for FU4 and P1-5 for FU3 indicate where the 249 spacecraft were when the N^{th} peak was seen in 250 the lowest energy channel in the HiRes data. The 251 stars with the accompanying energy labels represent 252 the locations of the electrons with that energy that 253 started at time of P1, and were seen at the last peak 254 on each spacecraft. The rectangles represent the 255 lower bound of the microburst scale size, assuming 256 that the majority of the electrons were in the upper 257 boundary of energy channel 4.....	64

LIST OF FIGURES – CONTINUED

Figure	Page
258 A.1 Panel (A) shows the magnetic power spectral density 259 as a function of frequency and time from the EMFI- 260 SIS WFR instrument on board RBSP-A. The “hiss- 261 like” wave used for the resonant diffusion analysis 262 was observed starting at 11:17:03 UT. In the same 263 format as panel (A), panel (B) shows the polar angle 264 of the wave vector for this time period. The wave 265 of interest had a normal wave vector, $\theta_k < 30^\circ$. 266 Since the results in panel (B) are valid only for high 267 planarity, panel (C) shows planarity in the same 268 format as panels (A) and (B). The wave of interest 269 was found to have a planarity of > 0.8 . Lastly, panel 270 (D) shows the available burst mode data.	82
271 A.2 Ratio of the RBSPICE EBR at microburst times 272 indicated with the black vertical arrows in Fig. 2, 273 to the EBR at the same pitch angles one spin prior 274 (quiet time). The microburst flux was enhanced by 275 10-80% across $100^\circ < \alpha_L < 160^\circ$ PA, and appear to 276 be peaked closer to $\alpha_L = 90^\circ$	83
277 B.1 Cross-correlation time lag analysis applied to a train 278 of microbursts. Panel (a) and (b) show the count 279 rate from the lowest energy channel. Panel (c) shows 280 the cross-correlation coefficient as a function of time 281 lag. Panel (d) shows the shifted timeseries. Clock 282 difference was 2.23 s.	86
283 B.2 Same analysis as Fig. B.1 on a different time period. 284 Clock difference was 2.21 s.	87
285 B.3 Same analysis as Fig. B.1 on a different time period. 286 Clock difference was 2.25 s.	88
287 B.4 Same analysis as Fig. B.1 on a different time period. 288 Clock difference was 2.27 s.	89

LIST OF FIGURES – CONTINUED

Figure		Page
289	B.5 Same cross-correlation time lag analysis applied to	
290	stationary spatial structures. The cross-correlation	
291	lag between these events is a sum of the clock differ-	
292	ence and time lag due to the spacecraft separation.	
293	The lag derived at this time was 4.95 s.....	90
294	B.6 Same analysis as Fig. B.5 applied to a different	
295	stationary spatial feature. The lag derived at this	
296	time was 5.01 s.	91

NOMENCLATURE

L	L-Shell
MLT	magnetic local time
λ	magnetic latitude
α	pitch angle
α_L	local pitch angle at the spacecraft
α_{eq}	pitch angle maped to the magnetic equator
c	speed of light
R_E	Earth's radius
J	flux
f	phase space density
E	energy
E_0	exponential e-folding energy
p	momentum
\vec{E}	electric field
\vec{B}	magnetic field
B_w	wave amplitude
v	velocity
Ω_e	electron gyrofrequency
ω_{pe}	plasma frequency
k	wave vector
D_{xx}	diffusion coefficient
s	spacecraft separation
t_b	electron bounce period

297

INTRODUCTION

299 Above Earth's atmosphere are the a pair of Van Allen radiation belts, a complex
300 and dynamic plasma environment that effects our technology-driven society. These
301 effects include: a higher radiation dose for astronauts and cosmonauts, higher chance
302 of spacecraft failure due to single event upsets that can lead to catastrophic latchups,
303 degradation of silicon (changing the silicon doping) from an extended radiation dose
304 that can degrade a transistor to the point where it no longer function as a switch,
305 and the degradation of the ozone layer due to the chemical production of NO_X and
306 HO_X molecules. With these effects in mind, it is no surprise that the radiation belts
307 have been extensively studied since their discovery in the 1960s.

308 One natural phenomenon in the radiation belts that has been a topic of interest
309 in the space physics community is wave-particle intersections that, as we will explore
310 throughout this dissertation, can accelerate particles to very high energies (e.g. \approx
311 MeV for electrons) and scatter them into the atmosphere.

312 The goal of this dissertation is to study the wave-particle mechanism that
313 scatters microbursts, a sub-second impulse of electrons into Earth's atmosphere.
314 Before we dive deep into the physics of wave-particle interactions, an introduction to
315 Earth's magnetosphere is warranted. Single charged particle motion in Earth's electric
316 and magnetic fields will be described first. Then the major particle populations in
317 the magnetosphere and the coupling between them will be described. Lastly, a brief
318 overview of wave-particle interactions and their effects will be presented.

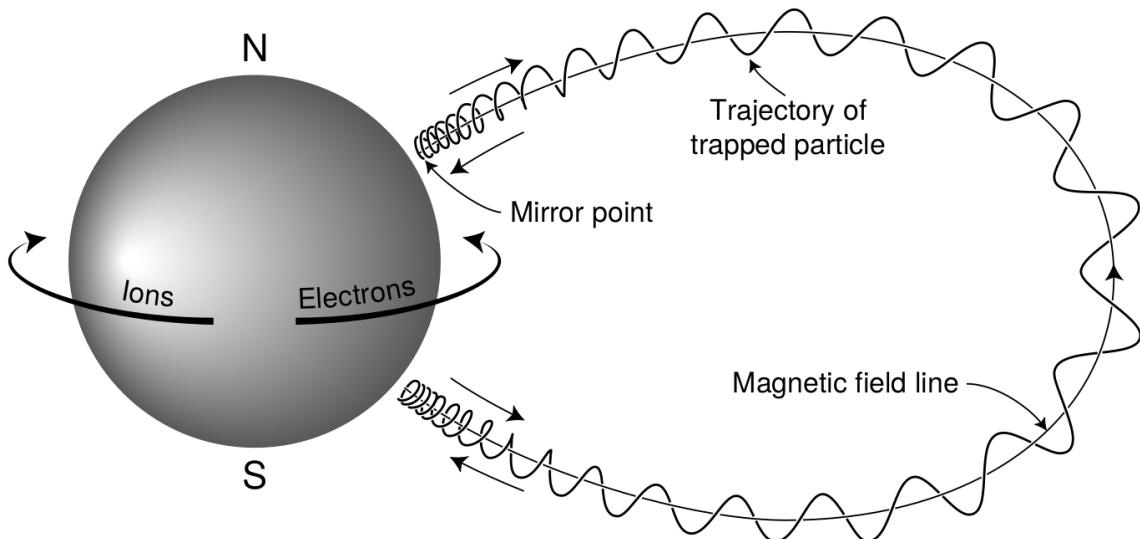


Figure 1.1: The three periodic motions of charged particles in Earth's dipole magnetic field. These motions are: gyration about the magnetic field line, bounce motion between the magnetic poles, and azimuthal drift around the Earth. Figure from (Baumjohann and Treumann, 1997).

319

Charged Particle Motion in Electric and Magnetic Fields

A charged particle trapped in the magnetosphere will experience three types of periodic motion in Earth's nearly dipolar magnetic field. The three motions are ultimately due to the Lorentz force that a particle of momentum \vec{p} , charge q , and velocity \vec{v} experiences in an electric field \vec{E} and magnetic field \vec{B} and is given by

$$\frac{d\vec{p}}{dt} = q(\vec{E} + \vec{v} \times \vec{B}). \quad (1.1)$$

- 320 In the magnetosphere, the three periodic motions in decreasing frequency are gyration,
 321 bounce, and drift and are schematically shown in Fig. 1.1. Each of these
 322 motions have a corresponding conserved quantity i.e. an adiabatic invariant.

The highest frequency periodic motion is gyration about a magnetic field of

magnitude B . This motion is circular with a Larmor radius of

$$r = \frac{mv_{\perp}}{|q|B} \quad (1.2)$$

where m is the mass and v_{\perp} the particle's velocity perpendicular to \vec{B} . This motion has a corresponding gyrofrequency

$$\Omega = \frac{|q|B}{m} \quad (1.3)$$

in units of radians/second. Inside the radiation belts the electron gyrofrequency, Ω_e is on the order of a kHz. The corresponding adiabatic invariant is found by integrating the particle's canonical momentum around the particle's path of gyration

$$J_i = \oint (\vec{p} + q\vec{A}) \cdot d\vec{l} \quad (1.4)$$

where J_i is the i^{th} adiabatic invariant and \vec{A} is the magnetic vector potential. This integral is carried out by integrating the first term over the circumference of the gyro orbit and integrating the second term using Stokes theorem to calculate the magnetic flux enclosed by the gyro orbit. With suitable integration, $J_1 \sim v_{\perp}^2/B$ and is conserved as the frequency of the driving force, ω satisfies $\omega \ll \Omega_e$.

The second highest frequency periodic motion is bouncing due to a parallel gradient in \vec{B} . This periodic motion naturally arises in the magnetosphere because Earth's magnetic field is stronger near the poles, and artificially in the laboratory in magnetic bottle machines. To understand this motion we first we need to define the concept of pitch angle α as the angle between \vec{B} and \vec{v} which is schematically shown in Fig. 1.2a. The pitch angle relates v with v_{\perp} , and $v_{||}$ (the component of the particles velocity parallel to \vec{B}). As shown in 1.2b and c, a larger α will tighten the

³³⁵ particle's helical trajectory and vice versa.

Assuming the particle's kinetic energy is concerned, the conservation of J_1 implies that given a particle's $v_{\perp}(0)$ and $B(0)$ at the magnetic equator (where Earth's magnetic field is usually at a minimum), we can calculate its $v_{\perp}(s)$ along the particle's path s by calculating $B(s)$ from magnetic field models. The particle's perpendicular velocity is then related via

$$\frac{v_{\perp}^2(0)}{B(0)} = \frac{v_{\perp}^2(s)}{B(s)} \quad (1.5)$$

³³⁶ which can be rewritten as

$$\frac{v^2 \sin^2 \alpha(0)}{B(0)} = \frac{v^2 - v_{\parallel}^2(s)}{B(s)} \quad (1.6)$$

³³⁷ and re-arranged to solve for $v_{\parallel}(s)$

$$v_{\parallel}(s) = v \sqrt{1 - \frac{B(s)}{B(0)} \sin^2 \alpha(0)} \quad (1.7)$$

³³⁸ which will tend towards 0 when the second term in the radical approaches 1.

³³⁹ The location where $v_{\parallel}(s) = 0$ is called the mirror point and is where a particle
³⁴⁰ stops and reverses direction. Since Earth's magnetic field is stronger towards the
³⁴¹ poles, the mirroring particle will execute periodic bounce motion between its two
³⁴² mirror points in the northern and southern hemispheres. The corresponding adiabatic
³⁴³ invariant, J_2 is

$$J_2 = \oint p_{\parallel} ds \quad (1.8)$$

where ds describes the particle path between the mirror points in the northern and southern hemispheres (see Fig. 1.1). J_2 is found by substituting Eq. 1.7 into Eq. 1.8 and defining the magnetic field strength at the mirror points as B_m where $\alpha(m) = 90^\circ$.

The J_2 integral can be written as

$$J_2 = 2p \int_{m_n}^{m_s} \sqrt{1 - \frac{B(s)}{B(m)}} ds \quad (1.9)$$

where m_n and m_s are the northern and southern mirror points, respectively. The bounce period can be estimated (e.g. Baumjohann and Treumann, 1997) to be

$$t_b \approx \frac{LR_e}{\sqrt{W/m}} (3.7 - 1.6 \sin \alpha(0)) \quad (1.10)$$

where L is the L -shell which describes the distance from the Earth's center to the location where a particular magnetic field line crosses the magnetic equator, in units of Earth radii, R_e . W is the particle's kinetic energy. As with gyration, a particle bounces as long as $\omega \ll \Omega_b$, where Ω_b is the bounce frequency.

At this stage it is instructional to introduce the notion of the loss cone pitch angle, α_L . A particle with $\alpha \leq \alpha_L$ will mirror at or below ≈ 100 km altitude in the atmosphere. A particle at those altitudes will encounter Earth's atmosphere and has a significant probability of Coulomb scattering with atmospheric particles and be lost to the atmosphere.

The slowest periodic motion experienced by charged particles in Earth's magnetic field is azimuthal drift around the Earth. This drift results from a combination of a radial gradient in \vec{B} and the curvature of the magnetic field. The radial gradient drift arises because Earth's magnetic field is stronger near the Earth where the particle's gyroradius radius of curvature is smaller as it gyrates towards stronger magnetic field, and larger when it gyrates outward. The overall effect is the particle gyro orbit does not close on itself and negatively charged particles drift East and positively charged particles drift West. The radial gradient drift is enhanced by the centrifugal force that a particle experiences as it bounces along the curved field lines. The drift adiabatic

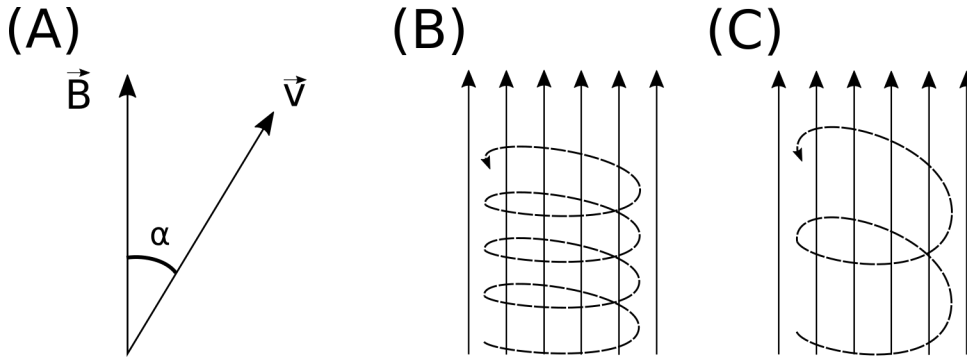


Figure 1.2: Charged particle motion in a uniform magnetic field \vec{B} . Panel (A) shows the geometry defining the pitch angle, α . Panel (B) and (C) show two helical electron trajectories with dashed lines assuming a large and small α (corresponding to a small and large parallel velocity $v_{||}$), respectively.

³⁶⁴ invariant, J_3 is found by integrating Eq. 1.4 over the complete particle orbit around
³⁶⁵ the Earth. The shape of this drift orbit is otherwise known as a drift shell. For J_3 ,
³⁶⁶ the first term is negligible and the second term is the magnetic flux enclosed by the
³⁶⁷ drift shell, Φ_m i.e. $J_3 \sim \Phi_m$.

³⁶⁸ Figure 1.3 from Schulz and Lanzerotti (1974) shows contours of the gyration,
³⁶⁹ bounce, and drift frequencies for electrons and protons in Earth's dipole magnetic
³⁷⁰ field.

Up until now we have considered the three periodic motions due Earth's magnetic field and the absence of electric fields. If \vec{E} is present, a particle's center of gyration i.e., averaged position of the particle over a gyration, will drift with a velocity perpendicular to both \vec{E} and \vec{B} . The drift velocity can be solved directly from Eq. 1.1 and is

$$\vec{v}_E = \frac{\vec{E} \times \vec{B}}{B^2}. \quad (1.11)$$

³⁷¹ Lastly, for more detailed derivations of these motions, see the following texts:
³⁷² Baumjohann and Treumann (1997); Schulz and Lanzerotti (1974); Tsurutani and
³⁷³ Lakhina (1997).

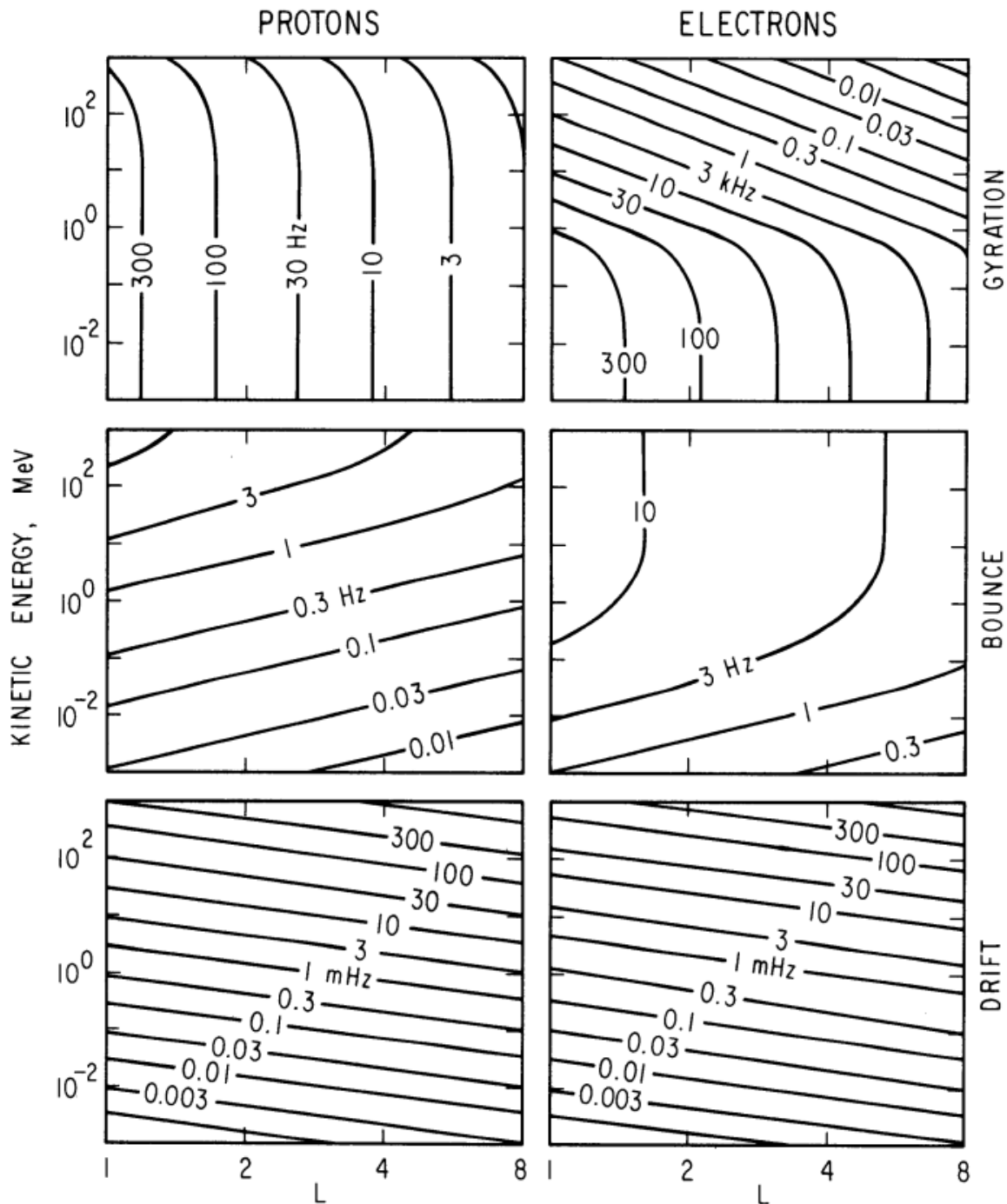


Figure 1.3: Contours of constant gyration, bounce, and drift frequencies for electrons and protons in a dipole field. Figure from Schulz and Lanzerotti (1974).

374

Particle Populations and Their Interractions in the Magnetosphere

375 The single-particle motion in Earth's magnetic field described in the previous
376 section is a prerequisite to understanding how magnetospheric particles organize into
377 macroscopic populations. The structure of the outer magnetosphere is shown in Fig.
378 1.4 and inner magnetosphere in Fig. 1.5. In this section we will introduce the various
379 particle populations in the magnetosphere and how they couple.

380 The sun and its solar wind are ultimately the source of energy input into the
381 magnetosphere. The solar wind at Earth's orbit is a plasma traveling at supersonic
382 speeds with an embedded interplanetary magnetic field (IMF). When the solar wind
383 encounters Earth's magnetic field the plasma can not easily penetrate into the
384 magnetosphere, rather it drapes around the magnetosphere forming a cavity in the
385 solar wind that is roughly shaped as shown in Fig. 1.4. Because the solar wind is
386 supersonic at 1 AU, a bow shock exists upstream of the magnetosphere. The solar
387 wind plasma, after it is shocked by the bow shock, flows around the magnetosphere
388 inside the magnetosheath. The surface where the solar wind ram pressure and Earth's
389 magnetic pressure balance is termed the magnetopause, which can be thought of as
390 a boundary between the solar wind's and Earth's plasma environments. This is
391 a slightly naive description of the magnetopause, but is nonetheless an instructive
392 conceptual picture. The shocked plasma then flows past the Earth where it shapes
393 the magnetotail. In the magnetotail the solar wind magnetic pressure balances Earth's
394 magnetic field pressure in the lobes. The magnetotail extends on the order of 100
395 R_E downstream of Earth [Add citation](#), and the tailward stretching of magnetic field
396 lines creates the plasma sheet which exists in the region of low magnetic field strength
397 near the magnetic equator [Add citation](#). The plasma sheet flows from dusk to dawn
398 (out of the page in Figs. 1.4 and 1.5) and this current is connected to a zoo of other

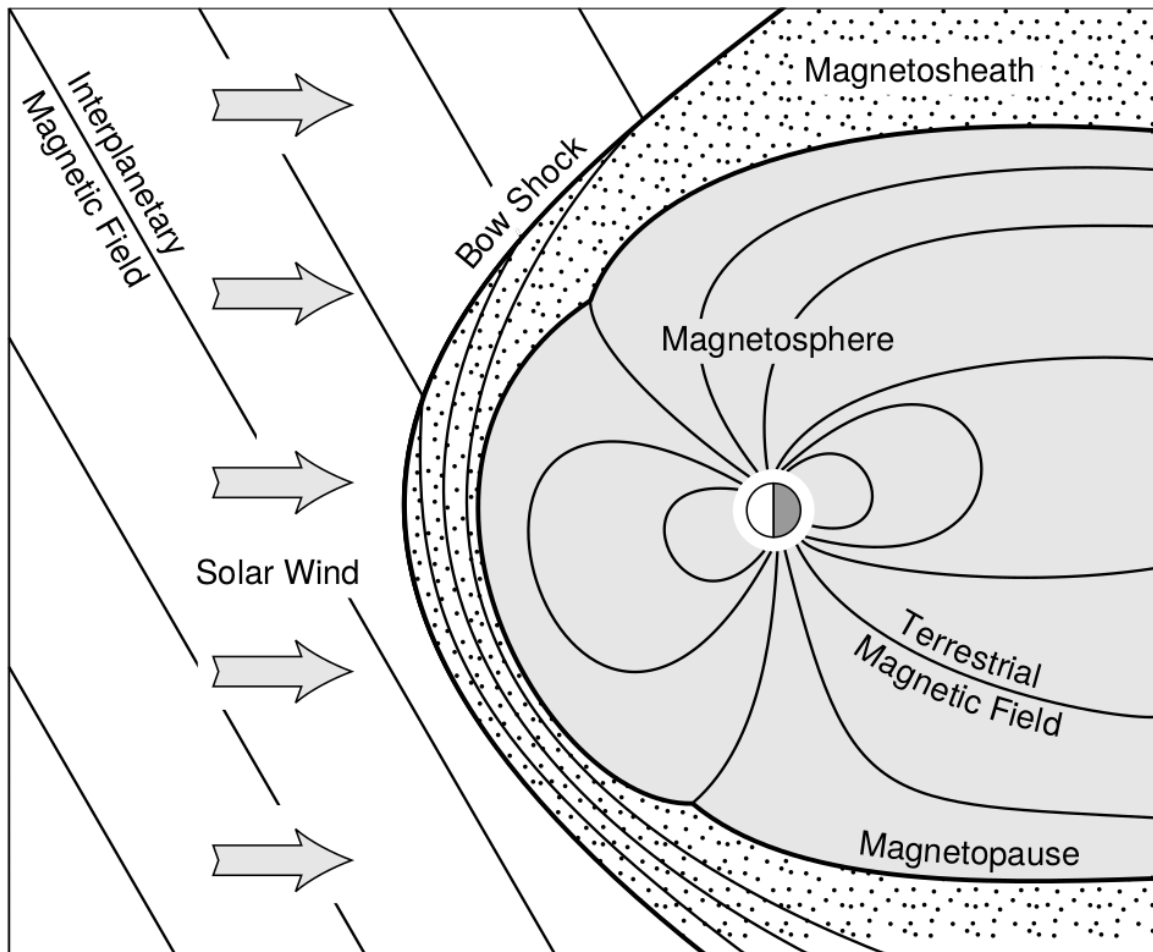


Figure 1.4: Macroscopic structures in the outer magnetosphere. The solar wind with its frozen-in interplanetary magnetic field is shown on the left and is traveling supersonically towards the right. The solar wind envelops Earth's magnetic field to create the magnetosphere cavity. Since the solar wind is traveling supersonically, it creates a bow shock up stream. Downstream of the bow shock the shocked solar wind plasma inside the magnetosheath flows around the magnetopause, a boundary between the solar wind and magnetosphere. Figure from Baumjohann and Treumann (1997).

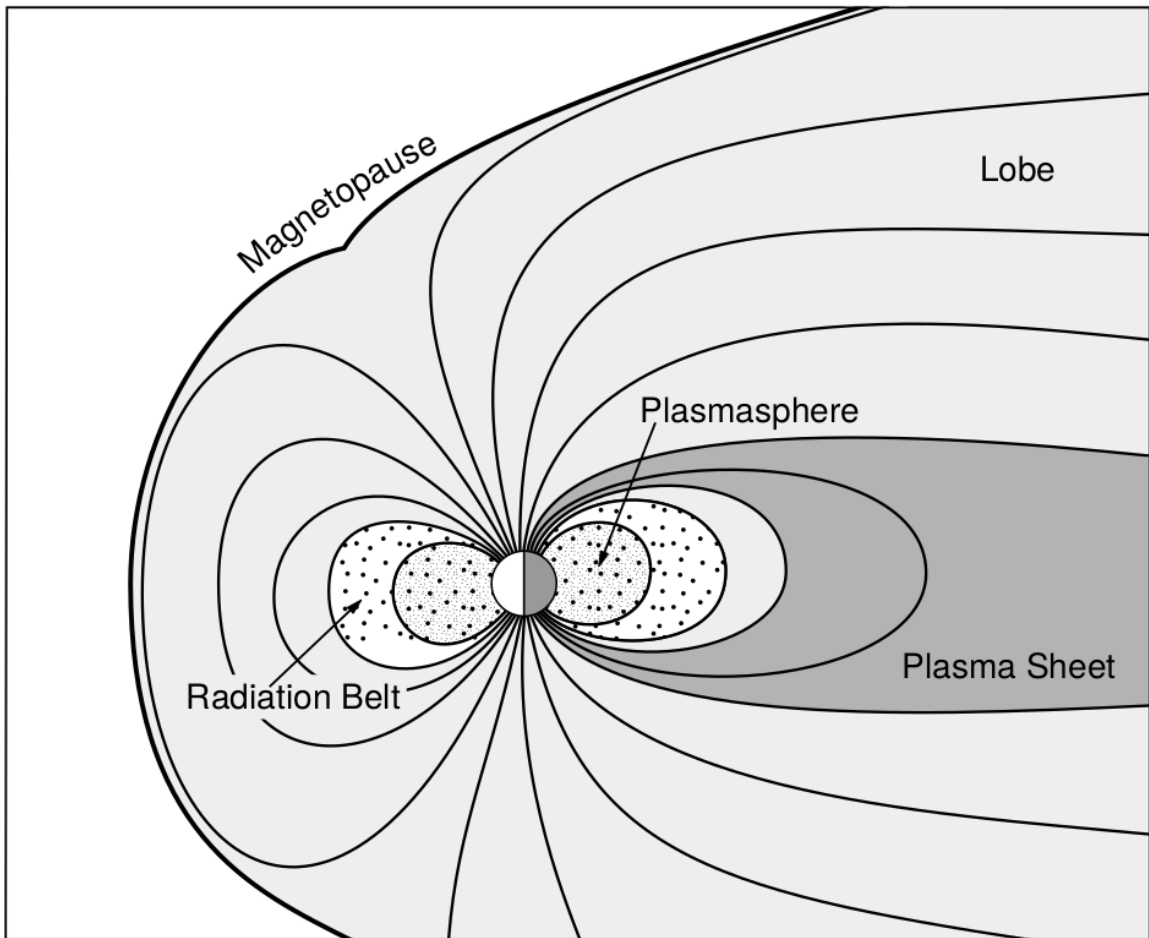


Figure 1.5: Macroscopic structures in the inner magnetosphere most relevant to this dissertation. The plasmasphere, and the radiation belts are shown and ring current is co-located there as well. Sun is to the left. Figure from Baumjohann and Treumann (1997).

399 currents in the magnetosphere which is beyond the scope of this dissertation.

400 The idea of the magnetopause as a barrier between the solar wind and
 401 the magnetosphere is not entirely accurate due to the presence of reconnection.
 402 Reconnection was first conceived by Dungey (1961) who described the convection of
 403 Earth's magnetic field between the bow and tail regions of the magnetosphere. This
 404 process is known as the Dungey cycle and is most effective when the IMF is pointing
 405 southward as is shown in Fig. 1.6 part 1. As the IMF contacts Earth's magnetic
 406 field it reconnects with it so that Earth's magnetic field is directly connected to the
 407 IMF. Then as the solar wind flows tailward the IMF drags Earth's magnetic field
 408 towards the magnetotail as shown in Fig. 1.6 parts 2-6. As more and more magnetic
 409 field lines are draped in the magnetotail, magnetic pressure increases in the lobes
 410 which squeezes the plasma sheet until Earth's magnetic field reconnects as is shown
 411 in Fig. 1.6 part 7. Lastly, Fig. 1.6 part 8 shows the newly merged magnetic field
 412 line and the plasma frozen on it moves Earthward under the magnetic tension force
 413 to become more dipolar. This is called a dipolarization of the magnetic field, and the
 414 plasma frozen on these field lines can be observed as injections (e.g. Turner et al.,
 415 2015). Injection of plasma into the inner magnetosphere is one of the drivers of inner
 416 magnetosphere dynamics. Should I talk about the K-H instability and how there
 417 could be micro reconnection? i.e. cite a paper or two that support or refute that
 418 idea.

419 Inner Magnetosphere Populations

420 Before we describe the inner magnetosphere particle populations, we first need to
 421 describe the coordinate system used to organize the inner magnetosphere populations.
 422 The first coordinate was defined in section 1 and is the L shell. L shell can be thought
 423 of as an analogue to a radius but in a dipole geometry. The azimuthal coordinate

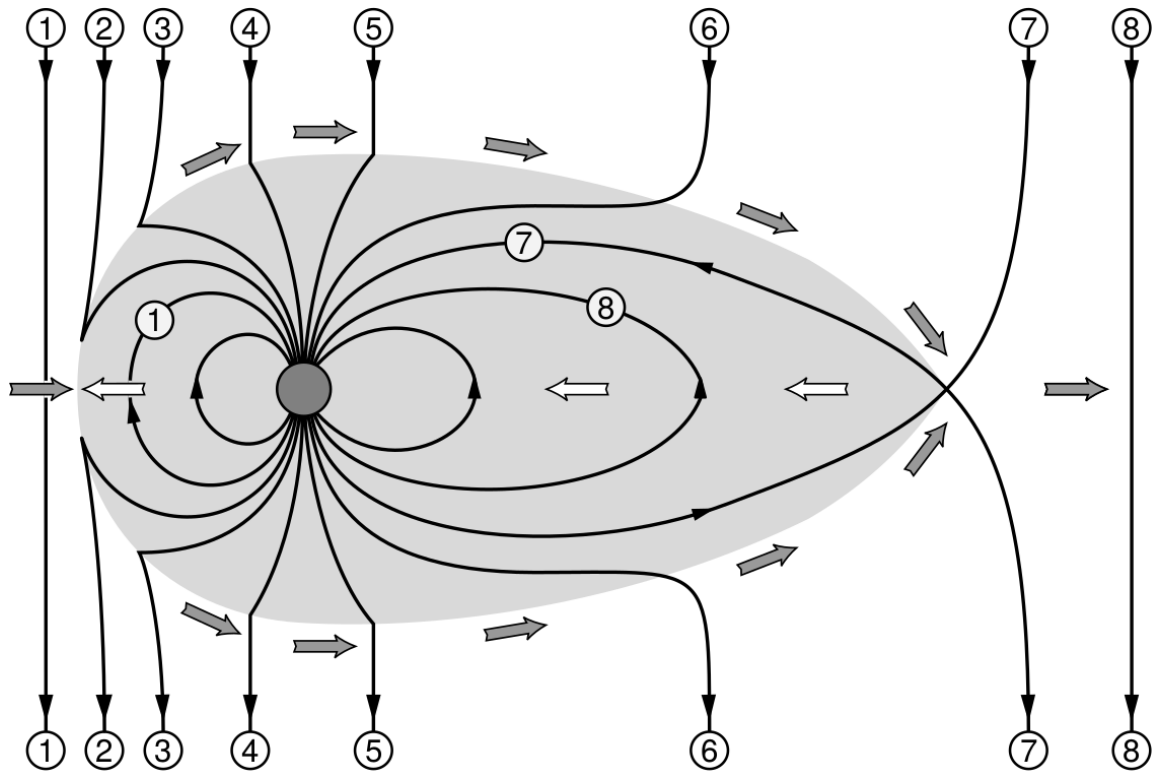


Figure 1.6: The series of steps involved in magnetic reconnection with a southward IMF. Figure from Baumjohann and Treumann (1997).

424 is the magnetic local time (MLT). For an observer above Earth's north pole looking
 425 down, MLT is defined to be 0 (midnight) in the anti-sunward direction, and increases
 426 in the counter-clockwise direction with 6 at dawn, 12 at noon (sunward direction),
 427 and 18 in dusk. The last coordinate used in this dissertation is the magnetic latitude,
 428 λ which is analogous to the latitude coordinate and is defined to be 0 at the magnetic
 429 equator.

430 The low energy particle dynamics in the inner magnetosphere are organized by
 431 two electric fields: the co-rotation and the dawn-dusk electric fields. The co-rotation
 432 electric field arises from the rotation of Earth's magnetic field. Since particles are
 433 frozen on magnetic field lines and the plasma conductivity is effectively infinite, to
 434 a non-rotating observer, Earth's rotation appears as a radial electric field that drops
 435 off as $\sim L^2$. This electric field makes particles orbit around the Earth due to the
 436 $\vec{E} \times \vec{B}$ drift. The other electric field, pointing from dawn to dusk is called the
 437 convection electric field and is formed by the Earthward transport of particles from
 438 the magnetotail that appears as an electric field to a stationary observer (with respect
 439 to Earth). The superposition of the co-rotation and convection electric fields
 440 results in a potential field shown in Fig. 1.7. The shaded area in Fig. 1.7 shows
 441 the orbits on which low energy electrons are trapped, and outside are the untrapped
 442 particles. The dynamic topology of the shaded region in Fig. 1.7 is controlled by only
 443 the convection electric field which is dependent on the solar wind speed and the IMF.
 444 The lowest energy particles, that are most effected by these electric fields, make up
 445 the plasmasphere.

446 Plasmasphere The plasmasphere is a dense ($n_e \sim 10^3/\text{cm}^3$), cool plasma
 447 ($\sim \text{eV}$) that extends to $L \sim 4$ (extent is highly dependent on the solar wind and
 448 magnetospheric conditions) and is sourced from the ionosphere. The two main

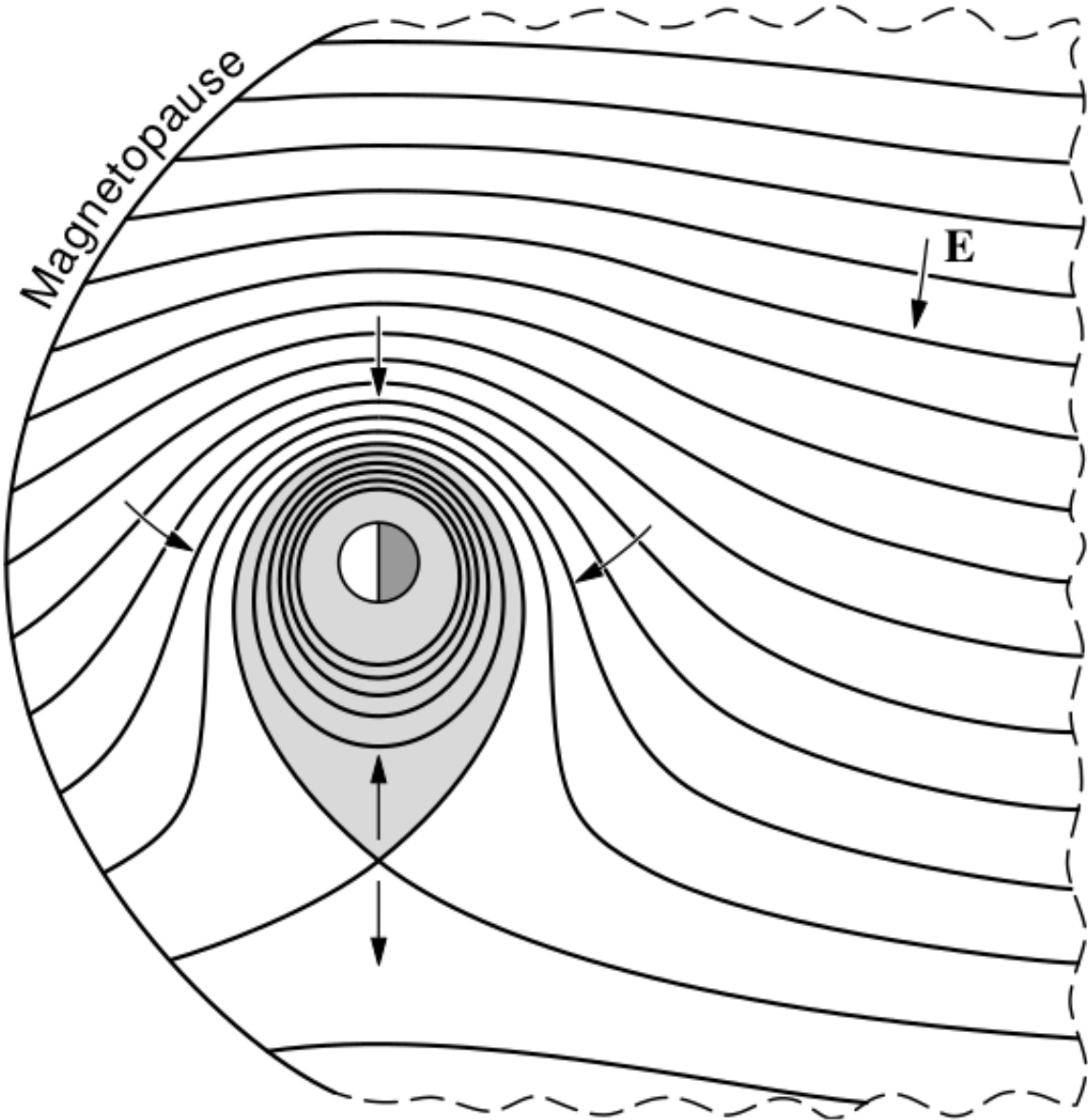


Figure 1.7: Equipotential lines and electric field arrows due to the superposition of the co-rotation and convection electric fields. Electrons in the shaded region execute closed orbits. Outside of the shaded regions the electrons are not trapped and will escape. The region separating the two regimes is called the Alfvén layer. Figure from Baumjohann and Treumann (1997).

449 mechanisms that source the cold plasma from the ionosphere are ultraviolet ionization
 450 by sunlight and particle precipitation. The ultraviolet ionization by sunlight is
 451 strongly dependent on the time of day (day vs night), latitude (more ionization near
 452 the equator). The ionization due to particle precipitation, on the other hand, is highly
 453 dependent on magnetospheric conditions, and mostly occurs at high latitudes.

454 The outer boundary of the plasmasphere is the plasmapause which is typically
 455 identified as a steep radial gradient in plasma density from $\sim 10^3/\text{cm}^3$ to $\sim 1/\text{cm}^3$. As
 456 we will see throughout this dissertation, the location of the plasmapause is important
 457 to model (e.g. O'Brien and Moldwin, 2003) and understand since the plasma density
 458 strongly controls the efficiency of particle scattering (Horne et al., 2005).

459 Ring Current The next higher energy population is the ring current. This
 460 population consists of protons and electrons between tens and a few hundred keV
 461 that drift around the Earth. The orbits of higher energy particles are not as effected
 462 by the convection and co-rotation electric field, rather they drift around the Earth
 463 due to gradient and curvature drifts. Since the direction of the drift is dependent on
 464 charge, protons drift west around the Earth and electrons drift East. This has the
 465 effect of creating a current around the Earth.

466 The ring current generates a magnetic field which decreases the magnetic field
 467 strength on Earth's surface and increases it outside of the ring current. The decrease
 468 of Earth's magnetic field strength is readily observed by a system of ground-based
 469 magnetometers and is merged into a Disturbance Storm Time (DST) index. An
 470 example of a DST index time series from a coronal mass ejection (CME) driven 2015
 471 St. Patrick's Day storm is shown in Fig. 1.8. The ring current is sometimes first
 472 depleted and DST increases slightly (initial phase or sudden storm commencement).
 473 Then the ring current is rapidly built up during which DST rapidly decreases (main

474 phase). Lastly the ring current gradually decays toward its equilibrium state over a
 475 period of a few days and DST increases towards 0 (recovery phase). The DST index
 476 along with other indicies are readily used by the space physics community to quantify
 477 the global state of the magnetosphere.

478 Radiation Belts The highest energy particle populations are in the Van Allen
 479 radiation belts. These belts were discovered by Van Allen (1959) and Vernov and
 480 Chudakov (1960) during the Cold War and are a pair of toroidally shaped populations
 481 of trapped electrons and protons usually within to $L < 8$ and are shown in Fig. 1.9.
 482 Their quiescent toroidal shape is similar to the shape of the plasmasphere and ring
 483 current and is a result of Earth's dipole magnetic field and the conservation of the
 484 three adiabatic invariants discussed in section 1.

485 The inner radiation belt is extremely stable on time periods of years, extends
 486 to $L \approx 2$, and mainly consists of protons with energies between MeV and GeV and
 487 electrons with energies up to ≈ 1 MeV (Claudepierre et al., 2019). The source of
 488 inner radiation belt protons is believed to be due to cosmic-ray albedo neutron decay
 489 (e.g. Li et al., 2017) and inward radial diffusion for electrons (e.g. O'Brien et al.,
 490 2016). The gap between the inner and outer radiation belt is called the slot, which is
 491 believed to be due to hiss waves inside the plasmasphere (described below) scattering
 492 particles into the atmosphere (e.g. Breneman et al., 2015; Lyons and Thorne, 1973).

493 The outer radiation belt, on the other hand is much more dynamic and consists
 494 of mainly electrons of energies up to a few MeV. The outer belt's spatial extent is
 495 highly variable e.g. see Fig. 1.10, and is typically observed at $4 < L < 8$. Since
 496 the outer radiation belt contains a dynamic population of energetic particles that
 497 pose a threat to human and technological presence in Earth's atmosphere and space,
 498 decades of research has been undertaken to understand and predict the outer radiation

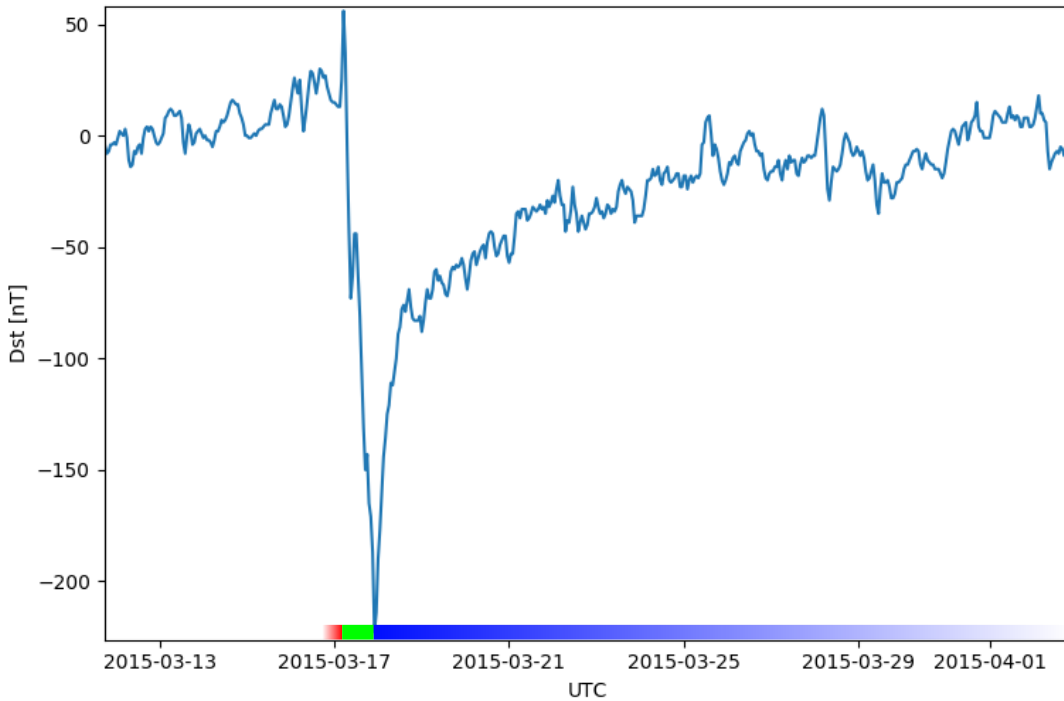


Figure 1.8: The DST index during the St. Patrick's Day 2015 storm. This storm was caused by a coronal mass ejection on March 15th, 2015. The storm phases are: initial phase, main phase, and recovery phase. The initial phase occurred when the Dst peaked at +50 nT on March 17th during which the ring current was eroded by the coronal mass ejection during the interval shown by the red bar. Then the rapid decrease to ≈ -200 nT was during the main phase where many injections from the magnetotail pumped up the ring current which reduced Earth's magnetic field strength at the ground and is shown with the green bar. Lastly, the recovery phase lasted from March 18th to approximately March 29th during which the ring current particles were lost and the ring current returned to its equilibrium state. The recovery phase is shown with the blue bar.

The Earth's Electron Radiation Belts

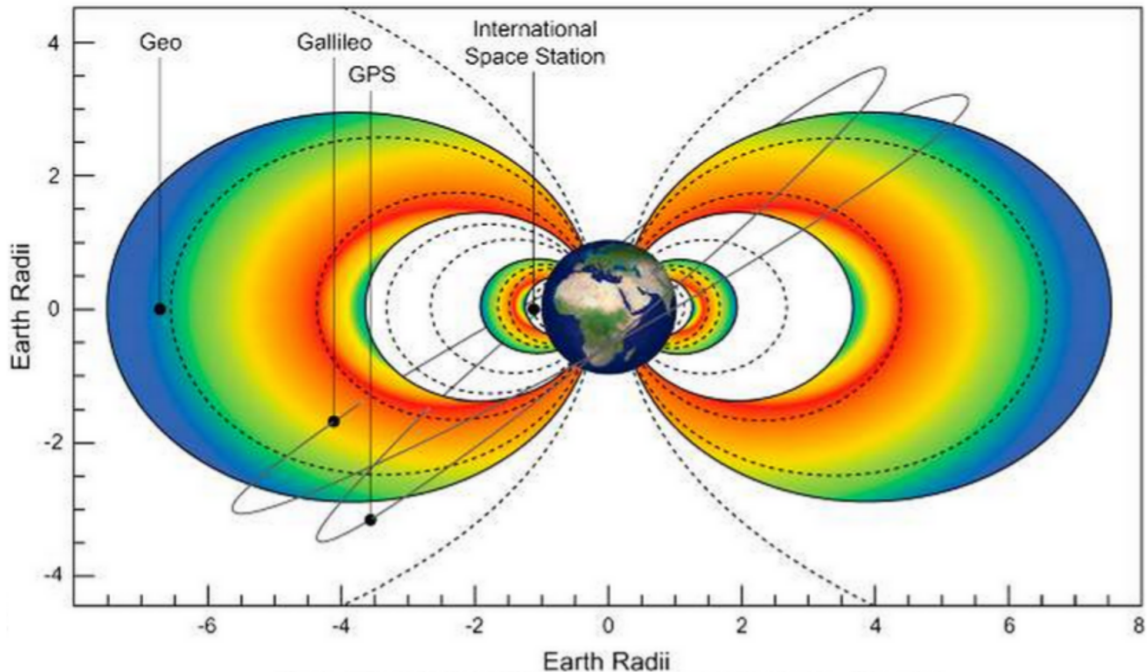


Figure 1.9: The two radiation belts with the locations of various satellites and orbits.
Figure from (Horne et al., 2013).

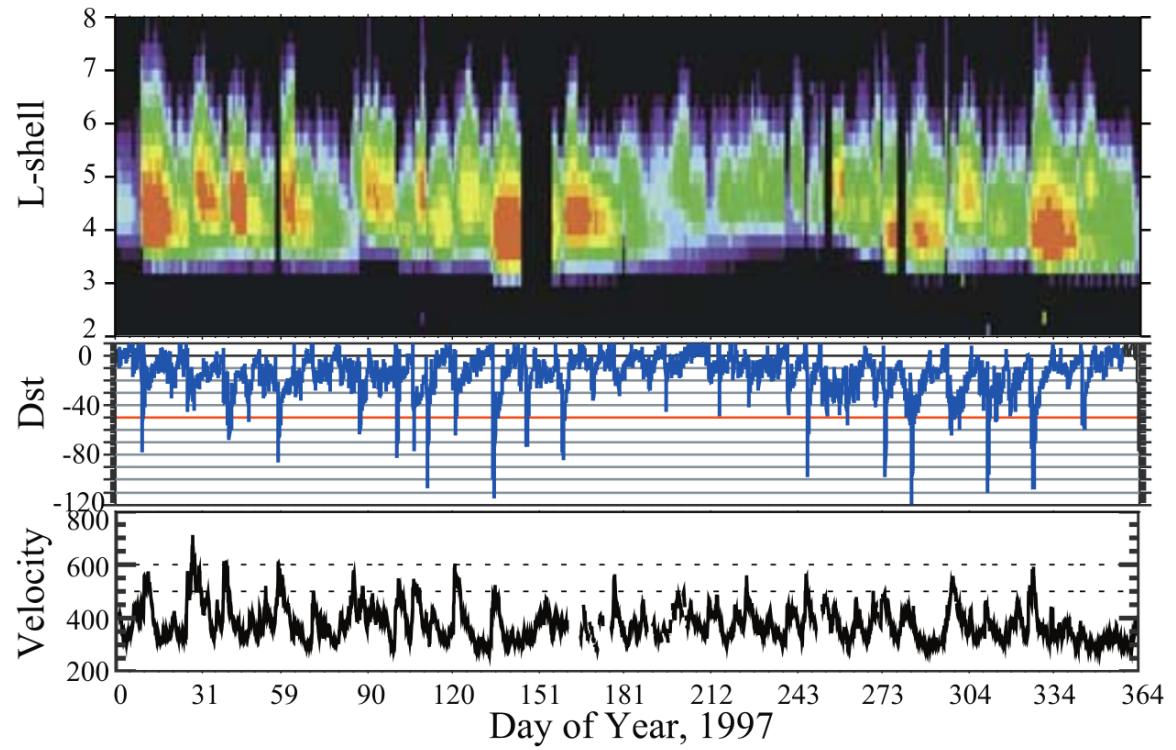


Figure 1.10: The dynamics of the outer radiation belt in 1997 from the POLAR satellite. Top panel shows the 1.2-2.4 MeV electron flux as a function of L and 1997 day of year. The middle panel shows the DST index, and bottom panel shows the solar wind velocity. Figure from (Reeves et al., 2003).

⁴⁹⁹ belt particles, waves, and wave-particle interactions. The dynamics of the outer
⁵⁰⁰ radiation belt can be understood by considering various competing acceleration and
⁵⁰¹ loss mechanisms which will be described in the following sections.

⁵⁰² Radiation Belt Particle Sources and Sinks

⁵⁰³ Adiabatic Heating

⁵⁰⁴ One of the particle heating and transport mechanisms arises from the Earthward
⁵⁰⁵ convection of particles. The conservation of J_1 implies that the initial and final v_{\perp}
⁵⁰⁶ depends on the change in the magnetic field amplitude

$$\frac{v_{\perp i}^2}{B_i} = \frac{v_{\perp f}^2}{B_f}. \quad (1.12)$$

⁵⁰⁷ As a particle convects Earthward, $B_f > B_i$ thus v_{\perp} must increase. The dipole
⁵⁰⁸ magnetic field amplitude can be written as

$$B(L, \theta) = \frac{31.2 \mu\text{T}}{L^3} \sqrt{1 + 3 \cos^2 \theta} \quad (1.13)$$

⁵⁰⁹ which implies that

$$\frac{v_{\perp f}^2}{v_{\perp i}^2} = \left(\frac{L_i}{L_f} \right)^3. \quad (1.14)$$

⁵¹⁰ .

⁵¹¹ In addition, as the particle convects Earthward the distance between the
⁵¹² particle's mirror points decrease. If J_2 is conserved, the shrinking bounce path implies
⁵¹³ that $v_{||}$ must increase by

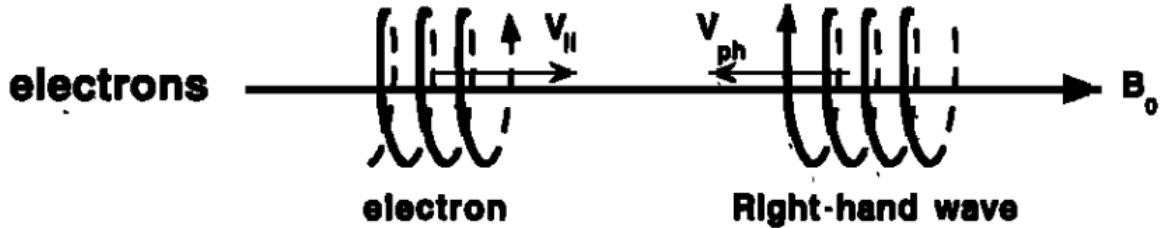
$$\frac{v_{|| f}^2}{v_{|| i}^2} = \left(\frac{L_i}{L_f} \right)^k \quad (1.15)$$

514 where k ranges from 2 for equatorial pitch angles, $\alpha_{eq} = 0^\circ$, to 2.5 for $\alpha_{eq} = 90^\circ$
 515 (Baumjohann and Treumann, 1997). Since the rate of adiabatic heating is greater in
 516 the perpendicular direction than heating in the parallel direction, an initially isotropic
 517 particle distribution will become anisotropic during its convection. These isotropic
 518 particles can then become unstable to wave growth and generate waves in order to
 519 reach equilibrium.

520 Wave Resonance Heating

521 Another mechanism that heats particles is due to particles resonating with
 522 plasma waves. A few of the electromagnetic wave modes responsible for particle
 523 acceleration (and deceleration) relevant to radiation belt dynamics are hiss, whistler
 524 mode chorus (chorus), and electromagnetic ion cyclotron (EMIC) waves. These waves
 525 are created by the loss cone instability that driven by an anisotropy of electrons
 526 for chorus waves, and protons for EMIC waves. The level of anisotropy can be
 527 quantified by the ratio of the perpendicular to parallel particle temperatures (T_\perp/T_\parallel).
 528 A particle distribution is unstable when $T_\perp/T_\parallel > 1$ which facilitates wave growth.
 529 Since electrons gyrate in a right-handed sense, the chorus waves also tend to be right
 530 hand circularly polarized (Tsurutani and Lakhina, 1997). The same argument applies
 531 to protons and left hand circularly polarized EMIC waves as well.

532 These circularly polarized waves can resonate with electrons and/or protons
 533 when their combined motion results in a static \vec{E} . One example of a resonance
 534 between a right hand circularly polarized wave and an electron is shown in Fig. 1.21
 535 and is termed the cyclotron resonance. An electron's v_\parallel and the wave's parallel wave
 536 vector, k_\parallel are in opposite directions such that the wave frequency ω is Doppler shifted
 537 to an integer multiple of the Ω_e at which point the electron feels a static electric
 538 field and is accelerated or decelerated. This acceleration happens when a resonance



$$\omega + \mathbf{k}_{\parallel} \mathbf{V}_{\parallel} = \Omega^-$$

Figure 1.11: The trajectories of an electron and a right-hand circularly polarized wave during a cyclotron resonance. The electron's v_{\parallel} and the wave's k_{\parallel} are in opposite directions such that the wave's frequency is Doppler shifted to an integer multiple of the electron cyclotron frequency. Figure from (Tsurutani and Lakhina, 1997).

539 condition is satisfied between a wave and a particle for which we will now derive an
540 illustrative toy model.

541 Assume a uniform magnetic field $\vec{B} = B_0 \hat{z}$ with a parallel propagating ($k = k \hat{z}$),
542 right-hand circularly polarized wave. The wave's electric field as a function of position
543 and time can be written as

$$\vec{E} = E_0 (\cos(\omega t - kz) \hat{x} + \sin(\omega t - kz) \hat{y}) \quad (1.16)$$

which is more clearly expressed by taking the dot product to find \vec{E} in the $\hat{\theta}$ direction

$$E_{\theta} = \vec{E} \times \hat{\theta} = E_0 \cos(\omega t - kz + \theta). \quad (1.17)$$

544 Now assume that the electron is traveling in the $-\hat{z}$ direction with a velocity $\vec{v} = -v_0 \hat{z}$
545 so its time dependent position along \hat{z} is

$$z(t) = -v_0 t \quad (1.18)$$

546 and gyrophase is

$$\theta(t) = -\Omega t + \theta(0) \quad (1.19)$$

547 where the first negative sign comes from the electron's negative charge. Now we put
548 this all together and express the electric field and the force that the electron will
549 experience

$$m \frac{dv_\theta}{dt} = qE_\theta = qE_0 \sin((\omega + kv_0 - \Omega)t + \theta(0)). \quad (1.20)$$

550 This is a relatively complex expression, but when the time dependent component,

$$\omega + kv_0 - \Omega = 0, \quad (1.21)$$

551 the electron will be in a static electric field which will accelerate or decelerate the
552 electron depending on θ_0 , the phase between the wave and the electron. **Show Bortnik**
553 **2008 plot?** The expression in Eq. 1.21 is commonly referred to as the resonance
554 condition and is more generally written as

$$\omega - k_{||}v_{||} = \frac{n\Omega_e}{\gamma} \quad (1.22)$$

555 where n is the resonance order, and γ is the relativistic correction (e.g. Millan and
556 Thorne, 2007). In the case of the cyclotron resonance, $\omega \approx \Omega_e$ thus J_1 is violated.
557 Since J_1 is violated, J_2 and J_3 are also violated since the conditions required to
558 violate J_2 and J_3 are less stringent than J_1 . It is important to remember that along
559 the particle's orbit it will encounter and experience the effects of many waves along
560 its orbit. The typical MLT extent of a handful of waves that are capable of resonating
561 with radiation belt electrons are shown in Fig. 1.12.

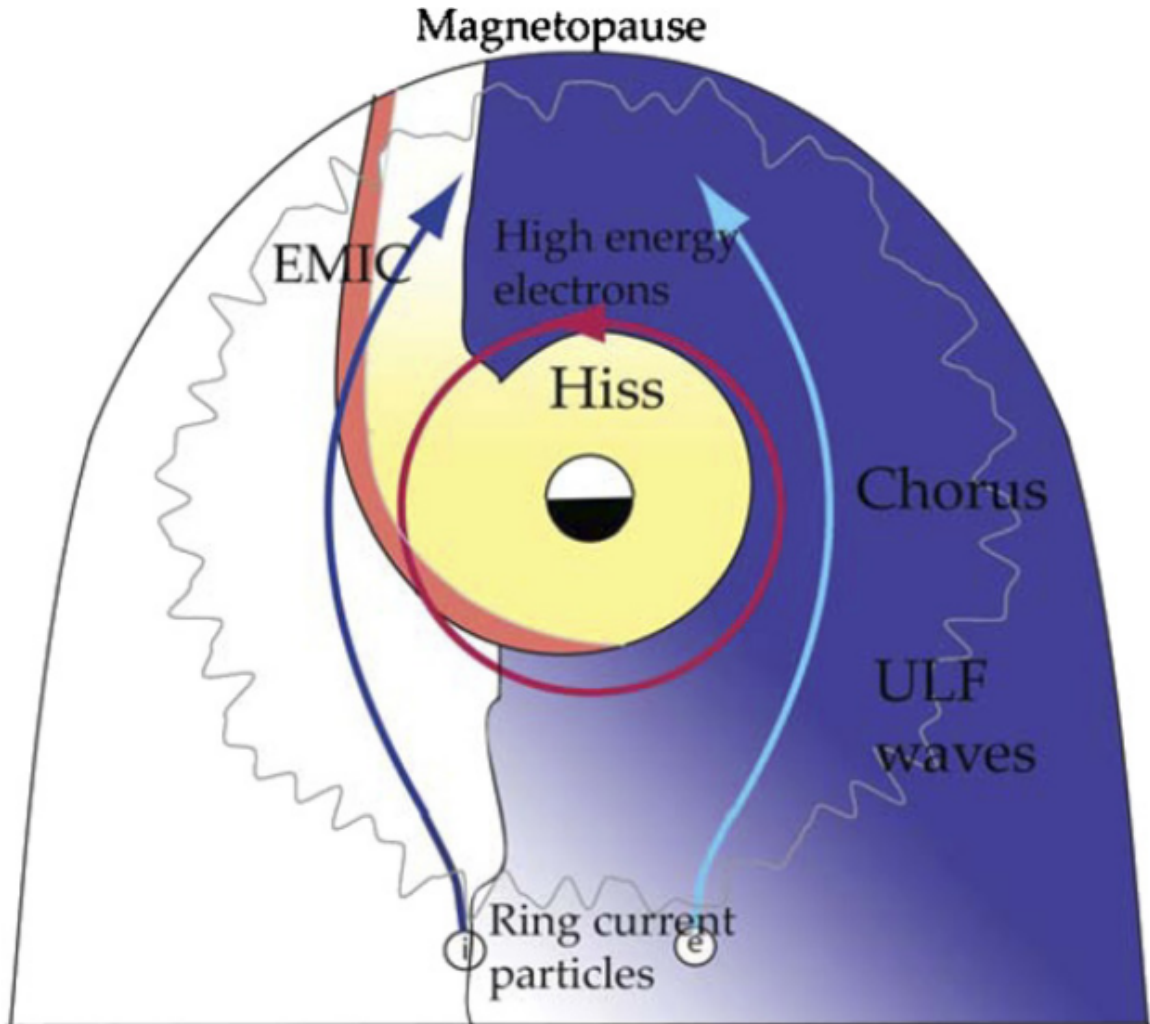


Figure 1.12: Various wave modes in the magnetosphere. Ultra low frequency waves occur through the magnetosphere. Chorus waves are typically observed in the 0-12 midnight-dawn region. EMIC waves are typically observed in the dusk MLT sector. Hiss waves are observed inside the plasmasphere. Figure from Millan and Thorne (2007).

562 Particle Losses

563 Now that we have seen two general mechanisms with which particles are
 564 accelerated and transported in the magnetosphere, we will now consider a few
 565 specific mechanisms with which particles are lost to the atmosphere or the solar
 566 wind. One particle loss mechanism into the solar wind is magnetopause shadowing
 567 (e.g. Ukhorskiy et al., 2006). Particles are sometimes lost when the ring current is
 568 strengthened and Earth's magnetic field strength is increased outside of the ring
 569 current (and reduced on Earth's surface). If the time scale of the ring current
 570 strengthening is slower than a particle drift, J_3 is conserved. Then in order to
 571 conserve J_3 while the magnetic field strength is increased, the particle's drift shell
 572 must move outward to conserve the magnetic flux contained by the drift shell. Then
 573 if the particle's drift shell expands to the point that it crosses the magnetopause, the
 574 particle will be lost to the solar wind.

575 **Move to acceleration?** Another particle loss and acceleration mechanism is driven
 576 by ultra low frequency (ULF) waves and is called radial diffusion. Radial diffusion is
 577 the transport of particles from high to low phase space density, f . If the transport is
 578 radially inward, particles will appear to be accelerated. On the other hand, radially
 579 outward radial diffusion can transport particles through the magnetopause where
 580 they will be lost to the solar wind. Reeves et al. (2013) investigated the driver of
 581 particle acceleration during the October 2012 storm and observationally found that
 582 inward radial diffusion was not dominant, rather local acceleration via wave-resonance
 583 heating (i.e. particle diffusion in pitch angle and energy which will be described below)
 584 appeared to be the dominant acceleration mechanism.

585 The loss mechanism central to this dissertation is pitch angle and energy
 586 scattering of electrons by waves. Some of the waves that scatter electrons in energy
 587 and pitch angle in the inner magnetosphere are: plasmaspheric hiss (e.g. Breneman

588 et al., 2015; O’Brien et al., 2014), EMIC waves (e.g. Capannolo et al., 2019; Hendry
 589 et al., 2017), and chorus waves (e.g. Breneman et al., 2017; Kasahara et al., 2018;
 590 Ozaki et al., 2019). These wave-particle interactions occur when the resonance
 591 condition in Eq. 1.22 is satisfied at which point the particle’s energy and α is modified
 592 by the wave. More details regarding the theory of pitch angle and energy diffusion is
 593 given in Chapter X. If the wave changes α towards 0 such that $\alpha < \alpha_{LC}$, the particle’s
 594 mirror point lowers to less than 100 km altitude where the particle can be lost due
 595 collisions with air. One manifestation of pitch angle scattering of particles into the
 596 loss cone are microbursts: a sub-second durtaison impulse of electrons.

597

Microbursts

598 Microbursts were first identified in high altitude balloon observations of bremsstrahlung
 599 X-rays emitted by microburst electrons impacting the atmosphere by Anderson and
 600 Milton (1964). Since then, other balloons have observed microburst X-ray signatures
 601 in the upper atmosphere (e.g. Anderson et al., 2017; Barcus et al., 1966; Brown et al.,
 602 1965; Parks, 1967; Trefall et al., 1966; Woodger et al., 2015). In addition to their X-ray
 603 signature, microbursts electrons have been directly observed in LEO with spacecraft
 604 including the Solar Anomalous and Magnetospheric Particle Explorer (SAMPEX),
 605 Focused Investigation of Relativistic Electron Bursts: Intensity, Range, and Dynamics
 606 II (FIREBIRD-II), Science Technologies Satellite (STSAT-I) (e.g. Blake et al., 1996;
 607 Blum et al., 2015; Breneman et al., 2017; Crew et al., 2016; Lee et al., 2012, 2005;
 608 Lorentzen et al., 2001a,b; Nakamura et al., 1995, 2000; O’Brien et al., 2004, 2003).
 609 An example microburst time series is shown in Fig. 1.13 and was observed by
 610 Montana State University’s (MSU) FIREBIRD-II CubeSats. The prominent features
 611 of microbursts in Fig. 1.13 are their ± 1 second duration, half order of magnitude
 612 increase in count rate above the falling background, and their approximately 200-800

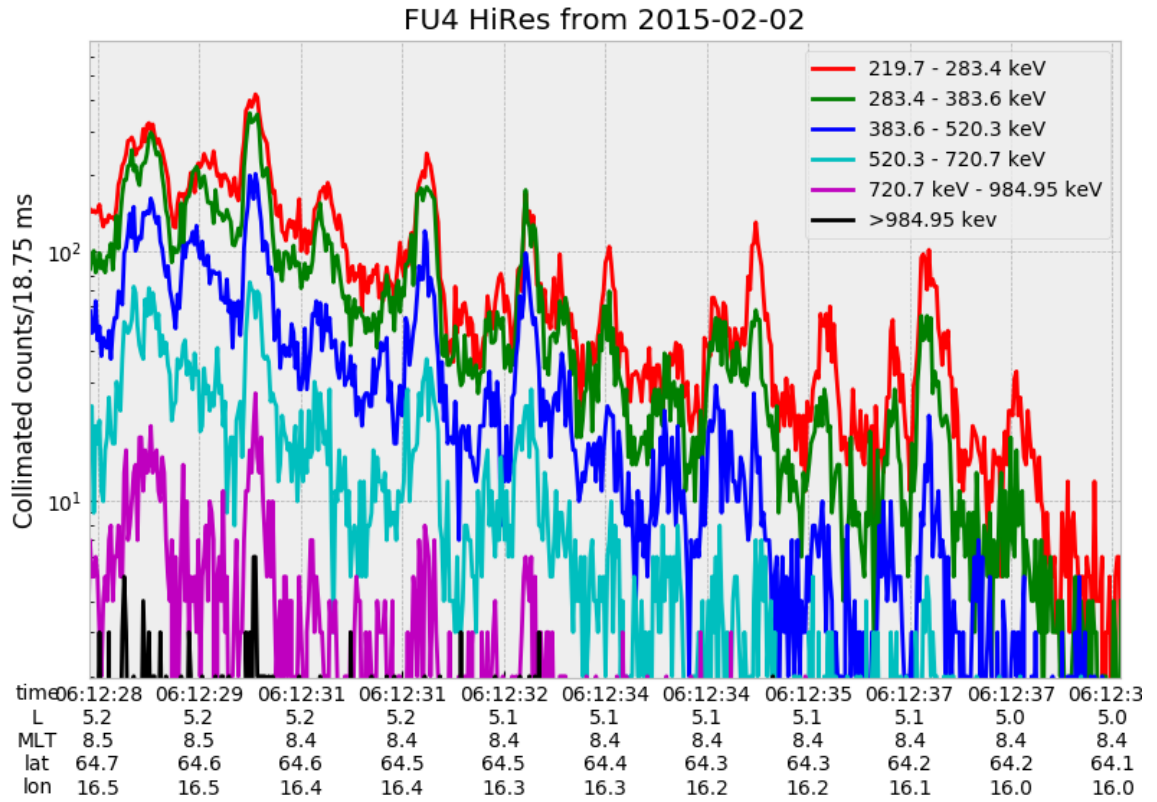


Figure 1.13: An example train of microbursts observed by FIREBIRD-II unit 4 on February 2nd, 2015. The colored curves show the differential energy channel count rates in six channels from ≈ 200 keV to greater than 1 MeV. The x-axis labels show auxiliary information such as time of observation and the spacecraft position in L, MLT, latitude and longitude coordinates.

613 keV energy extent.

614 Microbursts are observed on magnetic field footprints that are connected to the
 615 outer radiation belt (approximately $4 < L < 8$), and are predominately observed in
 616 the 0-12 MLT sector with an elevated occurrence frequency during magnetospherically
 617 disturbed times as shown in Fig. 1.14. Microbursts have been previously observed
 618 over a wide energy range from a few tens of keV (Datta et al., 1997; Parks, 1967) to
 619 greater than 1 MeV (e.g. Blake et al., 1996; Greeley et al., 2019). The microburst

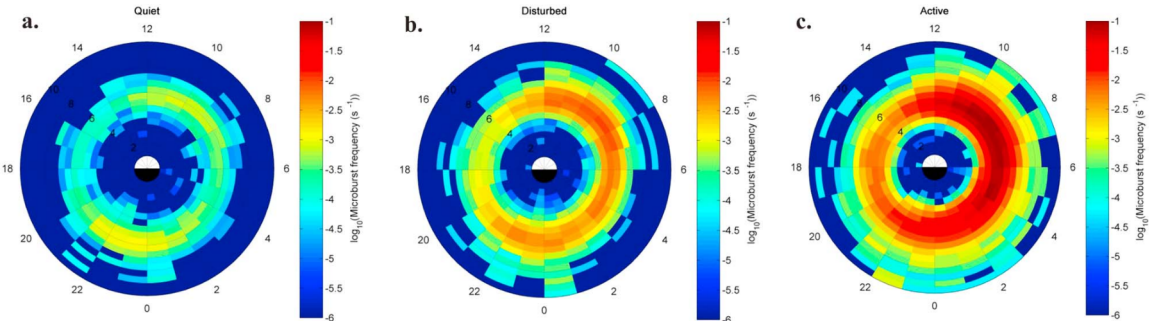


Figure 1.14: Relativistic ($> 1\text{MeV}$) distribution of microburst occurrence rates as a function of L and MLT. The three panels show the microburst occurrence rate dependence on geomagnetic activity, parameterized by the auroral electrojet (AE) index for (a) $\text{AE} < 100 \text{ nT}$, (b) $100 < \text{AE} < 300 \text{ nT}$ and (c) $\text{AE} > 300 \text{ nT}$. Figure from Douma et al. (2017).

620 electron flux (J) falls off in energy, and the microburst energy spectra is typically
 621 well fit to a decaying exponential

$$J(E) = J_0 e^{-E/E_0} \quad (1.23)$$

622 where J_0 is the flux at 0 keV (unphysical free parameter) and E_0 quantifies the
 623 efficiency of the scattering mechanism in energy (.e.g Datta et al., 1997; Lee et al.,
 624 2005; Parks, 1967). A small E_0 suggests that mostly low energy particles are scattered
 625 and a high E_0 suggests that the scattering mechanism scatters low and high energy
 626 electrons. Reality is a bit more messy and a high E_0 may be a signature of a scattering
 627 mechanism preferential to high energy electrons, but is hidden by the convolution of
 628 the source particles available to be scattered (typically with a falling energy spectrum)
 629 and the energy-dependent scattering efficiency.

630 The short duration of microbursts observed by a single LEO satellite has an
 631 ambiguity when interpreting what is exactly a microburst. The two possible realities
 632 are: a microburst is very small and spatially stationary so that the LEO spacecraft

633 passes through it in less than a second. Alternatively, microbursts are spatially large
 634 with a short duration such that the microburst passes by the spacecraft in a fraction
 635 of a second. There are a few ways to distinguish between the two possible realities,
 636 and each one has a unique set of advantages.

637 A high altitude balloon provides essentially a stationary view of the precipitating
 638 particles under the radiation belt footprints so a short-lived, temporal microburst
 639 can be unambiguously identified. Spatial structures on the other hand are difficult
 640 to identify because a balloon is essentially still on drift timescales thus a variation in
 641 the X-rays can be due to the spatial structure or an increase of precipitating particles
 642 over the whole area. Furthermore, if the stationary structure is drifting its particles
 643 are not precipitating into the atmosphere so there is no X-ray signature.

644 Another solution is multi-spacecraft missions that can determine if a microburst
 645 is spatial or temporal. As will be shown in this dissertation, if a microburst is
 646 observed simultaneously by two spacecraft then it is temporally transient and has
 647 a size greater than the spacecraft separation. On the other hand, if two spacecraft
 648 observe a microburst-like feature in the same location and at different times, then it is
 649 spatial may be a curtain (Blake and O'Brien, 2016). Both observational methods have
 650 a unique set of strengths, and this dissertation takes the multi-spacecraft approach
 651 to identify and study microbursts.

652

Scope of Research

653 This dissertation furthers our understanding of the microburst scattering
 654 mechanism by observing the scattering directly, and measuring the microburst sizes
 655 and comparing them to the size of waves near the magnetic equator where those
 656 electrons could have been scattered. Chapter X describes a microburst scattering
 657 event observed by NASA's Van Allen Probes which was studied in the theoretic

658 framework of pitch angle and energy diffusion. The following two chapters will then
659 study the size of microbursts. Chapter Y describes a bouncing packet microburst
660 observation made by MSU's FIREBIRD-II mission where the microburst's lower
661 bound longitudinal and latitudinal sizes were estimated. Then Chapter Z expands
662 the case study from Ch. Y to a statistical study of microburst sizes using The
663 Aerospace Corporation's AeroCube-6 (AC6) CubeSats. In this study, a Monte Carlo
664 and analytic microburst size models were developed to account for the compounding
665 effects of random microburst sizes and locations. Lastly, Ch. A will summarize the
666 dissertation work and make concluding remarks regarding outstanding questions in
667 microburst physics.

668

CHAPTER TWO

669

EVIDENCE OF MICROBURSTS OBSERVED NEAR THE EQUATORIAL

670

PLANE IN THE OUTER VAN ALLEN RADIATION BELT

671

Contribution of Authors and Co-Authors

672 Manuscript(s) in Chapter(s) 1

673

674 Author: [type author name here]

675 Contributions: [list contributions here, single-spaced]

676 Co-Author: [type co-author name here]

677 Contributions: [list contributions here, single-spaced]

678 Co-Author: [type co-author name here]

679 Contributions: [list contributions here, single-spaced]

680

681

Manuscript Information

682 [Type Author and Co-author(s) Names Here]

683 Geophysical Research Letters

684 Status of Manuscript: Published in a peer-reviewed journal

685 Wiley

686 Volume 45, Issue 16

687

Key Points

- 688 ● First report of direct observation of microbursts at high altitude, near the
689 equatorial plane.
- 690 ● Microbursts' duration, flux enhancement, and energy spectra are similar to prior
691 observations in LEO.
- 692 ● Microburst generation is not consistent with a single quasi-linear gyroresonant
693 interaction with chorus waves.

694

Abstract

695 We present the first evidence of electron microbursts observed near the equatorial
696 plane in Earth's outer radiation belt. We observed the microbursts on March 31st,
697 2017 with the Magnetic Electron Ion Spectrometer and RBSP Ion Composition
698 Experiment on the Van Allen Probes. Microburst electrons with kinetic energies
699 of 29-92 keV were scattered over a substantial range of pitch angles, and over time
700 intervals of 150-500 ms. Furthermore, the microbursts arrived without dispersion in
701 energy, indicating that they were recently scattered near the spacecraft. We have
702 applied the relativistic theory of wave-particle resonant diffusion to the calculated
703 phase space density, revealing that the observed transport of microburst electrons is
704 not consistent with the hypothesized quasi-linear approximation.

705

Introduction

706 Since the Van Allen radiation belts were discovered by Van Allen (1959) and
707 Vernov and Chudakov (1960), decades of work has focused on understanding their
708 origins and effects on the near-Earth space environment and ionosphere-thermosphere

709 system. The energy content of the outer belt is dominated by energetic electrons,
 710 with dynamics controlled by a complex interplay between various source and loss
 711 mechanisms. One important loss and acceleration mechanism is gyroresonant
 712 diffusion in energy and pitch angle (PA) due to scattering of electrons by plasma
 713 waves (e.g. Bortnik et al., 2008; Horne and Thorne, 2003; Meredith et al., 2002;
 714 Millan and Thorne, 2007; Summers et al., 1998; Thorne and Andreoli, 1981; Thorne
 715 et al., 2005; Walker, 1993).

716 Chorus waves are commonly associated with PA and energy diffusion. These
 717 waves are typically generated by substorm injections into the inner magnetosphere,
 718 which lead to a temperature anisotropy of the source electrons with energies up to
 719 tens of keV (e.g. Horne et al., 2003; Li et al., 2009a). Since these source electrons
 720 drift eastward, chorus is most frequently observed in the dawn sector, but it has
 721 been observed at all magnetic local times (MLT) (Li et al., 2009b). Chorus waves
 722 are believed to generate electron microburst precipitation through wave-particle
 723 interactions.

724 Microbursts are typically defined as an increase of electron flux in or near the
 725 atmospheric loss cone that last < 1 s (e.g. Anderson and Milton, 1964; Blake et al.,
 726 1996; Lorentzen et al., 2001a). Empirical and theoretical analyses indicate that
 727 microbursts are an important loss process since they can substantially deplete the
 728 radiation belt electrons on the order of one day (e.g. Breneman et al., 2017; Lorentzen
 729 et al., 2001b; O'Brien et al., 2004; Thorne et al., 2005). Previously, microbursts have
 730 been observed in the upper atmosphere in the form of bremsstrahlung X-rays (e.g.
 731 Anderson et al., 2017; Parks, 1967; Woodger et al., 2015) and directly in low Earth
 732 orbit (LEO) (e.g. Blake et al., 1996; Blum et al., 2015; Breneman et al., 2017; Crew
 733 et al., 2016; Lee et al., 2012, 2005; Lorentzen et al., 2001a,b; Mozer et al., 2018;
 734 Nakamura et al., 1995, 2000; O'Brien et al., 2004, 2003).

735 We observed for the first time, microburst-like signatures near their hypothesized
 736 origin within the heart of the outer radiation belt. The unique microburst
 737 observations we report here were possible with the Van Allen Probe-A's (RBSP-
 738 A) Magnetic Electron Ion Spectrometer's (MagEIS) fast sampling rate (\sim 11 ms),
 739 and RBSP Ion Composition Experiment's (RBSPICE) PA coverage. The observed
 740 microbursts' duration, energy spectra, and energy dispersion signature were similar to
 741 microbursts previously reported from LEO. Furthermore, we simultaneously observed
 742 structureless "hiss-like" whistler mode wave power in the lower band chorus frequency
 743 range (Li et al., 2012). From previous observations in LEO (e.g. Blake et al., 1996),
 744 it is believed that microbursts result from the impulsive scattering of electrons into
 745 or near the loss cone, which is on the order of a few tens of degrees in LEO. With this
 746 assumption, high altitude microburst observations near the magnetic equator should
 747 be very difficult to make since the atmospheric loss cone there is only a few degrees
 748 wide. Thus, the loss cone is smaller than the angular resolution of most particle
 749 detectors. Even when an instrument is observing the loss cone, the instrument's field
 750 of view will include some portion of the trapped population. The trapped electron flux
 751 is typically orders of magnitude higher than that in the loss cone, so that microbursts
 752 scattered into the loss cone will be obscured. We present observational evidence that
 753 suggests that the sudden impulse of electrons studied here is consistent with the
 754 creation of microbursts. Furthermore, these microbursts were scattered over a broad
 755 PA range outside of the loss cone, though the loss cone was not directly observed by
 756 MagEIS and RBSICE.

757 This paper explores the properties of the observed microbursts by utilizing in-
 758 situ RBSP measurements of waves and particles. This unique high altitude point of
 759 view enables us to test whether the observed microburst scattering is consistent with
 760 a quasi-linear diffusion process. We have tested this hypothesis with in-situ electron

761 phase space density (PSD) measurements and the relativistic theory of wave-particle
 762 resonant diffusion (Summers et al., 1998; Walker, 1993) to determine if the microburst
 763 electrons diffused in PA and energy.

764

Spacecraft Instrumentation

765 NASA's RBSP mission (Mauk et al., 2013), launched on August 30th, 2012,
 766 consists of a pair of identically instrumented spacecraft. Their orbit and instru-
 767 mentation are uniquely configured to enrich our understanding of the particles and
 768 waves in the inner magnetosphere. The RBSP spacecraft are in highly elliptical, low-
 769 inclination orbit, with perigee of \sim 600 km and apogee of \sim 30,000 km altitude. Their
 770 attitude is maintained by spin-stabilization with a period of \sim 11 s and the spin axis is
 771 roughly sun-pointing. In this analysis, energetic electron measurements from MagEIS
 772 (Blake et al., 2013) and RBSPICE (Mitchell et al., 2013) were used, complemented by
 773 magnetic field and wave measurements from Electric and Magnetic Field Instrument
 774 and Integrated Science (EMFISIS) (Kletzing et al., 2013).

775 We observed these microbursts with RBSP-A's MagEIS low energy instrument
 776 (MagEIS-A) which measures 20-240 keV electrons. It has an angular acceptance
 777 of $3^\circ - 10^\circ$ in the spacecraft spin plane, and 20° perpendicular to the spin plane.
 778 MagEIS-A has a high rate data mode which samples at 1000 angular sectors per
 779 spacecraft spin (11 ms cadence). MagEIS low on RBSP-B on the other hand samples
 780 at 64 angular sectors per spacecraft spin (172 ms cadence), so it was only used for
 781 context.

782 To expand the PA coverage of MagEIS-A, we used the RBSPICE-A time-of-
 783 flight instrument. RBSPICE-A measures electron energies in the range of 19 keV -
 784 1 MeV with a fan of six telescopes (the sixth telescope is used only for calibration
 785 and was excluded from this analysis). These telescopes have an overall acceptance

786 angle of 160° by 12° which allows them to simultaneously sample a substantial part
 787 of the Pitch Angle Distribution (PAD). RBSPICE-A gathers data over 32 sectors
 788 per spacecraft spin (≈ 310 ms cadence) and each sector is divided into three sub-
 789 sectors corresponding to three measurement modes (Manweiler and Zwiener, 2018).
 790 At the time of the observation, the sub-sector used for electron measurements had
 791 an accumulation time of 77 ms. We used RBSPICE-A's Electron Basic Rate (EBR)
 792 telemetry data in this analysis which is not averaged, though it is an integral energy
 793 channel.

794 To understand the dynamics of the local magnetic field, we used the EMFISIS
 795 instrument. EMFISIS provides measurements of the DC magnetic field with flux gate
 796 magnetometers. In addition, it measures electromagnetic waves from 10 Hz to 500
 797 kHz with search coil magnetometers. The spectral matrix and burst data products
 798 used in this analysis were from the EMFISIS waveform receiver (WFR) (10 Hz - 12
 799 kHz) and the high frequency receiver (10 kHz - 500 kHz). Burst data were selectively
 800 captured at a 35 kHz sample rate, and the survey mode spectral matrix data was
 801 captured every 6s.

802

Observations

803 MagEIS-A and RBSPICE-A observed the microburst-like signatures on March
 804 31st, 2017 at $L^* \approx 6$ and $MLT \approx 19$, calculated with the Tsyganenko 2004 magnetic
 805 field model (Tsyganenko and Sitnov, 2005). The magnetosphere was in the recovery
 806 phase of a storm, with minimum Dst of -75 nT observed on March 27th. The local
 807 electron number density was on the order of 1 cm^{-3} at this time, so both RBSP
 808 spacecraft were located outside the plasmasphere. The two spacecraft were separated
 809 by 1700 km, at magnetic latitudes $\lambda \approx -19^\circ$ and $\lambda \approx -18^\circ$ for RBSP-A and RBSP-B,
 810 respectively.

811 MagEIS-A observed microburst electron flux (J) at energies ± 92 keV around
 812 11:17 UT as shown in panel (a) in Fig. 2.1. For directional information, panel (b)
 813 in Fig. 2.1 shows flux as a function of local pitch angle (α_L) and time for 46-66 keV
 814 electrons. Electrons that traveled towards the northern hemisphere had $\alpha_L < 90^\circ$ and
 815 southern hemisphere had $\alpha_L > 90^\circ$. The interval between the two vertical dashed
 816 black lines contain the four microbursts examined in this study. We observed these
 817 microbursts at $\alpha_L < 50^\circ$, but MagEIS-A did not sample into the 0° loss cone.

818 Figure 2.1 panel (c) shows the EMFISIS WFR data from RBSP-A. Between
 819 11:17:05 and 11:17:10 UT, we observed an isolated burst of whistler mode wave power
 820 in the frequency range $0.1 < \omega < 0.3 \Omega_{ce0}$, where Ω_{ce0} is the equatorial electron
 821 gyrofrequency. No individual rising or falling tone elements were observed during
 822 this period, and the waves appeared more “hiss-like” (e.g. Li et al., 2012). This wave
 823 was near-parallel propagating (evidence shown in Appendix A) and about 10 minutes
 824 later, weak chorus rising tone elements were observed (not shown).

825 Panels (d)-(f) in Fig. 2.1 are in the same format as panels (a)-(c), but for RBSP-
 826 B. An injection or boundary was observed with RBSP-B at 11:16:50 UT and RBSP-A
 827 observed a similar feature soon after 11:18 UT (not shown).

828 A zoomed-in version of Fig. 2.1 panels (a) and (b) is shown in Fig. 2.2. Panel
 829 (a) shows the four microburst-like signatures observed between 11:17:10 and 11:17:12
 830 UT, at energies up to 92 keV. The observed duration of the microbursts was 150
 831 - 500 ms, and they did not arrive dispersed in energy, which indicates that they
 832 were recently scattered near the spacecraft location. We use IRBEM-Lib, a library
 833 dedicated to radiation belt modeling (Boscher et al., 2012), to calculate the mirror
 834 point altitudes, which were found to be above LEO. Panel (b) shows the RBSPICE-
 835 A EBR time series with the group of microbursts observed at the same time as
 836 in panel (a). To understand the timing relationship between the MagEIS-A and

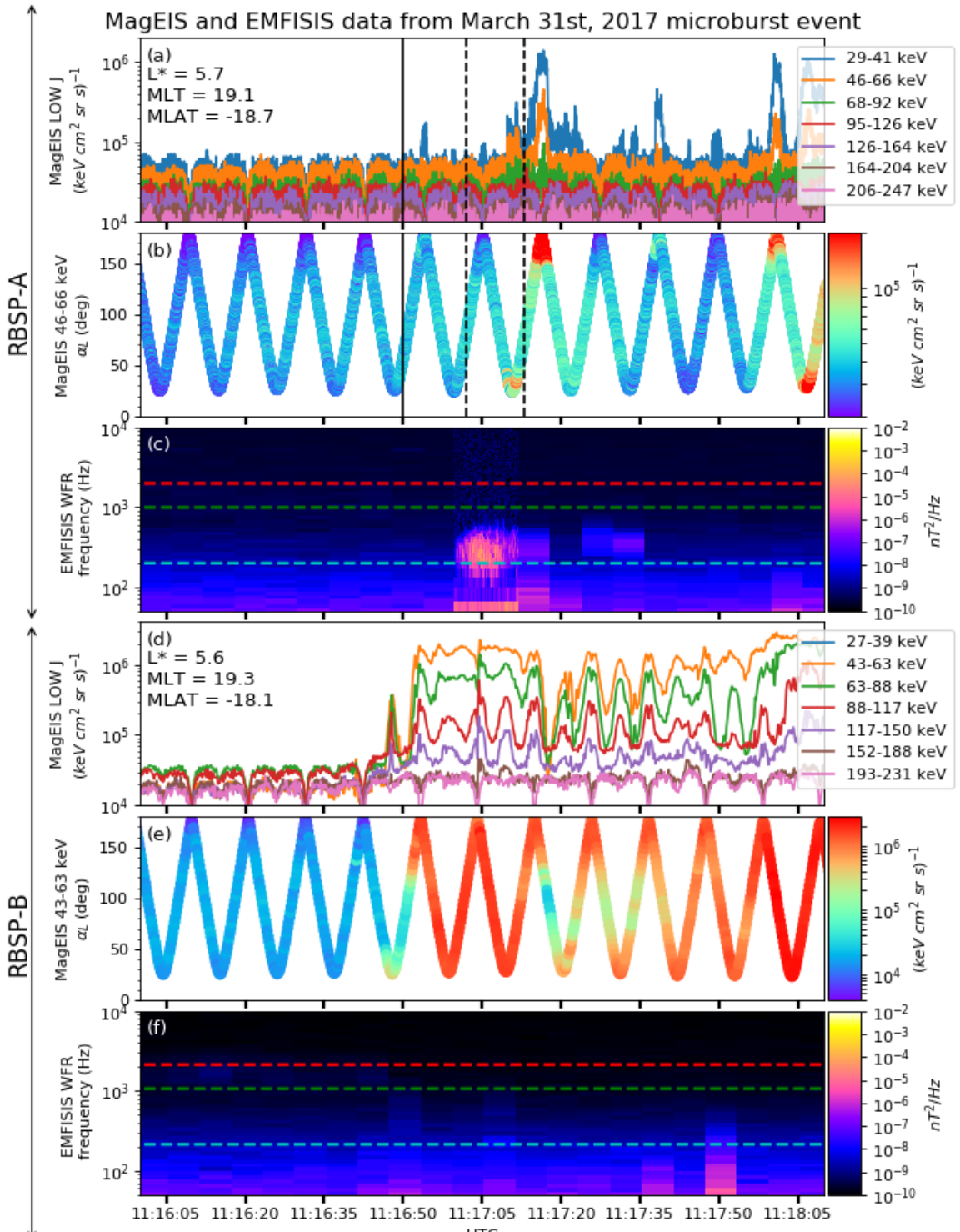


Figure 2.1: Electron and wave conditions from the MagEIS-A and EMFISIS WFR sensors for the microburst time interval. Panels (a), (b), and (c) are from RBSP-A with its position information annotated in panel (a). Panels (d), (e), and (f) are from RBSP-B with its position information annotated in panel (d). Panel (a) is the MagEIS-A high rate timeseries. Panels (b) and (e) show the evolution of the MagEIS-A J as a function of α_L from the ~ 40 to ~ 60 keV channel. Every 10th point is shown in panel (b). The solid black line in panels (a) and (b) mark the end of the time period used for the PSD fit extrapolation analysis explained in section

837 RBSPICE-A observations, we marked the times when MagEIS-A observed the four
 838 microbursts by vertical black arrows in panels (a) and (b). MagEIS-A observed the
 839 first microburst ~ 0.5 s before RBSPICE-A. The bounce period of locally mirroring,
 840 100 keV electrons was ~ 0.8 s, so this was unlikely to have been a returning bounce.
 841 This evidence confirms that these microburst signatures are packets of electrons and
 842 not a boundary moving back and forth at RBSP-A's location. To understand the
 843 PA extent of these microbursts, panel (c) shows the 29-41 keV MagEIS-A J and
 844 RBSPICE-A EBR as a function of α_L and time. The microburst J was observed
 845 by MagEIS-A between $25^\circ < \alpha_L < 50^\circ$ and RBSPICE-A between $100^\circ < \alpha_L < 160^\circ$,
 846 with the highest intensities close to $\alpha_L = 90^\circ$. RBSPICE-A observed a 10-80%
 847 enhancement in count rate over those PAs with the evidence presented in Appendix
 848 A.

849 Analysis

850 First, we estimated the microburst energy spectra. For each microburst shown in
 851 Fig. 2.2, its flux was averaged and baseline subtracted using the method from O'Brien
 852 et al. (2004) and then fit with an exponential function. The calculated exponential
 853 E-folding energy was found to vary between 25 and 35 keV, which is consistent with
 854 spectra derived from prior measurements (Datta et al., 1997; Lee et al., 2012, 2005).

855 We then tested the hypothesis that the microburst electrons were transported
 856 in energy and PA by a single chorus wave. We used a procedure similar to sections
 857 3.1 and 4.5 in Meredith et al. (2002) which we describe below.

858 Microburst and Source PSD

859 We estimated the electron PSD, $f(p_\perp, p_\parallel)$ where p_\perp and p_\parallel are the perpendicular
 860 and parallel components of the electron momentum relative to the local magnetic field,

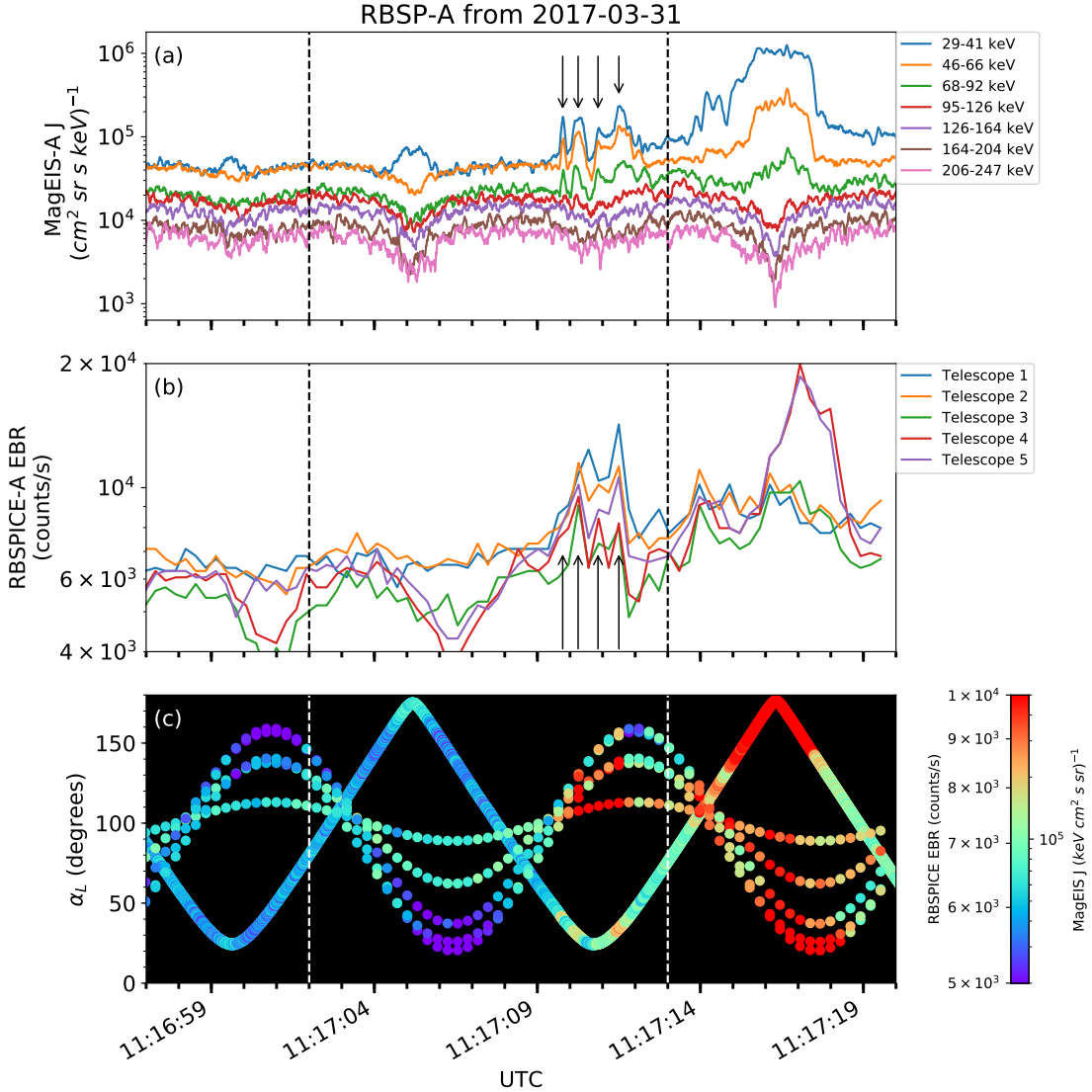


Figure 2.2: Panel (a) shows the MagEIS-A high rate timeseries. Panel (b) shows the RBSPIKE EBR count rate timeseries for $\zeta = 19$ keV electrons. The microbursts were observed between 11:17:10 - 11:17:12 UT and are indicated with the vertical black arrows in panels (a) and (b) for MagEIS-A times. Panel (c) shows the RBSPIKE EBR (family of relatively sparse sampled curves) and MagEIS-A J from the 29-41 keV energy channel (single curve) as a function of α_L . The vertical dashed lines show the time interval for the PSD analysis.

for the microburst time period. MagEIS-A $J(E, \alpha_L)$ was averaged between 11:17:02 and 11:17:13 UT and binned by α_L into 5° bins. Then, we assumed the conservation of the first adiabatic invariant and mapped α_L to equatorial PA, α_{eq} . The binned $J(E, \alpha_{eq})$ was then converted to $f(p_\perp, p_\parallel)$ via

$$f(p_\perp, p_\parallel) = \frac{J(E, \alpha_{eq})}{p^2}, \quad (2.1)$$

where $p = \sqrt{p_\perp^2 + p_\parallel^2}$. Lastly, α_{eq} was used to separate p into p_\perp and p_\parallel via

$$\frac{p_\parallel}{m_e c} = \frac{\sqrt{E(E + 2E_0)} \cos(\alpha_{eq})}{E_0} \quad (2.2)$$

$$\frac{p_\perp}{m_e c} = \frac{\sqrt{E(E + 2E_0)} \sin(\alpha_{eq})}{E_0} \quad (2.3)$$

where c is the speed of light, E is the kinetic energy, m_e is the electron mass, and E_0 is the electron rest energy. The observed $f(p_\perp, p_\parallel)$ in dimensionless momentum space is shown in Fig. 2.3 in all panels between the p_\parallel axis and the white dotted lines. The bright spot in $f(p_\perp, p_\parallel)$ in the upper p_\parallel plane represents the four microbursts. Along with the observed PSD, we use Fig. 2.3 to explore the various PSD extrapolation and diffusion model assumptions which are described below.

We proceed under the assumption that the source of the microburst electrons is not likely to be at the latitude of the observation, and is closer to the magnetic equator. To look for a source of microburst electrons, we extrapolate the unobserved $f(p_\perp, p_\parallel)$ of electrons with $|\lambda_m| < 19^\circ$ using two cases with a 90° -peaked PAD of the form

$$f(E, \alpha_{eq}) = f_0(E) \sin^n(\alpha_{eq}) \quad (2.4)$$

where $f_0(E)$ is a scaling parameter and n is a power parameter. Similarly to the

873 in-situ $f(p_{\perp}, p_{\parallel})$, the $f(E, \alpha_{eq}) \mapsto f(p_{\perp}, p_{\parallel})$ conversion was applied.

874 In the first case, we fitted Eq. 2.4 to the quiet time $J(E, \alpha_{eq})$ from 11:15:00 to
 875 11:16:50 UT (end time shown as the black vertical line in Fig. 2.1). The fitted
 876 PAD was relatively flat with $0.4 < n < 0.5$ and highest magnitude of f_0 was
 877 $0.05 c^3/(cm MeV)^3$. This extrapolated $f(p_{\perp}, p_{\parallel})$ is shown in Fig. 2.3 panels (A) and
 878 (E), between the dotted white lines for scattering at $\lambda = 0^\circ$ and 20° , respectively.
 879 To confirm the relatively low n parameter, we found times where RBSP-A was in
 880 a similar L-MLT location, but closer to the magnetic equator. At 2 and 19 UT on
 881 the same day, we fit the $J(E, \alpha_{eq})$, and the fit parameters were very similar to the
 882 pre-microburst $f(p_{\perp}, p_{\parallel})$ at 11 UT. Thus it is a reasonable assumption that $f(p_{\perp}, p_{\parallel})$
 883 was relatively flat near the equator.

884 In the other case, we estimate how large n would have to be in order to find
 885 sufficient PSD in MagEIS-A's energy range to be a source of the microburst electrons.
 886 We used $n \in \{1, 2, 4\}$ and we forced the $f_0(E)$ parameter to match the observed
 887 $f(p_{\perp}, p_{\parallel})$ at the most equatorial PAs observed by MagEIS-A. These extrapolations
 888 are shown in columns 2-4 in Fig. 2.3. There was enough source PSD anywhere in
 889 MagEIS-A's energy range only if $n \geq 2$.

890 Motion of resonant electrons in phase space

To calculate the motion of resonant electrons in momentum space, we used the relativistic theory of wave-particle resonant diffusion developed by Walker (1993) and Summers et al. (1998) and applied in Meredith et al. (2002). The chorus wave can modify $f(p_{\perp}, p_{\parallel})$ when a resonance condition is satisfied. The cyclotron resonance condition between an electron with velocity $v = \sqrt{v_{\parallel}^2 + v_{\perp}^2}$ and a parallel propagating

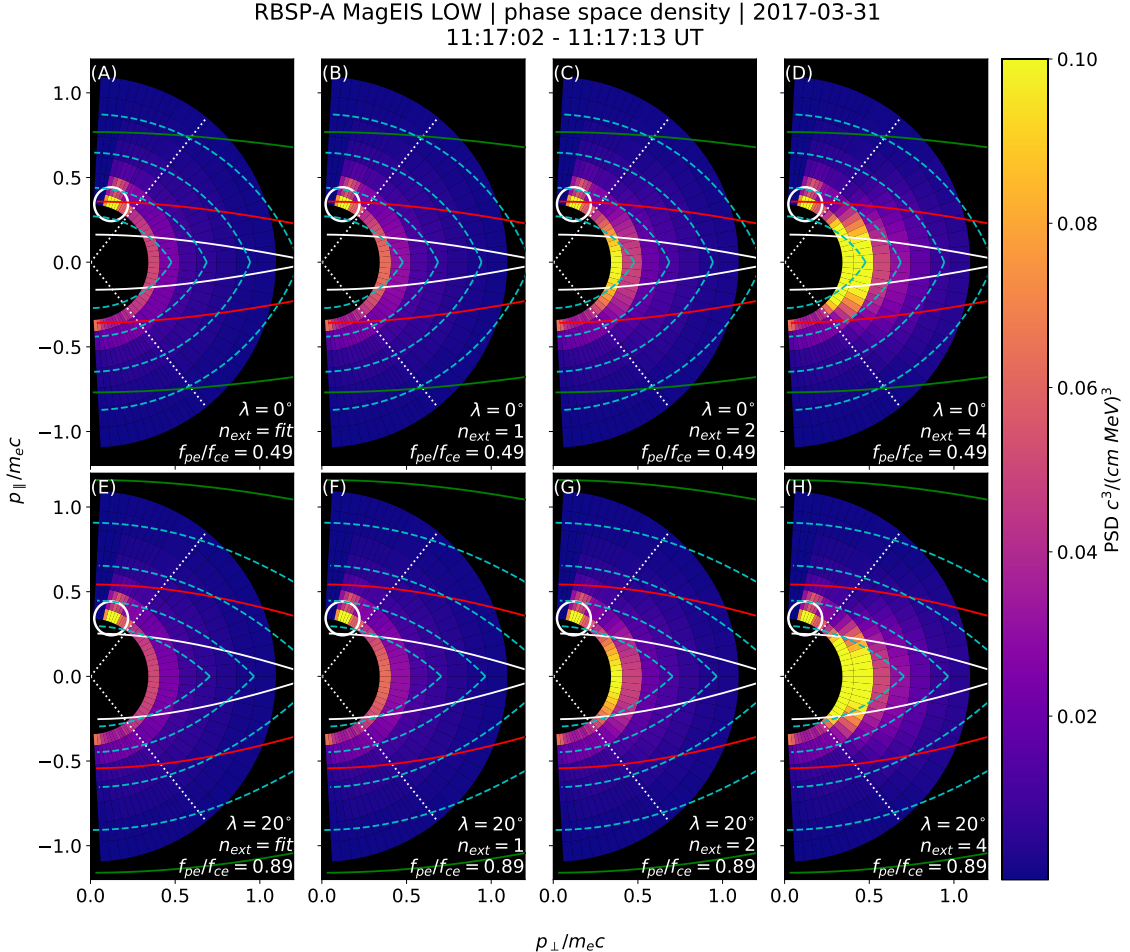


Figure 2.3: The colored annulus represents $f(p_{\perp}, p_{\parallel})$ in normalized momentum space, parallel and perpendicular to the background magnetic field. The microburst $f(p_{\perp}, p_{\parallel})$ is highlighted with the white circle. The columns show different powers of the sine extrapolation, and rows show the different magnetic latitudes of the scattering. The white dotted traces represent the boundary between the data and extrapolation. The green, red, and white solid traces are the resonance curves for $\omega = 0.2\Omega_{ce}$, $0.4\Omega_{ce}$, $0.6\Omega_{ce}$, respectively. The cyan dashed traces are the diffusion curves for a $\omega = 0.4\Omega_{ce}$ wave (waves of other frequency have similar diffusion curves). The magnetic latitude of the scattering, the ratio of the plasma to the cyclotron frequency, and the power of the sine extrapolation is annotated in each panel. For the resonance and diffusion curves, the density model assumed a $n_L = 1 e^-/cm^3$ and $\psi = -1$.

wave of frequency ω and wave number k_{\parallel} is given by

$$\omega - v_{\parallel} k_{\parallel} = \frac{\Omega_{ce}}{\gamma}, \quad (2.5)$$

where Ω_{ce} is the electron gyrofrequency at the scattering location, and γ is the relativistic correction. Assuming the cold plasma approximation,

$$k_{\parallel} = \frac{\omega}{c} \sqrt{1 - \frac{\omega_{pe}^2}{\omega(\omega - |\Omega_{ce}|)}}, \quad (2.6)$$

where ω_{pe} is the plasma frequency. For a particular set of parameters, Eq. 2.5 defines a curve in momentum space that describes which electrons will resonate with a monochromatic wave.

To calculate k_{\parallel} , we approximated the electron number density, $n_e(\lambda)$ locally and at the magnetic equator. Locally, the plasma density was approximately $n_e(\lambda = -20^\circ) = n_L \approx 1 \text{ cm}^{-3}$. We used magnetospheric seismology techniques (e.g. Takahashi and Denton, 2007) to parameterize $n_e(\lambda)$ elsewhere along the field line with

$$n_e(\lambda) = n_e(0) \left(\frac{LR_e}{R(\lambda)} \right)^{\psi} \quad (2.7)$$

where R_e is the Earth's radius, $R(\lambda)$ is the radial distance from the Earth to the spacecraft, and ψ is the exponent parameter. Assuming a dipole magnetic field for which $R(\lambda) = LR_e \cos^2 \lambda$ (e.g. Schulz and Lanzerotti, 1974), we can express Eq. 2.7 in terms of n_L via

$$n_e(\lambda) = n_L \left(\frac{\cos \lambda_L}{\cos \lambda} \right)^{2\psi} \quad (2.8)$$

where we used $\psi = -1$ (higher density at the magnetic equator) in this analysis. We chose this exponent parameter because it is a realistic best case scenario for the

901 electrons to be transported along the diffusion curves (described below).

Walker (1993) and Summers et al. (1998) argued that a resonant electron will move along diffusion curves in momentum space. A diffusion curve is derived as follows. In the reference frame moving with a monochromatic chorus wave's phase velocity (wave frame), the chorus wave is stationary and there is no electric field. Thus in the wave frame, the electron's kinetic energy is conserved, and the electron's velocity in the wave frame can be expressed in differential form as

$$v_{\parallel}dv_{\parallel} + v_{\perp}dv_{\perp} = 0. \quad (2.9)$$

After a Lorentz transformation of Eq. 2.9 into the magnetosospheric frame, kinetic energy will no longer be conserved. After integration and manipulation of Eq. 2.9, we obtain:

$$\left(1 - \frac{u_0^2 v_0^2}{c^4}\right)v_{\parallel}^2 - 2u_0\left(1 - \frac{v_0^2}{c^2}\right)v_{\parallel} + \left(1 - \frac{u_0^2}{c^2}\right)v_{\perp}^2 = v_0^2 - u_0^2 \quad (2.10)$$

902 where $u_0 = \omega/k_{\parallel}$ is the phase velocity, and v_0 is a constant of integration (Summers
 903 et al., 1998; Walker, 1993). Equation 2.10 defines a family of diffusion curves in
 904 momentum space on which resonant electrons will move. The distance that an
 905 electron moves along a diffusion curve is a function of wave and plasma parameters,
 906 and is estimated from the magnitude of the diffusion coefficients and the resonance
 907 time.

908 Comparing the microburst PSD to diffusion theory

909 Superposed on the PSD plots in Fig. 2.3 are resonance curves for chorus waves
 910 of $\omega = 0.2\Omega_{ce}$, $0.4\Omega_{ce}$, $0.6\Omega_{ce}$ and a few diffusion curves for a $\omega = 0.4\Omega_{ce}$ wave.
 911 These curves were parameterized by λ using a dipole magnetic field for $\lambda = 0^\circ$

(Fig. 2.3, panels A-D) and $\lambda = 20^\circ$ (Fig. 2.3, panels E-H). If the transport of microburst electrons is consistent with gyro-resonant diffusion, a diffusion curve that passes through the microburst $f(p_\perp, p_\parallel)$ must also pass through another region with at least the same magnitude PSD ($f(p_\perp, p_\parallel) \geq 0.1 \text{ c}^3/(\text{cm MeV})^3$) e.g. Fig. 2.3, panel (D). With this constraint, an artificially high extrapolated $f(p_\perp, p_\parallel)$ with $n > 2$ (5 times larger than calculated from the fits) must be assumed for there to have been a sufficient source of PSD anywhere in MagEIS-A's energy range.

We now show that by comparing MagEIS observations with theory, that the minimum wave amplitude necessary to scatter these electrons is much higher than was observed by EMFISIS-A. If we assume a unrealistic PAD with enough PSD just equatorward of RBSP-A, we can use MagEIS-A observations to calculate the minimum $\Delta\alpha_{eq}$ that the electrons were transported. We then used diffusion theory to calculate the necessary wave amplitude. For microbursts with larger PAs, MagEIS-A observed a transport of $\Delta\alpha_{eq} = 9^\circ$ and for microbursts with smaller PAs, the observed transport was $\Delta\alpha_{eq} = 24^\circ$. The required wave amplitude was calculated with Eq. 3 from Thorne and Andreoli (1981) assuming a maximum resonance period of a quarter bounce. The observed change in PA requires a wave amplitude $0.2 < |B_w| < 0.5 \text{ nT}$. For a few brief moments, the EMFISIS-A WFR waveform data showed $0.1 < |B_w| < 0.15 \text{ nT}$, so a transport of 9° is plausible, but not likely for 24° .

Another source of microburst electrons may be from energies below MagEIS-A's range. The Helium, Oxygen, Proton, and Electron mass spectrometer (Funsten et al., 2013) on RBSP-A observed $f(p_\perp, p_\parallel) \geq 0.1 \text{ c}^3/(\text{cm MeV})^3$ for $\gtrsim 23 \text{ keV}$ electrons at this time. We then assumed the wave amplitude derived above to predict the transport in energy. We used the fact that the momentum and pitch angle diffusion coefficients, D_{pp} and $D_{\alpha\alpha}$ are related via $D_{pp}/p^2 \sim D_{\alpha\alpha}$ or equivalently, $\Delta p/p \sim \Delta\alpha$. The observed PA transport corresponds to an energy transport of $6 < \Delta E < 16$

938 keV. Therefore, this wave can transport 23 keV electrons from smaller pitch angles
 939 to larger pitch angles and would be observed in the 29 – 41 keV MagEIS-A channel.
 940 However, this wave is insufficient to transport electrons to the 68 – 92 keV channel
 941 in one interaction. Therefore we conclude that quasi-linear diffusion cannot explain
 942 the observed microbursts.

943

Discussion and Conclusions

944 These novel observations of impulsive electron signatures reported here fall
 945 well within the broad definition of a microburst as described in section 3. Their
 946 properties were similar to microbursts observed in LEO, with an E-folding energy of
 947 $25 < E_0 < 35$ keV (Datta et al., 1997; Lee et al., 2012, 2005), duration of 150-500
 948 ms (Lorentzen et al., 2001a), observed upper energy limit of 92 keV, and a lack of
 949 clear energy dispersion (Breneman et al., 2017). With MagEIS-A’s high time and
 950 energy resolution, we conclude that these dispersionless microbursts were recently
 951 scattered near the spacecraft. Furthermore, RBSPICE-A’s PA coverage suggests
 952 that these electrons were scattered over a substantial range of PAs, with the highest
 953 intensities near $\alpha_L = 90^\circ$. Overall, our observational evidence suggests that on time
 954 scales shorter than one bounce period, the chorus wave effectively accelerated trapped
 955 electrons over a broad PA range.

956 In the theoretical framework of wave-particle resonant diffusion applied to the
 957 observed PSD in section 3, we determine that the observed scattering is not consistent
 958 with the quasi-linear approximation. The nearest source of sufficient PSD is too
 959 far away in phase space to have been transported by the hypothesized quasi-linear
 960 process over a timescale shorter than one bounce period (one interaction). A similar
 961 conclusion was made by Mozer et al. (2018) who used quasi-linear theory constrained
 962 by RBSP wave measurements. They successfully modeled the one second average

963 precipitating flux observed with AeroCube-6 (AC-6) CubeSats during a conjunction,
 964 but they were unable to model the AC-6 fluxes on smaller time scales.

965 To put these microburst observations into a wider magnetospheric perspective,
 966 we observed them during the recovery phase of a minimum Dst of -75 nT storm, a
 967 statistically favorable time period for microbursts (O'Brien et al., 2003). Furthermore,
 968 during the same storm on March 27th, the Arase spacecraft observed highly correlated
 969 lower band chorus with 10-50 keV electron precipitation inside the loss cone. At
 970 that time, Arase's magnetic field footprint was near The Pas All-Sky Imager (part
 971 of the THEMIS mission) which simultaneously observed pulsating auroral patches
 972 (Kasahara et al., 2018). While microbursts and pulsating auroral patches have not
 973 been clearly connected, they are both believed to be a product of electron scattering
 974 by whistler mode waves (e.g. Lorentzen et al., 2001a; Nishimura et al., 2011; O'Brien
 975 et al., 2003; Ozaki et al., 2012).

976 The combined capabilities of the various RBSP wave and particle instruments
 977 enable comprehensive studies of wave-particle scattering and the resulting microburst
 978 precipitation. From a preliminary search by the authors, other microburst-like
 979 signatures have been found with RBSP. Similar to previous studies (e.g. Blum et al.,
 980 2015; O'Brien et al., 2003), a statistical study of high-altitude microbursts in L-MLT
 981 space needs to be conducted before we can verify that these microbursts are the
 982 counterpart of the microbursts observed in LEO and the upper atmosphere.

983 Acknowledgments

984 The authors acknowledge the technicians, engineers, and scientists who made the
 985 RBSP and AC-6 missions possible. One author (Shumko) would like to acknowledge
 986 Dana Longcope for his help in understanding the quasi-linear diffusion theory. Dr.
 987 Gkioulidou was supported by JHU/APL subcontract 131803 to the NJIT under NASA

988 Prime contract NNN06AA01C. EMFISIS work was supported by JHU/APL contract
989 no. 921647 under NASA Prime contract No. NAS5-01072. The MagEIS instrument
990 was funded by NASA's Prime contract no. NAS5-01072. The level 3 MagEIS-A
991 "high rate" data is available in the Supporting Information, level 1 RBSPICE EBR
992 data is archived at <http://rbspicea.ftecs.com/>, and the EMFISIS level 2 spectral
993 matrix and burst data as well as the level 3 magnetometer data is archived at
994 <http://emfisis.physics.uiowa.edu/data/index>. The IRBEM Library can be obtained
995 at irbem.sf.net.

996

CHAPTER THREE

997

MICROBURST SCALE SIZE DERIVED FROM MULTIPLE BOUNCES OF A

998

MICROBURST SIMULTANEOUSLY OBSERVED WITH THE FIREBIRD-II

999

CUBESATS

1000

Contribution of Authors and Co-Authors

1001 Manuscript(s) in Chapter(s) 1

1002

1003 Author: [type author name here]

1004 Contributions: [list contributions here, single-spaced]

1005 Co-Author: [type co-author name here]

1006 Contributions: [list contributions here, single-spaced]

1007 Co-Author: [type co-author name here]

1008 Contributions: [list contributions here, single-spaced]

1009

1010

Manuscript Information

1011 [Type Author and Co-author(s) Names Here]

1012 Geophysical Research Letters

1013 Status of Manuscript: Published in a peer-reviewed journal

1014 Wiley

1015 Volume 45, Issue 17

1016

1017 This article is available under the terms of the Creative Commons Attribution

1018 Non-Commercial No Derivatives License CC BY-NC-ND (which may be updated

1019 from time to time) and permits non-commercial use, distribution, and reproduction

1020 in any medium, without alteration, provided the original work is properly cited and

1021 it is reproduced verbatim.

1022

Key Points

1023

- Multiple bounces from a microburst were observed by the two FIREBIRD-II CubeSats at LEO.
- The lower bounds on the microburst scale size at LEO were 29 ± 1 km (latitudinal) and 51 ± 11 km (longitudinal).
- Deduced lower bound equatorial scale size was similar to the whistler-mode chorus source scale.

1029

Abstract

1030

We present the observation of a spatially large microburst with multiple bounces made simultaneously by the FIREBIRD-II CubeSats on February 2nd, 2015. This is the first observation of a microburst with a subsequent decay made by two co-orbiting but spatially separated spacecraft. From these unique measurements, we place estimates on the lower bounds of the spatial scales as well as quantify the electron bounce periods. The microburst's lower bound latitudinal scale size was 29 ± 1 km and the longitudinal scale size was 51 ± 1 km in low earth orbit. We mapped these scale sizes to the magnetic equator and found that the radial and azimuthal scale sizes were at least 500 ± 10 km and 530 ± 10 km, respectively. These lower bound equatorial scale sizes are similar to whistler-mode chorus wave source scale sizes, which supports the hypothesis that microbursts are a product of electron scattering by chorus waves. Lastly, we estimated the bounce periods for 200-800 keV electrons and found good agreement with four common magnetic field models.

1043

Introduction

1044 The dynamics of radiation belt electrons are complex, and are driven by
 1045 competition between source and loss processes. A few possible loss processes are
 1046 radial diffusion (Shprits and Thorne, 2004), magnetopause shadowing (Ukhorskiy
 1047 et al., 2006), and pitch angle and energy diffusion due to scattering of electrons by
 1048 plasma waves (e.g. Abel and Thorne, 1998; Horne and Thorne, 2003; Meredith et al.,
 1049 2002; Mozer et al., 2018; Selesnick et al., 2003; Summers et al., 1998; Thorne et al.,
 1050 2005). There are a variety of waves that cause pitch angle scattering, including
 1051 electromagnetic ion cyclotron waves, plasmaspheric hiss, and chorus (Millan and
 1052 Thorne, 2007; Thorne, 2010). Chorus predominantly occurs in the dawn sector (6-12
 1053 magnetic local times (MLT)) (Li et al., 2009b) where it accelerates electrons with
 1054 large equatorial pitch angles and scatters electrons with small equatorial pitch angles
 1055 (Horne and Thorne, 2003). Some of these electrons may be impulsively scattered
 1056 into the loss cone, where they result in short-duration (~ 100 ms) enhancements in
 1057 precipitating flux called microbursts.

1058 Anderson and Milton (1964) coined the term microburst to describe high altitude
 1059 balloon observations of ~ 100 ms duration enhancements of bremsstrahlung X-
 1060 rays emitted from scattered microburst electrons impacting the atmosphere. Since
 1061 then, non-relativistic (less than a few hundred keV) microbursts have been routinely
 1062 observed with other balloon missions (e.g. Anderson et al., 2017; Parks, 1967; Woodger
 1063 et al., 2015). A review of the literature shows no reports of microbursts above a few
 1064 hundred keV observed by balloons (Millan et al., 2002; Woodger et al., 2015). This
 1065 lack of observation may be explained by relatively weaker pitch angle scattering of
 1066 relativistic electrons by chorus (Lee et al., 2012).

1067 In addition to the X-ray signature for bursts of electron precipitation, the

1068 precipitating relativistic and non-relativistic electrons have been measured in situ by
 1069 spacecraft orbiting in low earth orbit (LEO). Hereinafter, we refer to these electron
 1070 signatures observed by LEO spacecraft also as microbursts. Microbursts have been
 1071 observed with, e.g. the Solar Anomalous and Magnetospheric Particle Explorer's
 1072 (SAMPEX) \gtrsim 150 keV and \gtrsim 1 MeV channels (Blake et al., 1996; Blum et al., 2015;
 1073 Lorentzen et al., 2001a,b; Nakamura et al., 1995, 2000; O'Brien et al., 2004, 2003) and
 1074 Focused Investigation of Relativistic Electron Bursts: Intensity, Range, and Dynamics
 1075 (FIREBIRD-II) with its \gtrsim 200 keV energy channels (Anderson et al., 2017; Breneman
 1076 et al., 2017; Crew et al., 2016).

1077 Understanding microburst precipitation and its scattering mechanism is impor-
 1078 tant to radiation belt dynamics. The scattering mechanism has been observationally
 1079 studied by e.g. Lorentzen et al. (2001b) who found that microbursts and chorus
 1080 waves predominantly occur in the dawn sector and Breneman et al. (2017) made
 1081 a direct observational link between individual microbursts and chorus elements.
 1082 Microbursts have been modeled and empirically estimated to be capable of depleting
 1083 the relativistic electron population in the outer radiation belt on the order of a day
 1084 (Breneman et al., 2017; O'Brien et al., 2004; Shprits et al., 2007; Thorne et al., 2005).
 1085 An important parameter in this estimation of instantaneous radiation belt electron
 1086 losses due to microbursts is their scale size. Parks (1967) used balloon measurements
 1087 of bremsstrahlung X-rays to estimate the high altitude scale size of predominantly low
 1088 energy microbursts to be 40 ± 14 km. In Blake et al. (1996) a microburst with multiple
 1089 bounces was observed by SAMPEX, and the microburst's latitudinal scale size in LEO
 1090 was estimated to have been "at least a few tens of kilometers". Blake et al. (1996)
 1091 concluded that typically microbursts are less than a few tens of electron gyroradii in
 1092 size (at $L = 5$ at LEO, the gyroradii of 1 MeV electrons is on the order of 100 m).
 1093 Dietrich et al. (2010) used SAMPEX along with ground-based very low frequency

1094 stations to conclude that during one SAMPEX pass, the observed microbursts had
1095 scale sizes less than 4 km.

1096 Since February 1st, 2015, microbursts have been observed by FIREBIRD-II, a
1097 pair of CubeSats in LEO. Soon after launch, when the two FIREBIRD-II spacecraft
1098 were at close range, a microburst with a scale size greater than 11 km was observed
1099 (Crew et al., 2016). On the same day, FIREBIRD-II simultaneously observed a
1100 microburst with multiple bounces. The microburst decay was observed over a period
1101 of a few seconds, while the spacecraft were traveling predominantly in latitude. Here
1102 we present the analysis and results of the latitude and longitude scale sizes and
1103 bounce periods of the first microburst with multiple bounces observed with the two
1104 FIREBIRD-II spacecraft.

1105 Spacecraft and Observation

1106 The FIREBIRD missions are comprised of a pair of identically-instrumented
1107 1.5U CubeSats (15 x 10 x 10 cm) that are designed to measure electron precipitation
1108 in LEO (Klumpar et al., 2015; Spence et al., 2012). The second mission, termed
1109 FIREBIRD-II, was launched on January 31st 2015. The two FIREBIRD-II CubeSats,
1110 identified as Flight Unit 3 (FU3) and Flight Unit 4 (FU4), were placed in a 632 km
1111 apogee, 433 km perigee, and 99° inclination orbit (Crew et al., 2016). FU3 and FU4
1112 are orbiting in a string of pearls configuration with FU4 ahead, to resolve the space-
1113 time ambiguity of microbursts. Each FIREBIRD-II unit has two solid state detectors:
1114 one is mounted essentially at the spacecraft surface, covered only by a thin foil acting
1115 as a sun shade, with a field of view of 90° (surface detector), and the other is beneath
1116 a collimator which restricts the field of view to 54° (collimated detector). Only FU3
1117 has a functioning surface detector, so this analysis utilizes the collimated detectors.
1118 FU3's surface and collimated detectors, as well as FU4's collimated detector observe

1119 electron fluxes in six energy channels from ~ 230 keV to > 1 MeV. FIREBIRD-II's
 1120 High Resolution (HiRes) electron flux data is gathered with an adjustable sampling
 1121 period of 18.75 ms by default and can be as fast as 12.5 ms.

1122 On February 2nd, 2015 at 06:12 UT, both FIREBIRD-II spacecraft simulta-
 1123 neously observed an initial microburst, followed by subsequent periodic electron
 1124 enhancements of diminishing amplitude shown in Fig. 3.1. This is thought to be
 1125 the signature of a single burst of electrons, some of which precipitate, but the rest
 1126 mirror near the spacecraft then bounce to the conjugate hemisphere where they mirror
 1127 again and the subsequent bounces produce a train of decaying peaks (Blake et al.,
 1128 1996; Thorne et al., 2005). This bounce signature occurred during the transition
 1129 between the main and recovery phases of a storm with a minimum Dst of -44 nT
 1130 ($K_p = 4$, and $AE \approx 400$ nT). At this time, the HiRes data was sampled at 18.75 ms.
 1131 Five peaks were observed by both spacecraft. The fifth peak observed by FU4 was
 1132 comparable to the Poisson noise and was not used in this analysis. This microburst
 1133 was observed from the first energy channel ($\approx 200 - 300$ keV), to the fourth energy
 1134 channel ($\approx 500 - 700$ keV), and FU3's surface detector observed the microburst up
 1135 to the fifth energy channel (683 - 950 keV).

1136 The HiRes data in Fig. 3.1 shows signs of energy dispersion, characterized by
 1137 higher energy electrons arriving earlier than the lower energies. This time of flight
 1138 energy dispersion tends to smear out the initial sharp burst upon each subsequent
 1139 bounce. The first peak does not appear to be dispersed, and subsequent peaks show
 1140 a dispersion trend consistent across energy channels. The black vertical bars have
 1141 been added to Fig. 3.1 to highlight this energy dispersion. This dispersion signature
 1142 and amplitude decay implies that the first peak was observed soon after the electrons
 1143 were scattered, followed by decaying bounces.

1144 At this time, in magnetic coordinates, FIREBIRD-II was at McIlwain $L = 4.7$

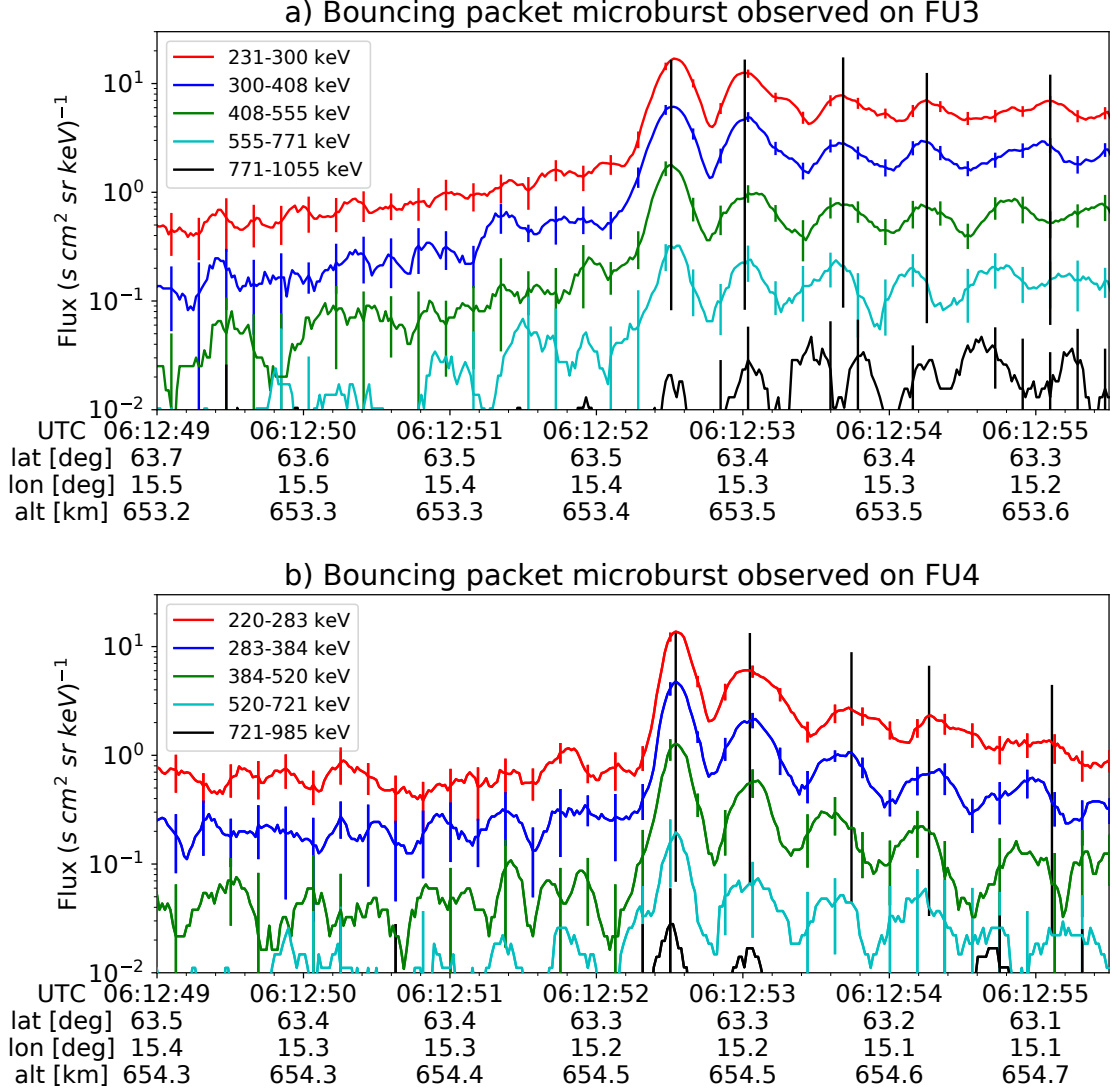


Figure 3.1: HiRes data of the microburst observed at February 2nd, 2015 at 06:12:53 UT, smoothed with a 150 ms rolling average. The subsequent bounces showed some energy dispersion. As discussed in Appendix B, a time correction of -2.28 s was applied to FU3. While the flux from five energy channels is shown, only channels with reasonable counting statistics were used for the spatial scale analysis. Vertical colored bars show the \sqrt{N} error every 10th data point and vertical black bars are lined up with the peaks in the 220-283 keV energy channel to help identify dispersion.

and MLT = 8.3, calculated with the Tsyganenko 1989 (T89) magnetic field model (Tsyganenko, 1989) using IRBEM-Lib (Boscher et al., 2012). Geographically, they were above Sweden, latitude = 63°N, longitude = 15°E, altitude = 650 km. This geographic location is magnetically conjugate to the east of the so-called South Atlantic Anomaly (SAA). The SAA is the location where the mirror points of electrons tend to occur at locations deeper in the atmosphere owing to the offset of the dipole magnetic field from the Earth's center. Electrons with pitch angles within the drift loss cone (DLC) will encounter the SAA and be removed from their eastward longitudinal drift paths (Comess et al., 2013; Dietrich et al., 2010). FU3 and FU4 are therefore both in regions where the particles in the DLC have recently precipitated, leaving only particles that were recently scattered. At the spacecraft location, locally mirroring electrons would have mirrored at 95 km in the opposite hemisphere, with more field aligned electrons mirroring at even lower altitudes. From the analysis done by Fang et al. (2010), the peak in the total ionization rate in the atmosphere for 100 keV electrons is around 80 km altitude, while the total ionization rate from 1 MeV electrons peaks around 60 km altitude. It is, therefore, expected that a fraction of the microburst electrons will survive each encounter with the atmosphere. By plotting the peak flux as a function of bounce (not shown), it was found that 40 - 60 % of the microburst electrons were lost on the first bounce, similar to the 33% loss per bounce observed for a bouncing microburst observed by SAMPEX (Thorne et al., 2005).

1165

Analysis

At the beginning of the FIREBIRD-II mission, two issues prevented the proper analysis of the microburst's spatial scale size: the spacecraft clocks were not synchronized, and their relative positions were not accurately known. We addressed these issues with a cross-correlation time lag analysis described in detail in Appendix

1170 B. From this analysis, the time correction was 2.28 ± 0.12 s (applied to Fig. 3.1) and
 1171 the separation was 19.9 ± 0.9 km at the time of the microburst observation.

1172 Electron Bounce Period

1173 We used this unique observation of bouncing electrons to calculate the bounce
 1174 period, t_b as a function of energy and compare it to the energy-dependent t_b curves
 1175 derived from four magnetic field models, the results of which are shown in Fig. 3.2.
 1176 The observed t_b and uncertainties were calculated by fitting the baseline-subtracted
 1177 HiRes flux. The baseline flux used in this analysis is given in O'Brien et al. (2004)
 1178 as the flux at the 10th percentile over a specified time interval, which in this analysis
 1179 was taken to be 0.5 seconds. The flux was fitted with a superposition of Gaussians
 1180 for each energy channel, and the uncertainty in flux was calculated using the Poisson
 1181 error from the microburst and baseline fluxes summed in quadrature. Using the fit
 1182 parameters, the mean t_b for the lowest four energy channels is shown in Fig. 3.2. The
 1183 trend of decreasing t_b as a function of energy is evident in Fig. 3.2, which further
 1184 supports the assumption that the subsequent peaks are bounces, and not a train of
 1185 microbursts scattered by bouncing chorus.

1186 The decaying peaks in the 231-408 keV electron flux observed by FU3's lowest
 1187 two energy channels (see Fig. 3.1) were right-skewed. One explanation is that there
 1188 was in-channel energy dispersion within those channels. Since t_b of higher energy
 1189 electrons is shorter, a right-skewed peak implies that higher energy electrons were
 1190 more abundant within that channel e.g. in FU3's 231-300 keV channel, the 300 keV
 1191 electrons will arrive sooner than the 231 keV electrons, but will they will be binned
 1192 in the same channel. A Gaussian fit cannot account for this in-channel dispersion,
 1193 and as a first order correction, minima between peaks was used to calculate t_b , and
 1194 is shown in Fig. 3.2. The observed energy-dependent dispersion shown in Fig. 3.2

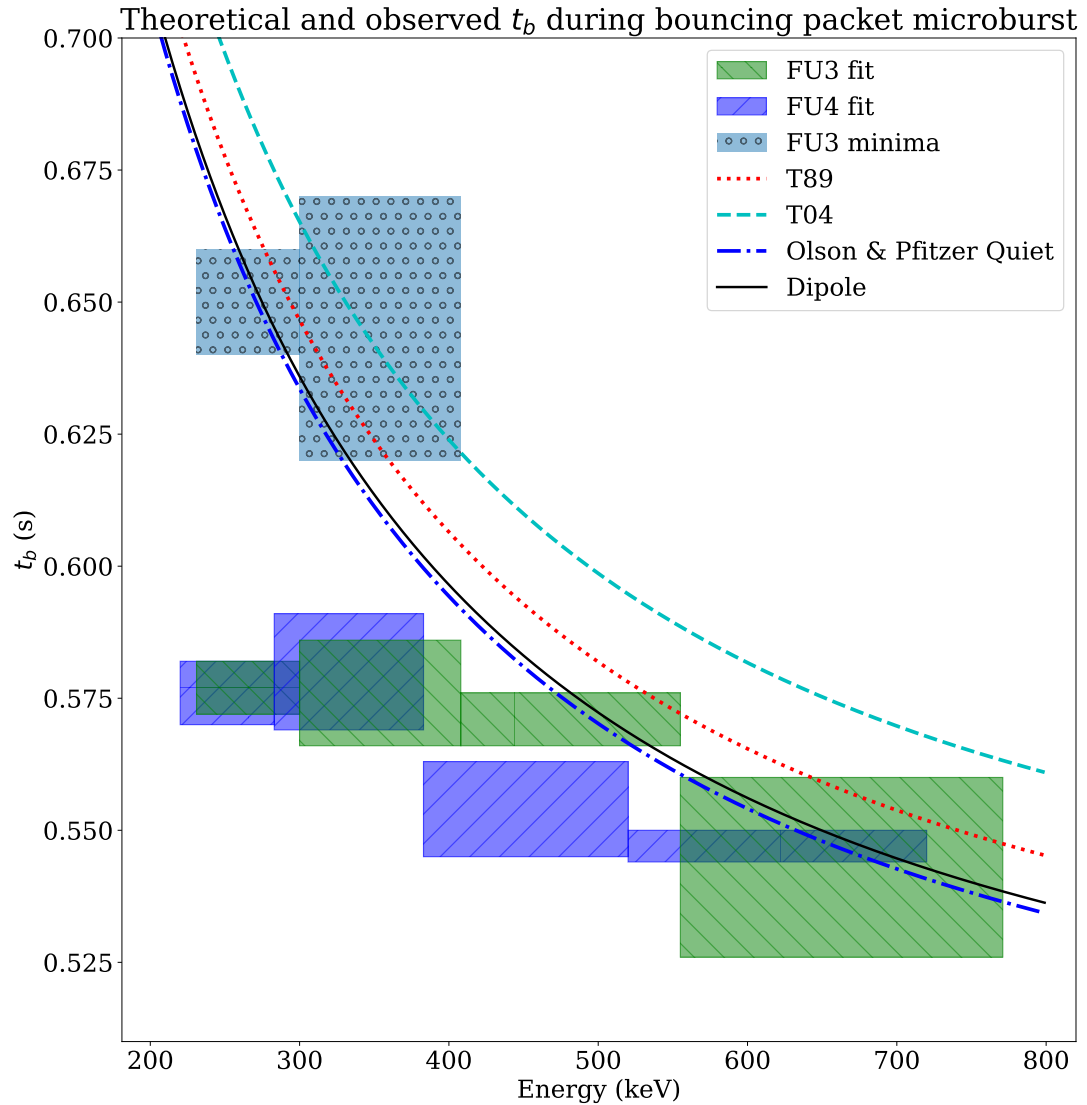


Figure 3.2: Observed and theoretical t_b for electrons of energies from 200 to 770 keV. The solid black line is t_b in a dipole magnetic field, derived in Schulz and Lanzerotti (1974). The red dotted and cyan dashed lines are the t_b derived using the T89, and T04 magnetic field models with IRBEM-Lib. Lastly, the blue dot-dash curve is the t_b derived using the Olson & Pfitzer Quiet model. The green and purple rectangles represent the observed t_b for FU3 and FU4 using a Gaussian fit, respectively. The blue rectangles represent the observed t_b calculated with the minima between the bounces. The width of the boxes represent the width of those energy channels, and the height represents the uncertainty from the fit.

is consistent with higher energy peaks returning sooner. This dispersion consistency further supports the assumption that the subsequent peaks are bounces, and not a train of microbursts scattered by bouncing chorus.

To compare the observed and modeled t_b , we superposed t_b curves for various models including an analytical solution in a dipole (Schulz and Lanzerotti, 1974), and numerical models: T89, Tsyganenko 2004 (T04) (Tsyganenko and Sitnov, 2005), and Olson & Pfitzer Quiet (Olson and Pfitzer, 1982) in Fig. 3.2. The numerical t_b curves were calculated using a wrapper for IRBEM-Lib. This code traces the magnetic field line between mirror points, and calculates t_b assuming conservation of energy and the first adiabatic invariant for electrons mirroring at FIREBIRD-II. With the empirical t_b , the models agree within FIREBIRD-II's uncertainties, but the T04 model has the largest discrepancy compared to the other models.

Microburst Energy Spectra

Next, we investigated the energy spectra of this microburst. The energy spectra was modeled with an exponential that was fit to the peak flux derived from the Gaussian fit parameters in section 3 to all but the highest energy channel. We found that the E-folding energy, $E_0 \sim 100$ keV. This spectra is similar to spectra show by Lee et al. (2005) from STSAT-1 and Datta et al. (1997) from sounding rocket measurements. The energy spectra is soft for a typical microburst observed with FIREBIRD-II and there was no statistically significant change in E_0 for subsequent bounces.

Microburst Scale Sizes

Lastly, after we applied the time and separation corrections detailed in Appendix B, we mapped the locations of FU3 and FU4 in Fig. 3.3. The locations where FU3 saw peaks 1-5 and where FU4 saw peaks 1-4 are shown as P1-5 and P1-4, respectively.

1220 The lower bound on the latitudinal extent of the microburst was the difference in
 1221 latitude between P1 on FU3 and P4 on FU4 and was found to be 29 ± 1 km. The
 1222 uncertainty was estimated from the spacecraft separation uncertainty described in
 1223 Appendix B. This scale size is the largest reported by FIREBIRD-II.

1224 In section 3, we showed that the observed decaying peaks were likely due to
 1225 bouncing, so we assume that the observed electrons in subsequent bounces were the
 1226 drifted electrons from the initial microburst. Under this assumption, the scattered
 1227 electrons observed in the last bounce by FIREBIRD-II, must have drifted east from
 1228 their initial scattering longitude, allowing us to calculate the minimum longitudinal
 1229 scale size. Following geometrical arguments, the distance that electrons drift east in
 1230 a single bounce is a product of the circumference of the drift shell foot print, and the
 1231 fraction of the total drift orbit traversed in a single bounce and is given by,

$$d_{az} = 2\pi(R_E + A) \cos(\lambda) \frac{t_b}{\langle T_d \rangle} \quad (3.1)$$

where R_E is the Earth's radius, A is the spacecraft altitude, λ is the magnetic latitude,
 t_b is the electron bounce period, and $\langle T_d \rangle$ is the electron drift period. Parks (2003)
derived $\langle T_d \rangle$ to be,

$$\langle T_d \rangle \approx \begin{cases} 43.8/(L \cdot E) & \text{if } \alpha_0 = 90^\circ \\ 62.7/(L \cdot E) & \text{if } \alpha_0 = 0^\circ \end{cases} \quad (3.2)$$

1232 where E is the electron energy in MeV, L is the L shell, and α_0 is the equatorial pitch
 1233 angle. Electrons mirroring at FIREBIRD-II have $\alpha_0 \approx 3.7^\circ$ and so the $\alpha_0 = 0^\circ$ limit
 1234 was used.

1235 The microburst's longitudinal scale size is defined as the distance the highest
 1236 energy electrons drifted in the time between the observations of the first and last
 1237 peaks. This scale size is given by $D_{az} = n d_{az}$ where n is the number of bounces

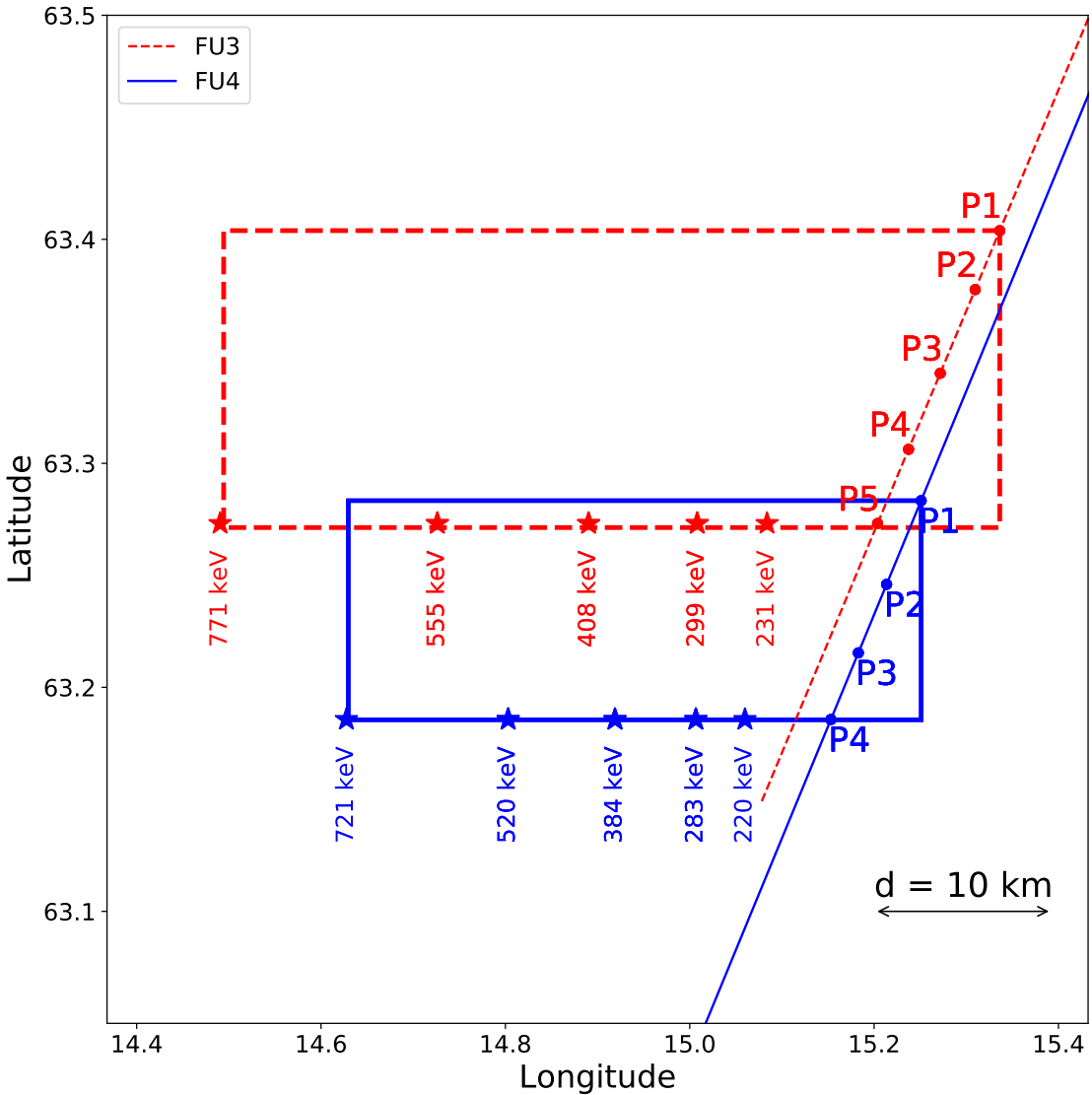


Figure 3.3: The topology of the FIREBIRD-II orbit and the multiple bounces of the microburst projected onto latitude and longitude with axis scaled to equal distance. Attributes relating to FU3 shown in red dashed lines, and FU4 with blue solid lines. The spacecraft path is shown with the diagonal lines, starting at the upper right corner. The labels P1-4 for FU4 and P1-5 for FU3 indicate where the spacecraft were when the N^{th} peak was seen in the lowest energy channel in the HiRes data. The stars with the accompanying energy labels represent the locations of the electrons with that energy that started at time of P1, and were seen at the last peak on each spacecraft. The rectangles represent the lower bound of the microburst scale size, assuming that the majority of the electrons were in the upper boundary of energy channel 4.

1238 observed. The stars in Fig. 3.3 (with labels corresponding to energy channel
 1239 boundaries) represent the locations when the microburst was observed at P1, such
 1240 that an electron of that energy would drift eastward to be seen at P5 for FU3 and P4
 1241 for FU4. Since FU3 observed more peaks it observed the larger longitudinal scale size
 1242 which is shown with the red dashed box in Fig. 3.3. FU3’s fourth energy channel’s
 1243 bounds are 555 keV and 771 keV, which correspond to longitudinal distances of 39 ± 1
 1244 km and 51 ± 1 , respectively. The uncertainty was estimated by propagating the
 1245 uncertainty in the bounce time Eq. 3.1. While the observed minimum longitudinal
 1246 scale size is dependent on FIREBIRD-II’s energy channels, the true scale size may
 1247 not be.

1248 To investigate how the microburst scale size compares to the scale sizes of chorus
 1249 waves near the magnetic equator, the microburst’s longitudinal and latitudinal scale
 1250 sizes and their uncertainties in LEO were mapped to the magnetic equator with T89.
 1251 The radial scale size (latitudinal scale mapped from LEO) was greater than 500 ± 10
 1252 km. The azimuthal scale size (longitudinal scale mapped from LEO) of 555 keV
 1253 electrons was greater than 450 ± 10 km and for the 771 keV electrons it was greater
 1254 than 530 ± 10 km. The lower bound microburst scale size is similar to the chorus
 1255 scale sizes derived by Agapitov et al. (2017, 2011), and is discussed below.

1256

Discussion and Conclusions

1257 We presented the first observation of a large microburst with multiple bounces
 1258 made possible by the twin FIREBIRD-II CubeSats. The microburst’s lower bound
 1259 LEO latitudinal and longitudinal scale sizes of 29 ± 1 km and 51 ± 1 km make
 1260 it one of the largest observed. The microburst’s LEO scale size was larger than
 1261 the latitudinal scale sizes of typical > 1 MeV microbursts reported in Blake et al.
 1262 (1996), approximately 10 times larger than reported in Dietrich et al. (2010), and

1263 approximately 2.6 times larger than other simultaneous microbursts observed by
 1264 FIREBIRD-II (Crew et al., 2016). Lastly, the scale sizes derived here were similar to
 1265 the scale sizes of \sim 15 keV microbursts observed with a high altitude balloon (Parks,
 1266 1967). No energy dependence on the minimum latitudinal scale size was observed,
 1267 while the observed energy dependence of the minimum longitudinal scale size is an
 1268 artifact of the technique we used to estimate their drift motion.

1269 The microburst scale size obtained in Section 3 and scaled to the geomagnetic
 1270 equator can be compared with the scales of chorus waves presumably responsible for
 1271 the rapid burst electron precipitation. Early direct estimates of the chorus source
 1272 scales were made by the coordinated measurement by ISEE-1, 2. The wave power
 1273 correlation scale was estimated to be about several hundred kilometers across the
 1274 background magnetic field (Gurnett et al., 1979). Furthermore, Santolik et al. (2003)
 1275 determined the correlation lengths of chorus-type whistler waves to be around 100
 1276 km based on multipoint CLUSTER Wide Band Data measurements near the chorus
 1277 source region at $L \approx 4$, during the magnetic storm of 18 April 2002. Agapitov et al.
 1278 (2017, 2011, 2010) recently showed that the spatial extent of chorus source region can
 1279 be larger, ranging from 600 km in the outer radiation belt to more than 1000 km in
 1280 the outer magnetosphere. The lower bound azimuthal and latitudinal scales obtained
 1281 in Section 3 and scaled to the magnetic equator, are similar to the whistler-mode
 1282 chorus source scale sizes reported in Agapitov et al. (2017, 2011).

1283 No wave measurements from nearby spacecraft were available at this time.
 1284 Nevertheless, during the hours before and after this observation, the Van Allen Probes'
 1285 (Mauk et al., 2013) Electric and Magnetic Field Instrument and Integrated Science
 1286 (Kletzing et al., 2013) observed strong wave power in the lower band chorus frequency
 1287 range, inside the outer radiation belt between 22 and 2 MLT. Furthermore, AE ~ 400
 1288 nT at this time, and relatively strong chorus waves were statistically more likely to

1289 be present at FIREBIRD-II's MLT (Li et al., 2009b).

1290 The empirically estimated and modeled t_b in this study agree within FIREBIRD-
 1291 II's uncertainties, confirming that the energy-dependent dispersion was due to
 1292 bouncing. The t_b curves are a proxy for field line length, and this agreement implies
 1293 that they are comparable. This is expected since the magnetosphere is not drastically
 1294 compressed at 8 MLT, but we expect a larger discrepancy near midnight, where the
 1295 magnetosphere is more stretched and difficult to accurately model. In future studies,
 1296 this analysis can be used as a diagnostic tool to validate field line lengths, and improve
 1297 magnetic field models.

1298 The similarity of the microburst and chorus source region scale sizes, as well
 1299 as magnetospheric location and conditions, further support the causal relationship
 1300 between microbursts and chorus.

1301

Acknowledgments

1302 This work was made possible with help from the FIREBIRD team, and the
 1303 members of the Space Sciences and Engineering Laboratory at Montana State
 1304 University for their hard work to make this mission a success. In addition, M.
 1305 Shumko acknowledges Drew Turner for his suggestions regarding the bounce period
 1306 calculations, and Dana Longcope for his proofreading feedback. The FIREBIRD-II
 1307 data are available at http://solar.physics.montana.edu/FIREBIRD_II/. This analysis
 1308 is supported by the National Science Foundation under Grant Numbers 0838034 and
 1309 1339414. Furthermore, the work of O. Agapitov was supported by the NASA grant
 1310 NNX16AF85G.

1311

CHAPTER FOUR

1312

MICROBURST SIZE DISTRIBUTION DERIVED WITH AEROCUBE-6

1313

Contribution of Authors and Co-Authors

1314 Manuscript(s) in Chapter(s) 1

1315

1316 Author: [type author name here]

1317 Contributions: [list contributions here, single-spaced]

1318 Co-Author: [type co-author name here]

1319 Contributions: [list contributions here, single-spaced]

1320 Co-Author: [type co-author name here]

1321 Contributions: [list contributions here, single-spaced]

1322

1323

Manuscript Information

1324 [Type Author and Co-author(s) Names Here]

1325 Journal of Geophysical Research

1326 Status of Manuscript: **Officially submitted to a peer-reviewed journal**

1327 Wiley

1328

1329

CONCLUSIONS AND FUTURE WORK

1330

- 1331 1. Microburst scattering mechanism and relation to prior work
- 1332 2. Microburst sizes and the elliptical shape, mention the curtain-microburst
1333 ambiguity.
- 1334 3. In future work mention how curtains should be studied and outline that project.
1335 Mention the SAA and amplitude idea.
- 1336 4. Mention REAL and how it plans to look at the microburst flux in PA space.
- 1337 5. Mention BOOMS and how it plans to image microbursts to determine their
1338 shape without ambiguity.

1339

In this dissertation we have explored the microburst scattering mechanism directly in Chapter 2 and indirectly in Chapters 3 and 4. In Chapter 2 we used numerous particle and wave instruments on the Van Allen Probes and found signatures of microbursts with the Magnetic Electron Ion Spectrometer. To these observations we applied the relativistic theory of wave-particle resonant diffusion and found that the motion of the microburst electrons was not along single-wave particle characteristics in momentum phase space, given the spacecraft position and orientation and most probable wave and plasma parameters.

1347

(Shumko et al., 2018)

1348

With these results, it is always important to keep our methods and their biases in mind. Werner Heisenberg once said that “What we observe is not nature itself, 1349 but nature exposed to our method of questioning.”

Future Work

- 1353 Abel, B. and Thorne, R. M. (1998). Electron scattering loss in earth's inner
 1354 magnetosphere: 1. dominant physical processes. *Journal of Geophysical Research: Space Physics*, 103(A2):2385–2396.
- 1356 Agapitov, O., Blum, L. W., Mozer, F. S., Bonnell, J. W., and Wygant, J. (2017).
 1357 Chorus whistler wave source scales as determined from multipoint van allen probe
 1358 measurements. *Geophysical Research Letters*, pages n/a–n/a. 2017GL072701.
- 1359 Agapitov, O., Krasnoselskikh, V., Dudok de Wit, T., Khotyaintsev, Y., Pickett,
 1360 J. S., Santolik, O., and Rolland, G. (2011). Multispacecraft observations of chorus
 1361 emissions as a tool for the plasma density fluctuations' remote sensing. *Journal of Geophysical Research: Space Physics*, 116(A9):n/a–n/a. A09222.
- 1363 Agapitov, O., Krasnoselskikh, V., Zaliznyak, Y., Angelopoulos, V., Le Contel, O.,
 1364 and Rolland, G. (2010). Chorus source region localization in the earth's outer
 1365 magnetosphere using themis measurements. *Annales Geophysicae*, 28(6):1377–
 1366 1386.
- 1367 Anderson, B., Shekhar, S., Millan, R., Crew, A., Spence, H., Klumpar, D., Blake, J.,
 1368 O'Brien, T., and Turner, D. (2017). Spatial scale and duration of one microburst
 1369 region on 13 August 2015. *Journal of Geophysical Research: Space Physics*.
- 1370 Anderson, K. A. and Milton, D. W. (1964). Balloon observations of X rays in the
 1371 auroral zone: 3. High time resolution studies. *Journal of Geophysical Research*,
 1372 69(21):4457–4479.
- 1373 Barcus, J., Brown, R., and Rosenberg, T. (1966). Spatial and temporal character of
 1374 fast variations in auroral-zone x rays. *Journal of Geophysical Research*, 71(1):125–
 1375 141.
- 1376 Baumjohann, W. and Treumann, R. A. (1997). *Basic space plasma physics*. World
 1377 Scientific.
- 1378 Blake, J., Carranza, P., Claudepierre, S., Clemons, J., Crain, W., Dotan, Y.,
 1379 Fennell, J., Fuentes, F., Galvan, R., George, J., et al. (2013). The magnetic electron
 1380 ion spectrometer (MagEIS) instruments aboard the radiation belt storm probes
 1381 (RBSP) spacecraft. *Space Science Reviews*, 179(1-4):383–421.
- 1382 Blake, J.,Looper, M., Baker, D., Nakamura, R., Klecker, B., and Hovestadt, D.
 1383 (1996). New high temporal and spatial resolution measurements by sampex of the
 1384 precipitation of relativistic electrons. *Advances in Space Research*, 18(8):171 – 186.
- 1385 Blake, J. B. and O'Brien, T. P. (2016). Observations of small-scale latitudinal
 1386 structure in energetic electron precipitation. *Journal of Geophysical Research: Space Physics*, 121(4):3031–3035. 2015JA021815.

- 1388 Blum, L., Li, X., and Denton, M. (2015). Rapid MeV electron precipitation as
 1389 observed by SAMPEX/HILT during high-speed stream-driven storms. *Journal of*
 1390 *Geophysical Research: Space Physics*, 120(5):3783–3794. 2014JA020633.
- 1391 Bortnik, J., Thorne, R., and Inan, U. S. (2008). Nonlinear interaction of energetic
 1392 electrons with large amplitude chorus. *Geophysical Research Letters*, 35(21).
- 1393 Boscher, D., Bourdarie, S., O'Brien, P., Guild, T., and Shumko, M. (2012). Irbem-lib
 1394 library.
- 1395 Breneman, A., Crew, A., Sample, J., Klumpar, D., Johnson, A., Agapitov, O.,
 1396 Shumko, M., Turner, D., Santolik, O., Wygant, J., et al. (2017). Observations
 1397 directly linking relativistic electron microbursts to whistler mode chorus: Van allen
 1398 probes and FIREBIRD II. *Geophysical Research Letters*.
- 1399 Breneman, A. W., Halford, A., Millan, R., McCarthy, M., Fennell, J., Sample, J.,
 1400 Woodger, L., Hospodarsky, G., Wygant, J. R., Cattell, C. A., et al. (2015). Global-
 1401 scale coherence modulation of radiation-belt electron loss from plasmaspheric hiss.
 1402 *Nature*, 523(7559):193.
- 1403 Brown, R., Barcus, J., and Parsons, N. (1965). Balloon observations of auroral zone
 1404 x rays in conjugate regions. 2. microbursts and pulsations. *Journal of Geophysical*
 1405 *Research (U.S.)*.
- 1406 Capannolo, L., Li, W., Ma, Q., Shen, X.-C., Zhang, X.-J., Redmon, R., Rodriguez,
 1407 J., Engebretson, M., Kletzing, C., Kurth, W., et al. (2019). Energetic electron
 1408 precipitation: multi-event analysis of its spatial extent during emic wave activity.
 1409 *Journal of Geophysical Research: Space Physics*.
- 1410 Claudepierre, S., O'Brien, T.,Looper, M., Blake, J., Fennell, J., Roeder, J.,
 1411 Clemons, J., Mazur, J., Turner, D., Reeves, G., et al. (2019). A revised look
 1412 at relativistic electrons in the earth's inner radiation zone and slot region. *Journal*
 1413 *of Geophysical Research: Space Physics*, 124(2):934–951.
- 1414 Comess, M., Smith, D., Selesnick, R., Millan, R., and Sample, J. (2013). Duskside
 1415 relativistic electron precipitation as measured by sampex: A statistical survey.
 1416 *Journal of Geophysical Research: Space Physics*, 118(8):5050–5058.
- 1417 Crew, A. B., Spence, H. E., Blake, J. B., Klumpar, D. M., Larsen, B. A., O'Brien,
 1418 T. P., Driscoll, S., Handley, M., Legere, J., Longworth, S., Mashburn, K.,
 1419 Mosleh, E., Ryhajlo, N., Smith, S., Springer, L., and Widholm, M. (2016). First
 1420 multipoint in situ observations of electron microbursts: Initial results from the
 1421 NSF FIREBIRD II mission. *Journal of Geophysical Research: Space Physics*,
 1422 121(6):5272–5283. 2016JA022485.

- 1423 Datta, S., Skoug, R., McCarthy, M., and Parks, G. (1997). Modeling of microburst
 1424 electron precipitation using pitch angle diffusion theory. *Journal of Geophysical*
 1425 *Research: Space Physics*, 102(A8):17325–17333.
- 1426 Dietrich, S., Rodger, C. J., Clilverd, M. A., Bortnik, J., and Raita, T. (2010).
 1427 Relativistic microburst storm characteristics: Combined satellite and ground-based
 1428 observations. *Journal of Geophysical Research: Space Physics*, 115(A12).
- 1429 Douma, E., Rodger, C. J., Blum, L. W., and Clilverd, M. A. (2017). Occurrence
 1430 characteristics of relativistic electron microbursts from SAMPEX observations.
 1431 *Journal of Geophysical Research: Space Physics*, 122(8):8096–8107. 2017JA024067.
- 1432 Dungey, J. W. (1961). Interplanetary magnetic field and the auroral zones. *Phys.*
 1433 *Rev. Lett.*, 6:47–48.
- 1434 Fang, X., Randall, C. E., Lummerzheim, D., Wang, W., Lu, G., Solomon, S. C., and
 1435 Frahm, R. A. (2010). Parameterization of monoenergetic electron impact ionization.
 1436 *Geophysical Research Letters*, 37(22).
- 1437 Funsten, H., Skoug, R., Guthrie, A., MacDonald, E., Baldonado, J., Harper, R.,
 1438 Henderson, K., Kihara, K., Lake, J., Larsen, B., et al. (2013). Helium, Oxygen,
 1439 Proton, and Electron (HOPE) mass spectrometer for the radiation belt storm
 1440 probes mission. *Space Science Reviews*, 179(1-4):423–484.
- 1441 Greeley, A., Kanekal, S., Baker, D., Klecker, B., and Schiller, Q. (2019). Quantifying
 1442 the contribution of microbursts to global electron loss in the radiation belts. *Journal*
 1443 *of Geophysical Research: Space Physics*.
- 1444 Gurnett, D., Anderson, R., Scarf, F., Fredricks, R., and Smith, E. (1979). Initial
 1445 results from the isee-1 and-2 plasma wave investigation. *Space Science Reviews*,
 1446 23(1):103–122.
- 1447 Hendry, A. T., Rodger, C. J., and Clilverd, M. A. (2017). Evidence of sub-mev
 1448 emic-driven electron precipitation. *Geophysical Research Letters*, 44(3):1210–1218.
- 1449 Hoots, F. R. and Roehrich, R. L. (1980). Models for propagation of norad element
 1450 sets. Technical Report 3, Spacetrack.
- 1451 Horne, R., Glauert, S., Meredith, N., Boscher, D., Maget, V., Heynderickx, D., and
 1452 Pitchford, D. (2013). Space weather impacts on satellites and forecasting the earth’s
 1453 electron radiation belts with spacecast. *Space Weather*, 11(4):169–186.
- 1454 Horne, R., Thorne, R., Meredith, N., and Anderson, R. (2003). Diffuse auroral
 1455 electron scattering by electron cyclotron harmonic and whistler mode waves during
 1456 an isolated substorm. *Journal of Geophysical Research: Space Physics*, 108(A7).

- 1457 Horne, R. B. and Thorne, R. M. (2003). Relativistic electron acceleration and
 1458 precipitation during resonant interactions with whistler-mode chorus. *Geophysical*
 1459 *Research Letters*, 30(10). 1527.
- 1460 Horne, R. B., Thorne, R. M., Shprits, Y. Y., Meredith, N. P., Glauert, S. A., Smith,
 1461 A. J., Kanekal, S. G., Baker, D. N., Engebretson, M. J., Posch, J. L., et al.
 1462 (2005). Wave acceleration of electrons in the van allen radiation belts. *Nature*,
 1463 437(7056):227.
- 1464 Kasahara, S., Miyoshi, Y., Yokota, S., Mitani, T., Kasahara, Y., Matsuda, S.,
 1465 Kumamoto, A., Matsuoka, A., Kazama, Y., Frey, H., et al. (2018). Pulsating
 1466 aurora from electron scattering by chorus waves. *Nature*, 554(7692):337.
- 1467 Kletzing, C., Kurth, W., Acuna, M., MacDowall, R., Torbert, R., Averkamp, T.,
 1468 Bodet, D., Bounds, S., Chutter, M., Connerney, J., et al. (2013). The electric and
 1469 magnetic field instrument suite and integrated science (EMFISIS) on RBSP. *Space*
 1470 *Science Reviews*, 179(1-4):127–181.
- 1471 Klumpar, D., Springer, L., Mosleh, E., Mashburn, K., Berardinelli, S., Gunderson,
 1472 A., Handly, M., Ryhajlo, N., Spence, H., Smith, S., Legere, J., Widholm, M.,
 1473 Longworth, S., Crew, A., Larsen, B., Blake, J., and Walmsley, N. (2015). Flight
 1474 system technologies enabling the twin-cubesat firebird-ii scientific mission.
- 1475 Lee, J. J., Parks, G. K., Lee, E., Tsurutani, B. T., Hwang, J., Cho, K. S., Kim, K.-H.,
 1476 Park, Y. D., Min, K. W., and McCarthy, M. P. (2012). Anisotropic pitch angle
 1477 distribution of 100 keV microburst electrons in the loss cone: measurements from
 1478 STSAT-1. *Annales Geophysicae*, 30(11):1567–1573.
- 1479 Lee, J.-J., Parks, G. K., Min, K. W., Kim, H. J., Park, J., Hwang, J., McCarthy,
 1480 M. P., Lee, E., Ryu, K. S., Lim, J. T., Sim, E. S., Lee, H. W., Kang, K. I., and
 1481 Park, H. Y. (2005). Energy spectra of 170–360 keV electron microbursts measured
 1482 by the korean STSAT-1. *Geophysical Research Letters*, 32(13). L13106.
- 1483 Li, W., Thorne, R., Angelopoulos, V., Bonnell, J., McFadden, J., Carlson, C.,
 1484 LeContel, O., Roux, A., Glassmeier, K., and Auster, H. (2009a). Evaluation of
 1485 whistler-mode chorus intensification on the nightside during an injection event
 1486 observed on the THEMIS spacecraft. *Journal of Geophysical Research: Space*
 1487 *Physics*, 114(A1).
- 1488 Li, W., Thorne, R., Bortnik, J., Tao, X., and Angelopoulos, V. (2012). Characteristics
 1489 of hiss-like and discrete whistler-mode emissions. *Geophysical Research Letters*,
 1490 39(18).
- 1491 Li, W., Thorne, R. M., Angelopoulos, V., Bortnik, J., Cully, C. M., Ni, B., LeContel,
 1492 O., Roux, A., Auster, U., and Magnes, W. (2009b). Global distribution of whistler-
 1493 mode chorus waves observed on the THEMIS spacecraft. *Geophysical Research*
 1494 *Letters*, 36(9). L09104.

- 1495 Li, X., Selesnick, R., Schiller, Q., Zhang, K., Zhao, H., Baker, D. N., and Temerin,
 1496 M. A. (2017). Measurement of electrons from albedo neutron decay and neutron
 1497 density in near-earth space. *Nature*, 552(7685):382.
- 1498 Lorentzen, K. R., Blake, J. B., Inan, U. S., and Bortnik, J. (2001a). Observations
 1499 of relativistic electron microbursts in association with VLF chorus. *Journal of*
 1500 *Geophysical Research: Space Physics*, 106(A4):6017–6027.
- 1501 Lorentzen, K. R.,Looper, M. D., and Blake, J. B. (2001b). Relativistic electron
 1502 microbursts during the GEM storms. *Geophysical Research Letters*, 28(13):2573–
 1503 2576.
- 1504 Lyons, L. R. and Thorne, R. M. (1973). Equilibrium structure of radiation belt
 1505 electrons. *Journal of Geophysical Research*, 78(13):2142–2149.
- 1506 Manweiler, J. W. and Zwiener, H. M. (2018). Science Operations Center (SOC)
 1507 RBSPICE Science Data Handbook Revision: e. Technical report, Fundamental
 1508 Technologies, LLC.
- 1509 Mauk, B., Fox, N. J., Kanekal, S., Kessel, R., Sibeck, D., and Ukhorskiy, A. (2013).
 1510 Science objectives and rationale for the radiation belt storm probes mission. *Space*
 1511 *Science Reviews*, 179(1-4):3–27.
- 1512 Meredith, N., Horne, R., Summers, D., Thorne, R., Iles, R., Heynderickx, D., and
 1513 Anderson, R. (2002). Evidence for acceleration of outer zone electrons to relativistic
 1514 energies by whistler mode chorus. In *Annales Geophysicae*, volume 20, pages 967–
 1515 979.
- 1516 Millan, R. and Thorne, R. (2007). Review of radiation belt relativistic electron losses.
 1517 *Journal of Atmospheric and Solar-Terrestrial Physics*, 69(3):362 – 377.
- 1518 Millan, R. M., Lin, R., Smith, D., Lorentzen, K., and McCarthy, M. (2002). X-
 1519 ray observations of mev electron precipitation with a balloon-borne germanium
 1520 spectrometer. *Geophysical research letters*, 29(24).
- 1521 Mitchell, D., Lanzerotti, L., Kim, C., Stokes, M., Ho, G., Cooper, S., Ukhorskiy, A.,
 1522 Manweiler, J., Jaskulek, S., Haggerty, D., et al. (2013). Radiation belt storm probes
 1523 ion composition experiment (RBSPICE). *Space Science Reviews*, 179(1-4):263–308.
- 1524 Mozer, F. S., Agapitov, O. V., Blake, J. B., and Vasko, I. Y. (2018). Simultaneous
 1525 observations of lower band chorus emissions at the equator and microburst
 1526 precipitating electrons in the ionosphere. *Geophysical Research Letters*.
- 1527 Nakamura, R., Baker, D. N., Blake, J. B., Kanekal, S., Klecker, B., and Hovestadt,
 1528 D. (1995). Relativistic electron precipitation enhancements near the outer edge of
 1529 the radiation belt. *Geophysical Research Letters*, 22(9):1129–1132.

- 1530 Nakamura, R., Isowa, M., Kamide, Y., Baker, D., Blake, J., and Looper, M. (2000).
 1531 Observations of relativistic electron microbursts in association with VLF chorus.
 1532 *J. Geophys. Res.*, 105:15875–15885.
- 1533 Nishimura, Y., Bortnik, J., Li, W., Thorne, R., Chen, L., Lyons, L., Angelopoulos, V., Mende, S., Bonnell, J., Le Contel, O., et al. (2011). Multievent study of the
 1534 correlation between pulsating aurora and whistler mode chorus emissions. *Journal of Geophysical Research: Space Physics*, 116(A11).
- 1535
- 1536
- 1537 O'Brien, T., Claudepierre, S., Blake, J., Fennell, J. F., Clemons, J., Roeder, J.,
 1538 Spence, H. E., Reeves, G., and Baker, D. (2014). An empirically observed pitch-
 1539 angle diffusion eigenmode in the earth's electron belt near $\lambda^* = 5.0$. *Geophysical Research Letters*, 41(2):251–258.
- 1540
- 1541 O'Brien, T., Claudepierre, S., Guild, T., Fennell, J., Turner, D., Blake, J., Clemons,
 1542 J., and Roeder, J. (2016). Inner zone and slot electron radial diffusion revisited.
 1543 *Geophysical Research Letters*, 43(14):7301–7310.
- 1544
- 1545 O'Brien, T. and Moldwin, M. (2003). Empirical plasmapause models from magnetic indices. *Geophysical Research Letters*, 30(4).
- 1546
- 1547 O'Brien, T. P., Looper, M. D., and Blake, J. B. (2004). Quantification of relativistic
 1548 electron microburst losses during the GEM storms. *Geophysical Research Letters*,
 31(4). L04802.
- 1549
- 1550 O'Brien, T. P., Lorentzen, K. R., Mann, I. R., Meredith, N. P., Blake, J. B., Fennell,
 1551 J. F., Looper, M. D., Milling, D. K., and Anderson, R. R. (2003). Energization of
 1552 relativistic electrons in the presence of ULF power and MeV microbursts: Evidence
 1553 for dual ULF and VLF acceleration. *Journal of Geophysical Research: Space Physics*, 108(A8).
- 1554
- 1555 Olson, W. P. and Pfitzer, K. A. (1982). A dynamic model of the magnetospheric
 1556 magnetic and electric fields for july 29, 1977. *Journal of Geophysical Research: Space Physics*, 87(A8):5943–5948.
- 1557
- 1558 Ozaki, M., Miyoshi, Y., Shiokawa, K., Hosokawa, K., Oyama, S.-i., Kataoka, R.,
 1559 Ebihara, Y., Ogawa, Y., Kasahara, Y., Yagitani, S., et al. (2019). Visualization of
 1560 rapid electron precipitation via chorus element wave-particle interactions. *Nature communications*, 10(1):257.
- 1561
- 1562 Ozaki, M., Yagitani, S., Ishizaka, K., Shiokawa, K., Miyoshi, Y., Kadokura, A.,
 1563 Yamagishi, H., Kataoka, R., Ieda, A., Ebihara, Y., Sato, N., and Nagano, I. (2012).
 1564 Observed correlation between pulsating aurora and chorus waves at Syowa Station
 1565 in Antarctica: A case study. *Journal of Geophysical Research: Space Physics*, 117(A8).

- 1566 Parks, G. (2003). *Physics Of Space Plasmas: An Introduction, Second Edition.*
 1567 Westview Press.
- 1568 Parks, G. K. (1967). Spatial characteristics of auroral-zone X-ray microbursts. *Journal
 1569 of Geophysical Research*, 72(1):215–226.
- 1570 Reeves, G., Spence, H. E., Henderson, M., Morley, S., Friedel, R., Funsten, H., Baker,
 1571 D., Kanekal, S., Blake, J., Fennell, J., et al. (2013). Electron acceleration in the
 1572 heart of the van allen radiation belts. *Science*, 341(6149):991–994.
- 1573 Reeves, G. D., McAdams, K. L., Friedel, R. H. W., and O'Brien, T. P. (2003). Ac-
 1574 celeration and loss of relativistic electrons during geomagnetic storms. *Geophysical
 1575 Research Letters*, 30(10):n/a–n/a. 1529.
- 1576 Santolik, O., Gurnett, D., Pickett, J., Parrot, M., and Cornilleau-Wehrlin, N. (2003).
 1577 Spatio-temporal structure of storm-time chorus. *Journal of Geophysical Research:
 1578 Space Physics*, 108(A7).
- 1579 Santolk, O., Parrot, M., and Lefevre, F. (2003). Singular value decomposition
 1580 methods for wave propagation analysis. *Radio Science*, 38(1):n/a–n/a. 1010.
- 1581 Schulz, M. and Lanzerotti, L. J. (1974). *Particle Diffusion in the Radiation Belts.*
 1582 Springer.
- 1583 Selesnick, R. S., Blake, J. B., and Mewaldt, R. A. (2003). Atmospheric losses of
 1584 radiation belt electrons. *Journal of Geophysical Research: Space Physics*, 108(A12).
 1585 1468.
- 1586 Shprits, Y. Y., Meredith, N. P., and Thorne, R. M. (2007). Parameterization
 1587 of radiation belt electron loss timescales due to interactions with chorus waves.
 1588 *Geophysical Research Letters*, 34(11):n/a–n/a. L11110.
- 1589 Shprits, Y. Y. and Thorne, R. M. (2004). Time dependent radial diffusion modeling
 1590 of relativistic electrons with realistic loss rates. *Geophysical Research Letters*,
 1591 31(8):n/a–n/a. L08805.
- 1592 Shumko, M., Sample, J., Johnson, A., Blake, B., Crew, A., Spence, H., Klumpar, D.,
 1593 Agapitov, O., and Handley, M. (2018). Microburst scale size derived from multiple
 1594 bounces of a microburst simultaneously observed with the firebird-ii cubesats.
 1595 *Geophysical Research Letters*, 45(17):8811–8818.
- 1596 Spence, H. E., Blake, J. B., Crew, A. B., Driscoll, S., Klumpar, D. M., Larsen,
 1597 B. A., Legere, J., Longworth, S., Mosleh, E., O'Brien, T. P., Smith, S., Springer,
 1598 L., and Widholm, M. (2012). Focusing on size and energy dependence of electron
 1599 microbursts from the van allen radiation belts. *Space Weather*, 10(11).

- 1600 Summers, D., Thorne, R. M., and Xiao, F. (1998). Relativistic theory of wave-particle
 1601 resonant diffusion with application to electron acceleration in the magnetosphere.
 1602 *Journal of Geophysical Research: Space Physics*, 103(A9):20487–20500.
- 1603 Takahashi, K. and Denton, R. E. (2007). Magnetospheric seismology using multi-
 1604 harmonic toroidal waves observed at geosynchronous orbit. *Journal of Geophysical
 1605 Research: Space Physics*, 112(A5).
- 1606 Thorne, R. M. (2010). Radiation belt dynamics: The importance of wave-particle
 1607 interactions. *Geophysical Research Letters*, 37(22). L22107.
- 1608 Thorne, R. M. and Andreoli, L. J. (1981). *Mechanisms for Intense Relativistic
 1609 Electron Precipitation*, pages 381–394. Springer Netherlands, Dordrecht.
- 1610 Thorne, R. M., O'Brien, T. P., Shprits, Y. Y., Summers, D., and Horne, R. B. (2005).
 1611 Timescale for MeV electron microburst loss during geomagnetic storms. *Journal
 1612 of Geophysical Research: Space Physics*, 110(A9). A09202.
- 1613 Trefall, H., Bjordal, J., Ullaland, S., and Stadsnes, J. (1966). On the extension of
 1614 auroral-zone x-ray microbursts. *Journal of Atmospheric and Terrestrial Physics*,
 1615 28(2):225–233.
- 1616 Tsurutani, B. T. and Lakhina, G. S. (1997). Some basic concepts of wave-particle
 1617 interactions in collisionless plasmas. *Reviews of Geophysics*, 35(4):491–501.
- 1618 Tsyganenko, N. (1989). A solution of the chapman-ferraro problem for an ellipsoidal
 1619 magnetopause. *Planetary and Space Science*, 37(9):1037 – 1046.
- 1620 Tsyganenko, N. A. and Sitnov, M. I. (2005). Modeling the dynamics of the inner
 1621 magnetosphere during strong geomagnetic storms. *Journal of Geophysical Research:
 1622 Space Physics*, 110(A3).
- 1623 Turner, D., Claudepierre, S., Fennell, J., O'Brien, T., Blake, J., Lemon, C.,
 1624 Gkioulidou, M., Takahashi, K., Reeves, G., Thaller, S., et al. (2015). Energetic
 1625 electron injections deep into the inner magnetosphere associated with substorm
 1626 activity. *Geophysical Research Letters*, 42(7):2079–2087.
- 1627 Ukhorskiy, A. Y., Anderson, B. J., Brandt, P. C., and Tsyganenko, N. A. (2006).
 1628 Storm time evolution of the outer radiation belt: Transport and losses. *Journal of
 1629 Geophysical Research: Space Physics*, 111(A11):n/a–n/a. A11S03.
- 1630 Van Allen, J. A. (1959). The geomagnetically trapped corpuscular radiation. *Journal
 1631 of Geophysical Research*, 64(11):1683–1689.
- 1632 Vernov, S. and Chudakov, A. (1960). Investigation of radiation in outer space. In
 1633 *International Cosmic Ray Conference*, volume 3, page 19.

- 1634 Walker, A. D. M. (1993). *Plasma waves in the magnetosphere*, volume 24. Springer
1635 Science & Business Media.
- 1636 Woodger, L., Halford, A., Millan, R., McCarthy, M., Smith, D., Bowers, G., Sample,
1637 J., Anderson, B., and Liang, X. (2015). A summary of the BARREL campaigns:
1638 Technique for studying electron precipitation. *Journal of Geophysical Research: Space Physics*, 120(6):4922–4935.
1639

APPENDIX: APPENDIX A

1641 This appendix contains Figs. A.1 and A.2. Figure A.1 shows evidence that
1642 supports our claim that the “hiss-like” chorus wave observed at 11:17:03 UT with
1643 EMFISIS WFR instrument on RBSP-A was parallel propagating. The polar angle
1644 of the wave vector and the supporting planarity of the magnetic field polarization
1645 shown in Fig. A.1 was calculated using the singular value decomposition (SVD)
1646 method (Santolk et al., 2003).

1647 Figure A.2 supports the claim that RBSPICE-A observed a 10-80% increase in
1648 the count rates at the microburst times and pitch angles. Figure A.2 shows the ratio
1649 of the RBSPICE-A’s EBR count rates during the four microbursts to the quiet time
1650 one spin before, at the same pitch angles.

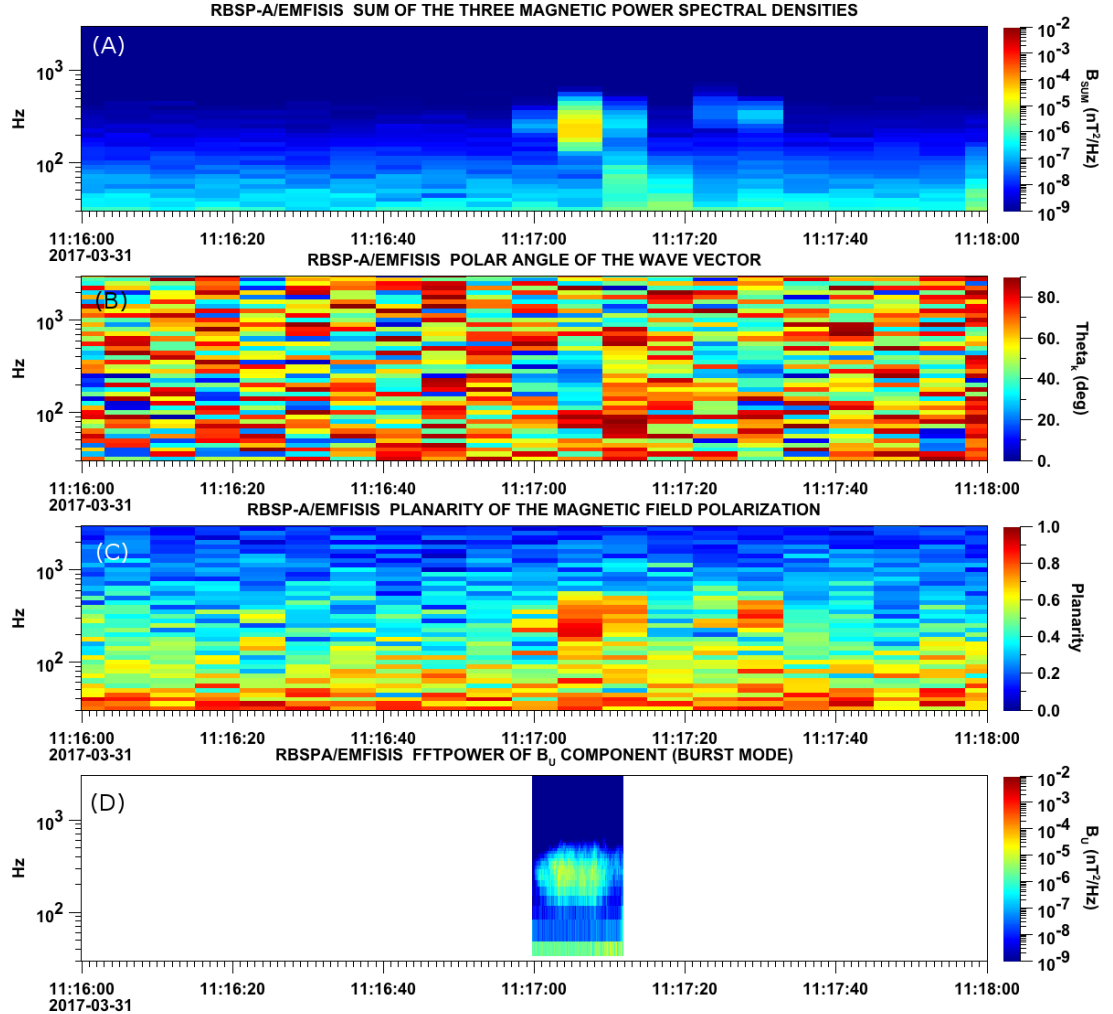


Figure A.1: Panel (A) shows the magnetic power spectral density as a function of frequency and time from the EMFISIS WFR instrument on board RBSP-A. The “hiss-like” wave used for the resonant diffusion analysis was observed starting at 11:17:03 UT. In the same format as panel (A), panel (B) shows the polar angle of the wave vector for this time period. The wave of interest had a normal wave vector, $\theta_k < 30^\circ$. Since the results in panel (B) are valid only for high planarity, panel (C) shows planarity in the same format as panels (A) and (B). The wave of interest was found to have a planarity of > 0.8 . Lastly, panel (D) shows the available burst mode data.

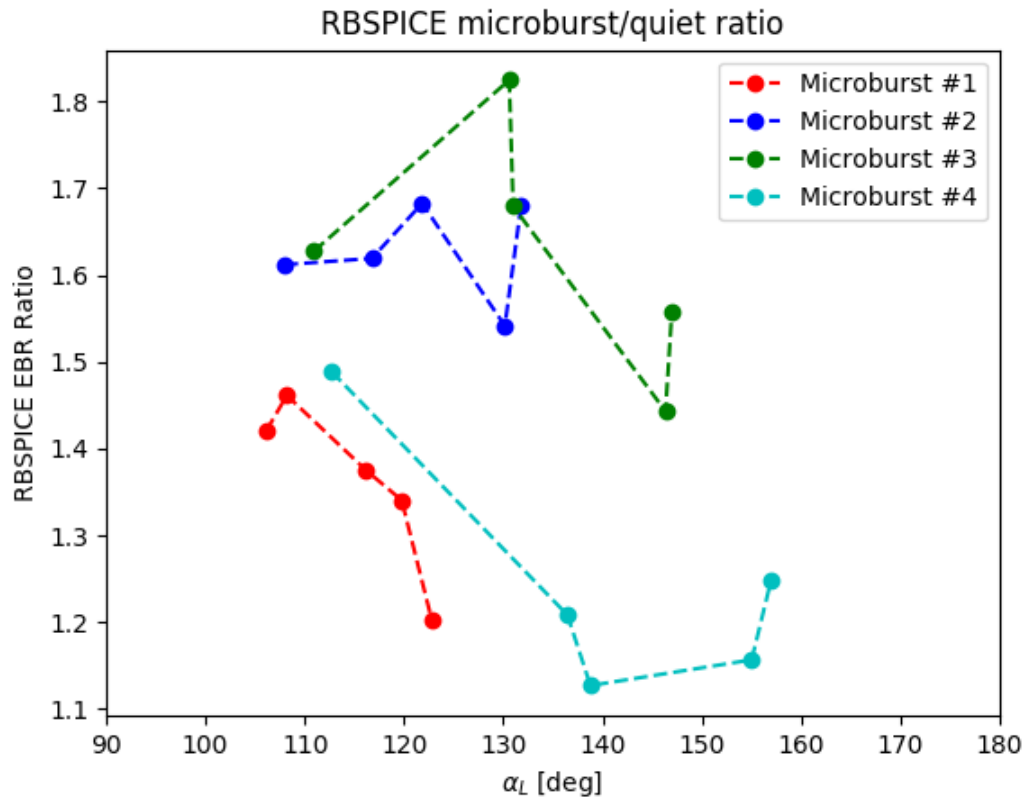


Figure A.2: Ratio of the RBSPICE EBR at microburst times indicated with the black vertical arrows in Fig. 2, to the EBR at the same pitch angles one spin prior (quiet time). The microburst flux was enhanced by 10-80% across $100^\circ < \alpha_L < 160^\circ$ PA, and appear to be peaked closer to $\alpha_L = 90^\circ$.

1651

APPENDIX: APPENDIX B

1652 This appendix describes the method we used to calculate the time difference and
 1653 separation between FU3 and FU4 at 06:12 UT on February 2nd, 2015. We used the
 1654 following method to calculate the clock difference, δt_c and separation, d between FU3
 1655 and FU4 at 06:12 UT on February 2nd, 2015.

1656 The relative clock difference was calculated with a cross-correlation time
 1657 lag analysis on uniquely-identified trains of microbursts that hit both spacecraft
 1658 simultaneously. Four time periods with coincident microbursts were hand-picked on
 1659 February 2nd, 2015 and are shown in Figs. B.1-B.4, panels (a) and (b). The cross-
 1660 correlation time lag analysis was applied to the HiRes time series in panels (a) and
 1661 (b), and the resulting normalized cross-correlation coefficient as a function of time is
 1662 shown in panel (c). To validate the peak lag identified in panel (c), FU3's time series
 1663 was shifted by that lag and is shown in panel (d).

1664 The clock differences from the simultaneous microbursts in Figs. B.1-B.4 were
 1665 linearly fit to account for the relative clock drift (≈ 20 ms/hour at this time), giving
 1666 a value of $\delta t_c = 2.28 \pm 0.12$ s at the time of the microburst analyzed here. This time
 1667 shift was applied to the HiRes data in Fig. 1. A clock difference of $\delta t_c = 2.45^{+0.51}_{-0.98}$ s
 1668 was independently calculated with the FIREBIRD-II telemetry beacon time stamps
 1669 that were downlinked during operational passes.

1670 We calculate the spacecraft separation, by applying same the cross-correlation
 1671 time lag analysis on structures assumed to be spatial and are shown in Figs. B.5
 1672 and B.6. The lag from the peak cross-correlation between these events is a sum of
 1673 the clock difference and time lag due to the spacecraft separation. We interpret the
 1674 time lag due to the spacecraft separation as the time difference between when the
 1675 leading satellite observed a stationary spatial feature, to when the trailing satellite
 1676 observed the same stationary spatial feature. With the method described above, we
 1677 find the spatial time lag to be $\delta t_d = 2.64 \pm 0.12$ s (after we account for the clock
 1678 difference and its uncertainty). To convert from a spatial time lag to a spacecraft
 1679 separation, we calculate the satellite velocity. We calculate the velocity using a Two
 1680 Line Element (TLE), a data format containing the orbit parameters that are used
 1681 for orbit propagation. With the TLE derived spacecraft velocity, $v = 7.57$ km/s, the
 1682 spacecraft separation was $d = 19.9 \pm 0.9$ km.

1683 An independent method to calculate the spacecraft separation was developed.
 1684 The separation was calculated using TLEs. The TLE from February 2nd was
 1685 anomalous and was not used in this analysis. Instead, seven TLEs released up to
 1686 five days after the microburst event were backpropagated, using the SGP-4 algorithm
 1687 (Hoots and Roehrich, 1980) that calculates orbital state vectors with perturbations
 1688 such as Earth's atmosphere, as well as gravitational effects from the moon and sun.
 1689 Then the predicted spacecraft separations at the time of the microburst event were

₁₆₉₀ averaged to derive a separation of $d = 18.4 \pm 1.5$ km. These two methods give
₁₆₉₁ similar separations, which implies that the stationary event assumption used in the
₁₆₉₂ cross-correlation time lag analysis is reasonable.

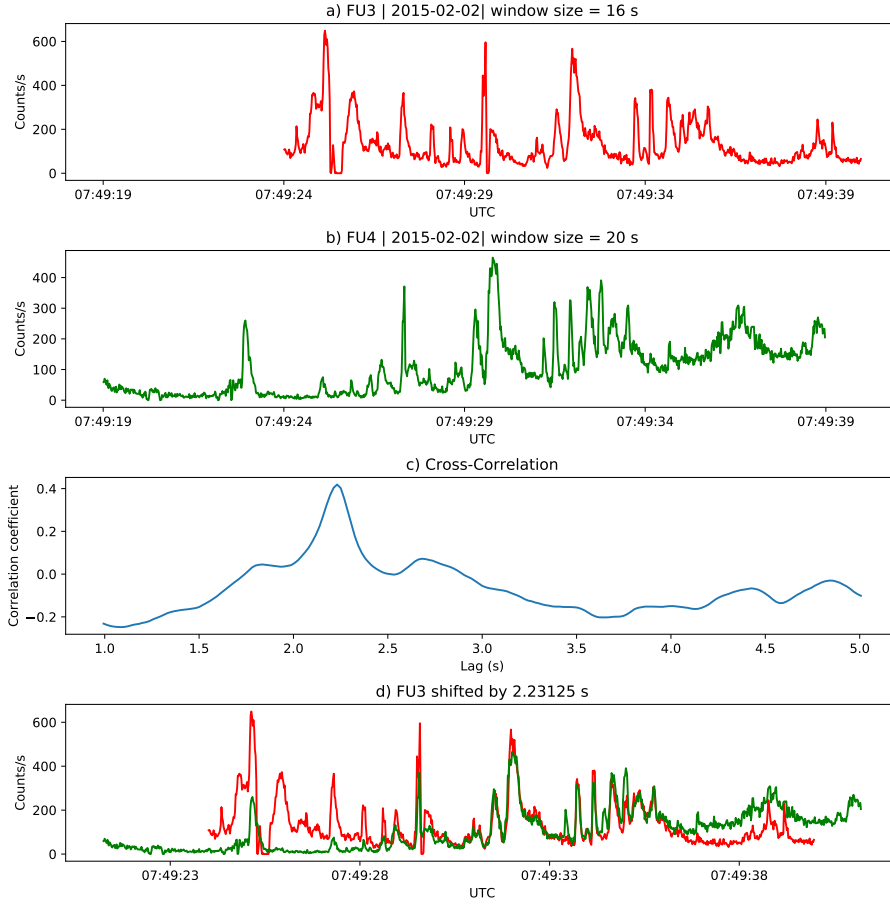


Figure B.1: Cross-correlation time lag analysis applied to a train of microbursts. Panel (a) and (b) show the count rate from the lowest energy channel. Panel (c) shows the cross-correlation coefficient as a function of time lag. Panel (d) shows the shifted timeseries. Clock difference was 2.23 s.

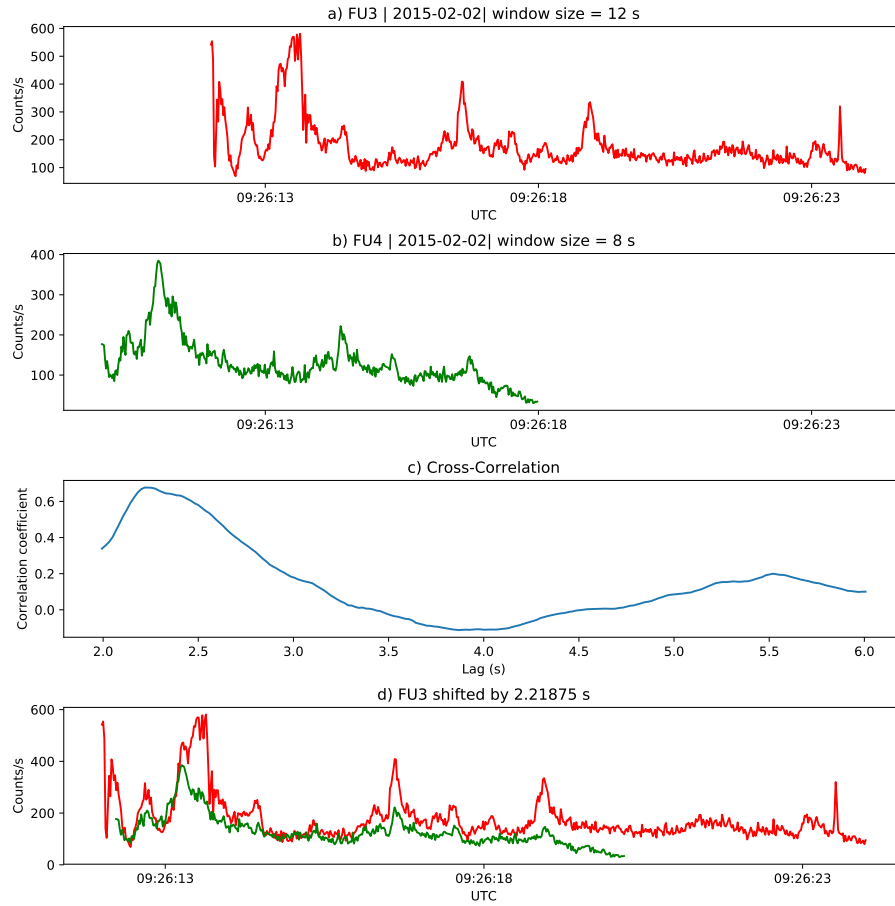


Figure B.2: Same analysis as Fig. B.1 on a different time period. Clock difference was 2.21 s.

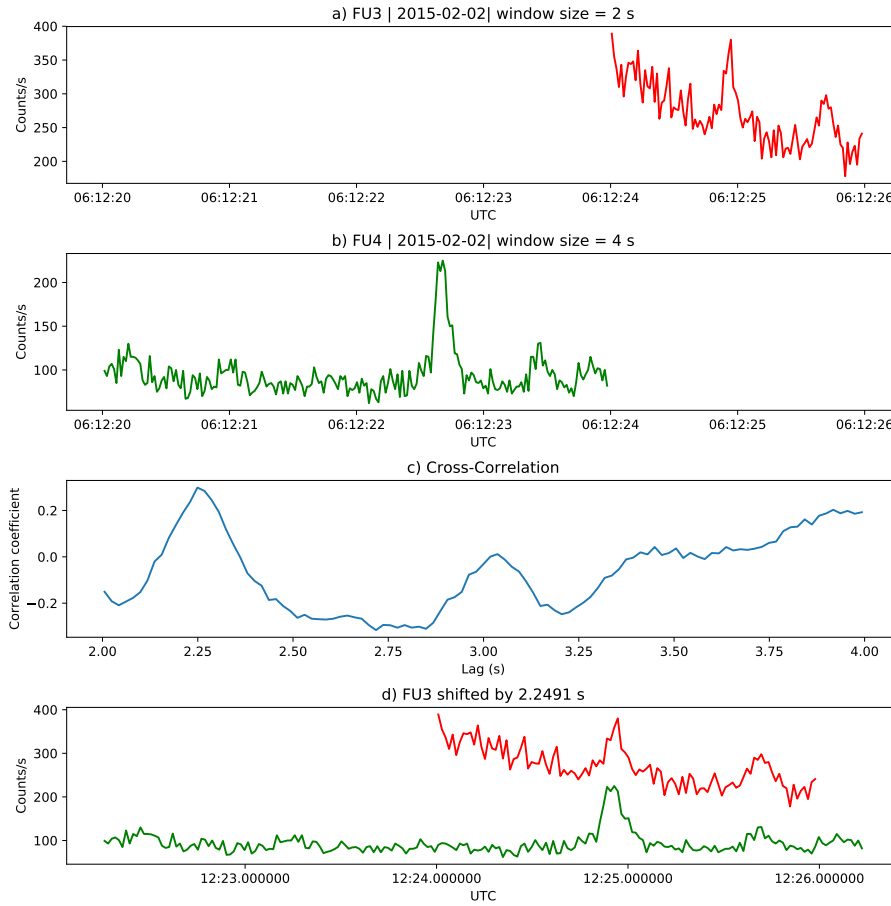


Figure B.3: Same analysis as Fig. B.1 on a different time period. Clock difference was 2.25 s.

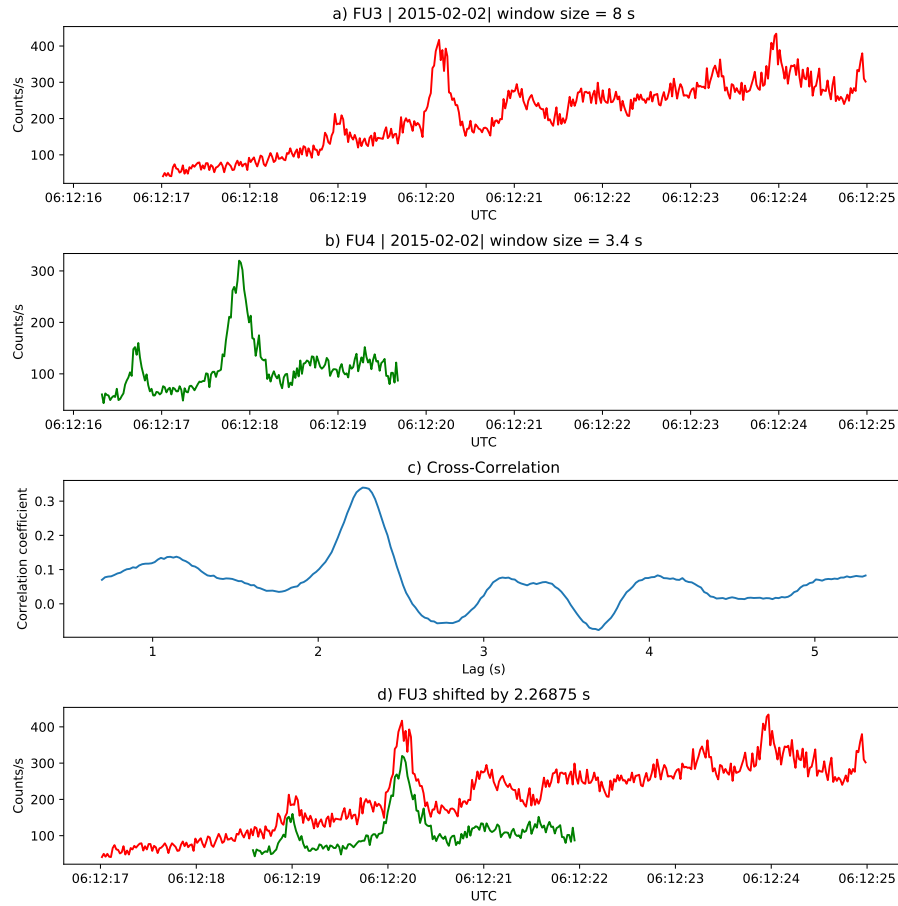


Figure B.4: Same analysis as Fig. B.1 on a different time period. Clock difference was 2.27 s.

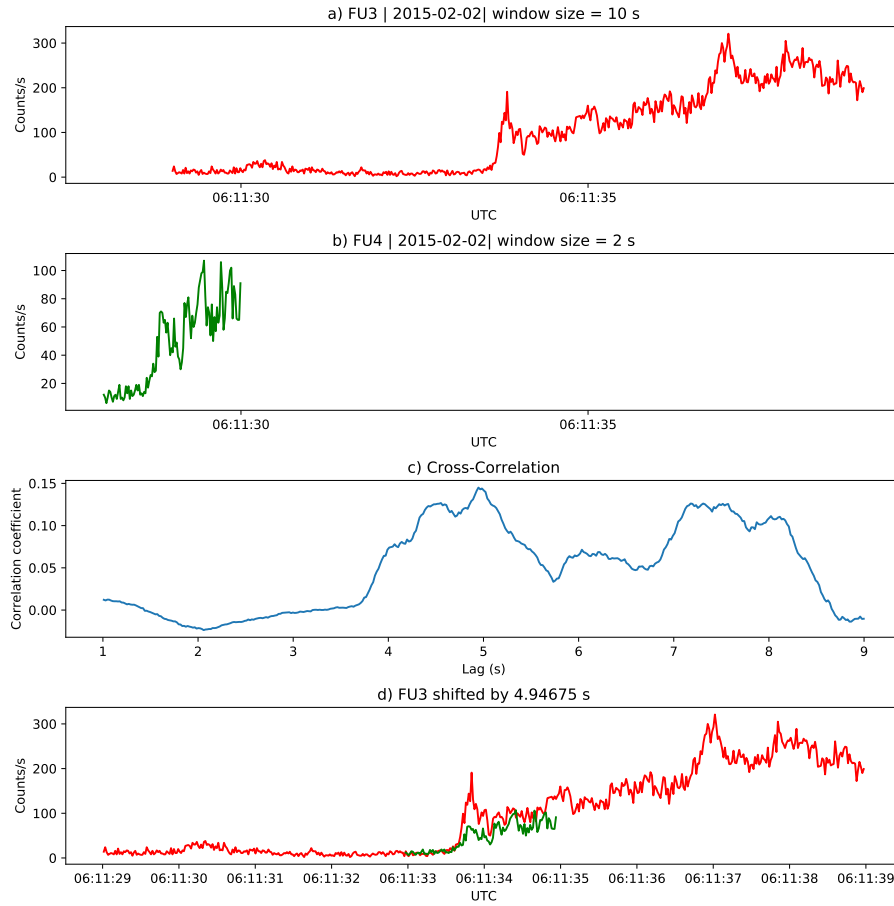


Figure B.5: Same cross-correlation time lag analysis applied to stationary spatial structures. The cross-correlation lag between these events is a sum of the clock difference and time lag due to the spacecraft separation. The lag derived at this time was 4.95 s.

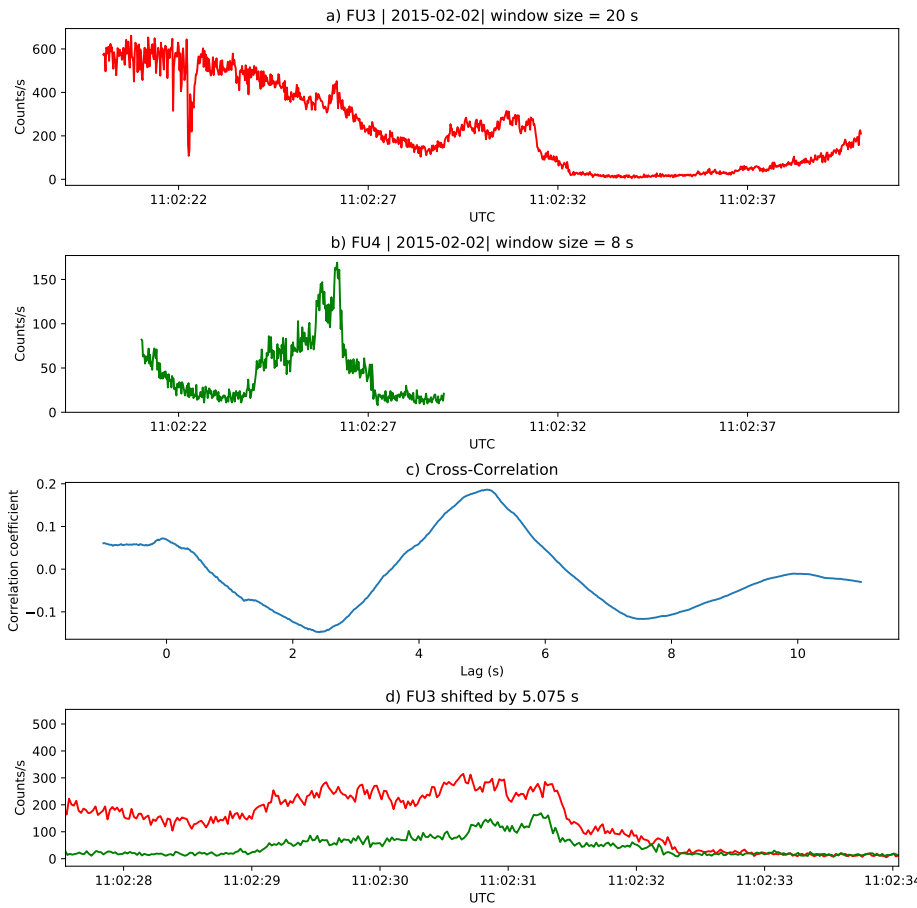


Figure B.6: Same analysis as Fig. B.5 applied to a different stationary spatial feature. The lag derived at this time was 5.01 s.